EUMETSAT Satellite Application Facility on Climate Monitoring

The EUMETSAT
Network of
Satellite
Application
Facilities

CM SAF
Climate Monitoring

Algorithm Theoretical Basis Document

Top of Atmosphere Radiation

MVIRI/SEVIRI Data Record

CM-Product identifier: CM-23311, CM-23341

Reference Number:	**SAF/CM/RMIB/ATBD/MET_TOA**
Version:	**1.3**
Date:	**5 October 2016**

Document Signature Table

	Name	Function	Signature	Date
Author	Manon Urbain Nicolas Clerbaux Alessandro Ipe Florian Tornow	CM SAF Scientists		05.10.2016
Approval	Rainer Hollmann SG	Science Manager Steering Group		
Release	Martin Werscheck	Project Manager		

Distribution List

Internal Distribution	
Name	**No. Copies**
DWD Archive	1

External Distribution		
Company	**Name**	**No. Copies**
PUBLIC		1

Document Change Record

Issue/ Revision	Date	DCN No.	Changed Pages/Paragraphs
1.0	07.08.2015	SAF/CM/RMIB/ATBD/MET_TOA	Initial issue
1.1	07.08.2015	SAF/CM/RMIB/ATBD/MET_TOA	Update following PCR 2.6
1.2	23.05.2016	SAF/CM/RMIB/ATBD/MET_TOA	Update in view of DRR 2.6
1.3	05.10.2016	SAF/CM/RMIB/ATBD/MET_TOA	Update following DRR 2.6

Applicable documents

Reference	Title	Code
AD 1	CM SAF CDOP2 Project Plan	SAF/CM/DWD/PP/1.6
AD 2	CM SAF Product Requirement Document	SAF/CM/DWD/PRD/2.8

Reference documents

Reference	Title	Code
RD 1	GERB Dataset Scientific Validation document, version 3.0	SAF/CM/RMIB/VAL/GERB_DS
RD 2	GERB Dataset Product User Manual, version 3.0	SAF/CM/RMIB/PUM/GERB_DS
RD 3	GERB Dataset Generation Capability Description Document, version 3.0	SAF/CM/RMIB/DGCDD/GERB_DS
RD 5	Requirements Review 2.6 document. TOA Radiation – TCDR MVIRI/SEVIRI Edition 1 data sets, version 3.0	SAF/CM/RMIB/GERB/RR2.6
RD 6	TOA Radiation MVIRI/SEVIRI Dataset Generation Capability Description Document, version 1.0	SAF/CM/RMIB/DGCDD/MET_TOA
RD 7	GERB Datasets 2nd Edition Algorithm Theoretical Basis Document, version 1.0	SAF/CM/RMIB/ATBD/GERB_DS_R2
RD 8	TOA Radiation MVIRI/SEVIRI Product User Manual, version 1.1	SAF/CM/RMIB/PUM/MET_TOA
RD 9	TOA Radiation MVIRI/SEVIRI Validation Report, version 1.1	SAF/CM/RMIB/VAL/MET_TOA

	EUMETSAT SAF on CLIMATE MONITORING	Doc. SAF/CM/RMIB/ATBD/MET_TOA
	Algorithm Theoretical Basis Document	Issue: 1.3
	TOA Radiation MVIRI/SEVIRI Data Record	Date: 5 October 2016

Table of Contents

List of Tables

List of Figures

1   The EUMETSAT SAF on Climate Monitoring (CM SAF)

The importance of climate monitoring with satellites was recognized in 2000 by EUMETSAT Member States when they amended the EUMETSAT Convention to affirm that the EUMETSAT mandate is also to "contribute to the operational monitoring of the climate and the detection of global climatic changes". Following this, EUMETSAT established within its Satellite Application Facility (SAF) network a dedicated centre, the SAF on Climate Monitoring (CM SAF, http://www.cmsaf.eu).

The consortium of CM SAF currently comprises the Deutscher Wetterdienst (DWD) as host institute, and the partners from the Royal Meteorological Institute of Belgium (RMIB), the Finnish Meteorological Institute (FMI), the Royal Meteorological Institute of the Netherlands (KNMI), the Swedish Meteorological and Hydrological Institute (SMHI), the Meteorological Service of Switzerland (MeteoSwiss), and the Meteorological Service of the United Kingdom (UK MetOffice). Since the beginning in 1999, the EUMETSAT Satellite Application Facility on Climate Monitoring (CM SAF) has developed and will continue to develop capabilities for a sustained generation and provision of Climate Data Records (CDR's) derived from operational meteorological satellites.

In particular, the generation of long-term data records is pursued. The ultimate aim is to make the resulting data records suitable for the analysis of climate variability and potentially the detection of climate trends. CM SAF works in close collaboration with the EUMETSAT Central Facility and liaises with other satellite operators to advance the availability, quality and usability of Fundamental Climate Data Records (FCDRs) as defined by the Global Climate Observing System (GCOS). As a major task the CM SAF utilizes FCDRs to produce records of Essential Climate Variables (ECVs) as defined by GCOS. Thematically, the focus of CM SAF is on ECVs associated with the global energy and water cycle.

Another essential task of CM SAF is to produce data records that can serve applications related to the Global Framework of Climate Services initiated by the WMO World Climate Conference-3 in 2009. CM SAF is supporting climate services at national meteorological and hydrological services (NMHSs) with long-term data records but also with data records produced close to real time that can be used to prepare monthly/annual updates of the state of the climate. Both types of products together allow for a consistent description of mean values, anomalies, variability and potential trends for the chosen ECVs. CM SAF ECV data records also serve the improvement of climate models both at global and regional scale.

As an essential partner in the related international frameworks, in particular WMO SCOPE-CM (Sustained COordinated Processing of Environmental satellite data for Climate Monitoring), the CM SAF - together with the EUMETSAT Central Facility, assumes the role as main implementer of EUMETSAT's commitments in support to global climate monitoring. This is achieved through:

- Application of highest standards and guidelines as lined out by GCOS for the satellite data processing,

- Processing of satellite data within a true international collaboration benefiting from developments at international level and pollinating the partnership with own ideas and standards,

- Intensive validation and improvement of the CM SAF climate data records,

- Taking a major role in data record assessments performed by research organisations such as WCRP (World Climate Research Program). This role provides the CM SAF with deep contacts to research organizations that form a substantial user group for the CM SAF CDRs,

- Maintaining and providing an operational and sustained infrastructure that can serve the community within the transition of mature CDR products from the research community into operational environments.

A catalogue of all available CM SAF products is accessible via the CM SAF webpage, http:/www.cmsaf.eu/. Here, detailed information about product ordering, add-on tools, sample programs and documentation is provided.

2   Introduction

2.1   Scope of the document

The purpose of this document is to describe the algorithm implemented within the CM SAF to generate daily mean, monthly mean and monthly mean diurnal cycle of Top-Of-Atmosphere (TOA) radiative fluxes data records from the MVIRI and SEVIRI instruments on board the Meteosat satellites. The observations from the GERB radiometer are used to derive empirical narrowband to broadband relations for MVIRI and SEVIRI. Once those relations have been derived, GERB is not needed as input data for the processing. This document focuses on the algorithm while details about the processing system are provided in the Dataset Generation Capability Description Document (DGCDD) [RD6].

Two data records are generated with the following CM SAF identifiers:

CM SAF identifier	Content
CM-23311	TOA Reflected Solar radiative flux – All Sky (TRS_AS)
CM-23341	TOA Emitted Thermal radiative flux – All Sky (TET_AS)

2.2   Content of the document

This Algorithm Theoretical Basis Document (ATBD) is structured as follows.

- Section 3 provides a summary of the problems involved and the adopted strategies. This section also summarizes the users' requirements from [RD5].

- Section 4 provides basic information about the data used as input of the processing.

Then, the core of the document consists of 4 sections providing the complete description/justification of the 4 main algorithms used to generate the datasets, namely:

- Section 5 : the visible clear-sky processing.

- Section 6 : the preprocessing of the input data.

- Section 7 : the estimation of the instantaneous TOA radiative fluxes.

- Section 8 : the daily and monthly mean averaging and the spatial re-gridding.

Then, Section 9 presents some comparisons with CERES EBAF and discusses the results in view of the user's requirements [RD5]. Finally, Section 10 describes the data record content.

3   Problem statement and adopted approach

3.1   Data records purposes

At the Top-Of-Atmosphere (TOA) the following radiative fluxes are defined: the TOA Incoming Solar (TIS), the TOA Reflected Solar (TRS) and the TOA Emitted Thermal (TET).
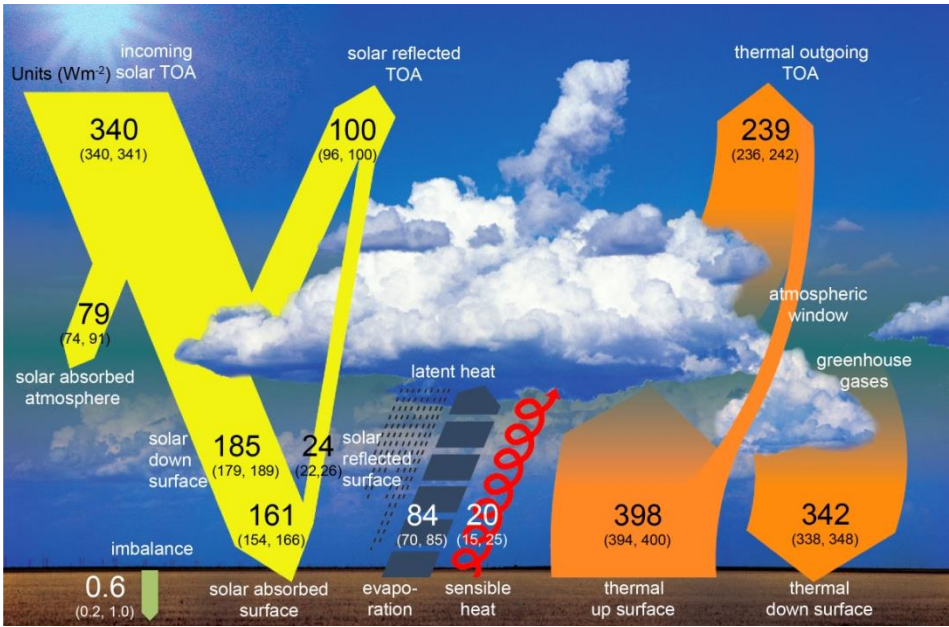
Figure 1: Schematic diagram of the Earth Radiation Budget (from Wild et al., 2013). Numbers indicate best estimates or the magnitudes of the globally averaged energy balance components together with their uncertainty ranges, representing present day climate conditions at the beginning of the twenty first century. Units are $W.m^{-2}$.

These three components of the Earth Radiation Budget (ERB) are the driver of the climate on our planet. In the frame of climate monitoring, the continuous monitoring of these fluxes is of prime importance to understand climate variability and change. The nature of these quantities, which are defined at TOA, makes the use of satellite observations especially useful.

Over the Meteosat Field Of View (FOV), broadband observations of the TRS and TET are available since 2004 from the Geostationary Earth Radiation Budget (GERB, Harries et al, 2005) instruments on the Meteosat Second Generation (MSG) satellites. The instruments' observations are processed by the GERB team, a consortium including institutions in Germany, the UK and Belgium. Currently, GERB Edition-1 instantaneous fluxes are generated (Dewitte et al., 2008) and made available to the user community. Within CM SAF, the GERB Edition-1 instantaneous fluxes have been daily and monthly averaged, as well as monthly averaged of the hourly integrated values. Those data records have been released in 2013, with product identifier CM-113 (TRS) and CM-115 (TET).

Meteosat observations from around 0° longitude are however available since 1982 and have been used to derive a data record of surface radiation in CM SAF. Given the overlap between the Meteosat Visible and InfraRed Imager (MVIRI) and GERB in the period 2004-

2006, empirical narrowband to broadband regressions can be derived to "unfilter" the MVIRI channel observations, making the estimation of instantaneous fluxes from 1982 to 2006 possible. From 2004 onward, this estimation can be built on the MVIRI-like visible (VIS), water vapour (WV) and infrared (IR) channels simulated from the narrowband channels of the Spinning Enhanced Visible and InfraRed Imager (SEVIRI, Schmetz et al., 2002). This opens the door to the generation of a homogeneous data record covering more than 30 years. Consequently, it is proposed to use the Meteosat first and second generations' observations to construct long geostationary-based data records of TRS and TET radiative fluxes.

3.2 Summary of user requirements

[RD5] discusses the user requirements for such geostationary-based data records. Table 1 summarizes the requirements in terms of stability and Table 2 in terms of accuracy. Table 2 also summarizes the accuracy of the CM-113 and CM-115 products (from [RD2]) as well as documented accuracies of the Clouds and the Earth's Radiant Energy System (CERES, Wielicki et al., 1996) products.

The stability refers to the maximum acceptable change (max-min) of the systematic error over a period of 10 years. Changes of systematic error are primarily caused by switches from one instrument to another and instrumental drift. Stability requirements only apply to the monthly mean products (it is expected that the daily mean and monthly mean diurnal cycle products will be characterized by the same stability). The validation activities should also provide evidence that stability requirements are met over most of the scene types. Otherwise, it will be documented in the Product User Manual (PUM).

Table 1: Stability requirements for CM-23311 and CM-23341 from [RD5].

Products	Threshold	Target	Optimal	Remarks
TRS all sky MM	4 W/m^2/dec	0.6 W/m^2/dec	0.3 W/m^2/dec	
TET all sky MM	4 W/m^2/dec	0.6 W/m^2/dec	0.3 W/m^2/dec	

Table 2: Accuracy requirements for CM-23311 (TRS) and CM-23341 (TET) and for the Monthly Mean (MM), the Daily mean (DM) and the Monthly mean diurnal Cycle (MMDC) from [RD5].

Products		Threshold	Target	Optimal	CM-113 and CM-115 accuracy	CERES accuracy	Remarks
TRS CM-23311	MM	8 W/m^2	4 W/m^2	2 W/m^2	3.0 W/m^2	4.2 W/m^2	Requirements referring to error: - at 1 standard deviation (RMS error) - at 1° x 1° scale - taking only VZA<60° - does not include error (bias) due to the absolute calibration.
	DM	16W/m^2	8 W/m^2	4 W/m^2	5.5 W/m^2	7.8 W/m^2	
	MMDC	16W/m^2	8 W/m^2	4 W/m^2	12.8W/m^2	16.7 W/m^2 (3-hour)	
TET CM-23341	MM	4 W/m^2	2 W/m^2	1 W/m^2	2.0 W/m^2	2.0 W/m^2	
	DM	8 W/m^2	4 W/m^2	2 W/m^2	3.6 W/m^2	1.9 W/m^2	
	MMDC	8 W/m^2	4 W/m^2	2 W/m^2	3.1 W/m^2	3.1 W/m^2 (3-hour)	

3.3 Processing overview

Figure 2 provides a sketch of the processing into its 4 main processing steps and outlines its main inputs and outputs.

Figure 2: Processing flowchart

The "**Visible clear-sky processing**" subsystem aims at generating the clear-sky visible data that are needed to process the TOA fluxes. In those images, the cloud effect has been filtered by image processing techniques, based on a series of input visible images covering a period of 61 days around the day of interest. A recursive loop is used to generate the clear sky (CS) images over a long period of time to save CPU resources. The CS VIS estimates are an important input for cloud detection and characterization. This first subsystem is described in section 5.

The "**Data preprocessing**" subsystem performs several corrections of the input visible, water vapour and infrared data such as calibration, ageing correction, stripes' interpolation and conversion to equivalent Meteosat-7 ("MET7-like") observations. The outputs of the preprocessing are given in reflectances for the VIS channel, in radiances for the WV channel, and in radiances and brightness temperatures for the IR channel. This preprocessing step is needed as the Meteosat observations are not yet available as Fundamental Climate Data Record (FCDR). In the future, it can be expected that a FCDR will be provided by EUMETSAT. This second subsystem is described in section 6.

In the "**TOA fluxes processing**", the TRS and TET instantaneous radiative fluxes are generated at the time of the imager acquisition from the MET7-like observations through various stages: a scene identification (performed only during daytime, i.e. for Solar Zenith Angle (SZA) < 80°), narrowband-to-broadband relations to "unfilter" the MET7-like radiances, and angular dependency models to convert broadband radiances into fluxes. The TOA fluxes are generated on a geostationary grid at the full resolution, i.e.: $(2.5 \text{ km})^2$, $(5 \text{ km})^2$ and $(3 \text{ km})^2$ at sub-satellite point respectively for the visible MVIRI, the thermal MVIRI and the SEVIRI channels. The algorithm used for the TOA fluxes processing is described in section 7.

Finally, the "**Daily and monthly averaging**" subsystem performs the averaging of the TRS and TET fluxes in hourly boxes, from which the daily mean, monthly mean and monthly mean diurnal cycle are estimated. A maximum of 3 hours of successive missing data is accepted in the daily averaging; otherwise the daily mean is not issued. A minimum number of 15 days is required to process the monthly mean and monthly mean diurnal cycle. The seasonal change in insolation during the month is also taken into account in the monthly averaging. The data are finally re-gridded from the geostationary grid onto a common regular grid with a spatial resolution of $(0.05°)^2$. This regridding is performed for consistency with other CM SAF products (e.g. CLAAS and SARAH) and also to ease the use of the product. The averaging and regridding algorithms used for this last part of the processing are described in section 8.

3.4 Product features

The main features of the CM-23311 and CM-23341 data records are summarized in Table 3.

Table 3: Main features of the CM-23311 and CM-23341 data records.

Covered period	**32 years**, from 1 February 1983 to 31 January 2015.
VIS channel ageing correction	**Correction** of the MVIRI and SEVIRI ageing using, respectively, the SEVIRI Solar Channel Calibration (SSCC, Govaerts et al., 2004) and Meirink et al. (2013).
Spectral response correction (NB→NB)	MET7-like VIS channels are simulated using **regressions** from narrowband channels which are **theoretical for MVIRI and empirical for SEVIRI** while MET7-like WV and IR channels are simulated using **theoretical regressions.**
Unfiltering (NB→BB)	**Empirical narrowband-to-broadband regressions** are used to "unfilter" the MET7-like channel observations. GERB is used "off-line" to tune the regressions.
Fluxes computation (ADM)	Using **CERES TRMM angular dependency models** (ADMs) for the TRS (Loeb et al., 2003) and **theoretical models** for the TET (Clerbaux et al., 2003a).
Output quantities	TRS and TET fluxes in **"all sky"** conditions (no clear-sky fluxes data records in this first version of the data records).
Temporal characteristics	Fluxes provided as **daily mean**, **monthly mean** and monthly mean of the hourly values (**diurnal cycle**).
Spatial resolution	Data records provided on a regular lat-lon grid with a spatial resolution of $(0.05°)^2$, i.e., about $(5.5 km)^2$ at sub-satellite point. Internally, TRS and TET are computed as instantaneous fluxes on the geostationary grid at a spatial resolution of $(2.5 km)^2$ and $(5 km)^2$ for MFG and of $(3 km)^2$ for MSG respectively.
Validation	Validation performed at lower resolution (e.g. 1°x1°) by **intercomparison** with several other data records (CERES EBAF, HIRS OLR CDR, etc.).
Format	A **NetCDF** file format following the CF convention. Preliminary information about the data record format, metadata and attributes, is provided in Section 10.

4   Input data description

4.1   MVIRI Level 1.5 data

4.1.1 Introduction

The Meteosat Visible and InfraRed Imager (MVIRI) instruments are high resolution radiometers on-board the Meteosat First Generation (MFG) satellites (1977-2006 at 0°). They provide a continuous imaging of the Earth over the Meteosat FOV which is observed from South to North and from East to West. A full Earth scan is performed each 30 minutes. The MVIRI instruments measure radiation using a reflecting telescope within three spectral bands chosen in accordance with Meteosat's primary task of mapping the distribution of clouds and water vapour. These bands and their characteristics are summarized in Table 4. They provide a spatial resolution at sub-satellite point of 2.5 km x 2.5 km and 5 km x 5 km respectively for the shortwave (SW) and the longwave (LW) channels.

Table 4: Spectral channel characteristics of MVIRI in terms of central, minimum and maximum wavelength of the channels, resolution at sub-satellite point, and the main application areas of each channel.

Spectral band	Characteristics of spectral band (μm)			Resolution at sub-satellite point (km)	Main observational application
	λcen	λmin	λmax		
VIS	0.70	0.45	1.0	2.5	Cloud imaging during daytime
WV	6.40	5.7	7.1	5	Determination of the amount of water vapour in the upper troposphere
IR	11.5	10.5	12.5	5	Detection of clouds, estimation of the temperature of cloud tops and the ocean's surface by day and night

The MFG series of satellites consists of seven spin-stabilised geostationary satellites, called Meteosat-1 to -7. The first of this series, Meteosat-1, was the first European meteorological satellite sent into space. Launch dates and status of all the MFG satellites are summarised in Table 5. Meteosat-1 failed after two years due to a design fault and its images were never transcribed into the EUMETSAT archive (EUMETSAT, 2011). Together with Meteosat-2 and -3, it was part of the pre-operational phase of the Meteosat program. This phase was followed by the Meteosat Operational Program (MOP) during which the three satellites Meteosat-4, -5 and -6 were launched. Meteosat-7 was launched as the Meteosat Transition Program (MTP), needed to ensure the operational continuity between the MOP and the Meteosat Second Generation (MSG) satellites. As shown in Table 5, all the MVIRI instruments have been working at the nominal position of 0° longitude and some of them have been moved to other locations on the geostationary ring afterwards in support of other programs. The Meteosat system is designed as a dual-satellite service, always keeping an additional satellite in orbit as back up.

The MVIRI Level 1.5 data were retrieved from the EUMETSAT Data Center as images of 5000 x 5000 pixels for the visible channel and 2500 x 2500 pixels for the thermal channels. The values are coded on 8 bits. However, for the VIS images of Meteosat-2 and -3 the digitalization of the detector's signal has been done on only 6 bits. The level 1.5 data is built from the original level 1.0 data by correcting them for undesirable geometrics effects and by rectifying them on a reference geostationary projection.

Table 5: Lifetime and services of the Meteosat First Generation satellites. The prime date indicates when the instrument was declared operational.

Satellite	Launch date	Prime date	Retirement date	Status
Meteosat-1	23/11/1977	09/12/1977	25/11/1979	0 degree coverage
Meteosat-2	19/06/1981	16/08/1981	11/08/1988	0 degree coverage
Meteosat-3	15/06/1988	11/08/1988	31/05/1995	0 degree coverage, ADC[1] (01/08/1991–27/01/1993), XADC[2] (21/02/1993–31/05/1995)
Meteosat-4	06/03/1989	19/06/1989	04/02/1994	0 degree coverage
Meteosat-5	02/03/1991	02/05/1991	16/04/2007	0 degree coverage, IODC[3] (01/07/1998–16/04/2007)
Meteosat-6	19/11/1993	21/10/1996	15/04/2011	0 degree coverage, IODC (08/01/2007–15/04/2011)
Meteosat-7	02/09/1997	03/06/1998	2016	0 degree coverage, IODC (since 11/2006)

4.1.2 Spectral response of the instruments

The normalised spectral response (SR) of a channel corresponds to the ratio between the instrument response and the incoming energy, normalised to 1.0 at the wavelength where the instrument presents the highest sensitivity. For MFG, there are two detectors operating in the VIS channel (VIS1 and VIS2) while there is only one in the IR and WV channels. The VIS

---

[1] Atlantic Data Coverage

[2] Extended Atlantic Data Coverage

[3] Indian Ocean Data Coverage

SR curve is obtained by taking the average of both detectors' SR. The normalised SR curves of the MVIRI instruments' channels are shown as a function of wavelength in Figure 3 for the VIS, in Figure 4 for the WV and in Figure 5 for the IR.

It is worth pointing out that the Meteosat-5, -6 and -7 satellites show the same spectral response curves in the VIS channel. Indeed, the silicon photo-diode detectors of Meteosat-5 to -7 have been produced in the same batch and have therefore similar spectral behavior (Govaerts, 1999). Consequently, their VIS spectral responses are nearly identical. However, the SR of the Meteosat-5 and -6 instruments were originally poorly characterised, in particular for the visible channel, unlike the SR of the Meteosat-7 radiometer VIS channel. According to Govaerts (1999), the pre-launch SR of both former instruments have a large uncertainty. The Meteosat-5 and -6 SR curves were thus replaced by the SR of the Meteosat-7 radiometer VIS channel.

Figure 3: Normalised spectral response curves of the MFG VIS channels

Figure 4: Normalised spectral response curves of the MFG WV channels

Figure 5: Normalised spectral response curves of the MFG IR channels

The normalised SR curves are used in the data preprocessing to tune the theoretical regressions used to convert the input data to their Meteosat-7 counterparts ("MET7-like"). The simulation of MET7-like VIS, WV and IR channels is discussed in Section 6.

4.1.3 **VIS channel calibration**

As mentioned before, the MVIRI instruments have two detectors operating in the VIS channel which are scanning simultaneously two lines of pixels. Two backup detectors can be used in case of failure of the two operational ones. Such radiometers measure the radiation hitting the detectors in digital units, called counts, which are proportional to the radiances. The narrowband (NB) radiances (L), expressed in $W.m^{-2}.sr^{-1}$, can be obtained from the integer image value (called "count" C) using a constant offset value (O_v, expressed in counts) and a calibration coefficient (g, expressed in $W.m^{-2}.sr^{-1}.count^{-1}$) according to

$$L = g \ (C - O_v)$$

Because of the degradation with time of the instrument's optics and detectors in the visible channels, an ageing correction of the measured radiances is required. This ageing process results in a decrease of the channel's SR curve with time. It was originally thought to be uniform over the spectrum. To correct for this effect, a calibration coefficient linearly increasing in time, called drift, can be estimated. The SEVIRI Solar Channels Calibration (SSCC) (Govaerts et al., 2004), developed by EUMETSAT in preparation of the MSG satellites, provides a vicarious calibration method for the VIS channels based on radiative transfer modelling over bright desert and clear ocean targets, i.e., targets with relatively well known and stable spectral reflectance (Govaerts et al., 2001). Originally developed for SEVIRI, the method has been applied to the VIS channel of the MFG (Govaerts et al., 2004).

The SSCC results are currently the "official" calibration and are available on the EUMETSAT webpage. The calibration coefficients at launch (expressed in $W.m^{-2}.sr^{-1}.count^{-1}$), the time average offset values (in count), the daily drift from the SSCC method (in $W.m^{-2}.sr^{-1}.count^{-1}.day^{-1}$) as well as the filtered solar irradiance (FSI, in $W.m^{-2}$) are shown in Table 6 for each MVIRI instrument on board the MFG satellites. For a same satellite, different calibration coefficients must be estimated in case of modification of the electronic gain of the VIS channel (e.g. Meteosat-2a and -b).

Validation of the SSCC calibration method, also performed in Govaerts et al. (2004), demonstrated that the ageing process has a spectral feature contrary to what was initially assumed. The degradation is stronger for the shorter wavelengths of the VIS channels than for the longer ones. Govaerts et al. (2004) also showed a saturation of the drift in time meaning that the signal, initially decreasing linearly, starts to decrease less after a certain amount of time. Therefore, an exponential model seems to be better suited than a linear model to capture the ageing process. Decoster et al. (2013a, 2013b, 2014a) and Decoster (2014b) have developed a semi-empirical spectral ageing model that simulates the degradation of the spectral response of the VIS channels of the MVIRI radiometers. This calibration method could potentially be implemented in a later version in the "MVIRI/SEVIRI Data record" although the effect of the MVIRI VIS channel spectral ageing on the Earth Radiation Budget is limited, see section 4.4.6 of the thesis of Decoster (2014b).

Table 6: Calibration of the VIS channel of the Meteosat First Generation satellites obtained using the SSCC.

Satellite	From		To		Gain level	Calibration coefficient at launch ($W.m^{-2}.sr^{-1}.count^{-1}$)	Offset (count)	Drift per day ($10^{-5}.W.m^{-2}.sr^{-1}.count^{-1}.day^{-1}$)	FSI ($W.m^{-2}$)
	Date	Slot	Date	Slot					
Meteosat-2a	19811019	34	19870512	16	0	0.652	3.729	2.322	499.9
Meteosat-2b	19810816	1	19811019	33	1	0.545	3.686	1.493	499.9
	19870512	17	19880811	14					
Meteosat-3a	19880801	17	19900125	17	1	0.628	3.712	3.547	602.2
	19910801	1	19910930	48					
Meteosat-3b	19900125	18	19910731	48	0	0.757	4.001	3.928	602.2
Meteosat-4	19890619	18	19941231	4	4	0.732	4.661	5.239	599.5
Meteosat-5	19911126	26	20050930	48	5	0.814	4.460	2.992	690.6
Meteosat-6	19961021	18	20050930	48	5	0.838	5.542	3.944	691.4
Meteosat-7	19980603	19	20051031	6	6	0.918	4.837	5.351	690.8

4.1.4 WV and IR channels calibration

As for the visible channel, the WV and IR radiances are obtained from the integer count values using a simple linear transformation. A preliminary processing of the whole data record highlighted significant stability issues within the operational calibration of the WV and IR channels provided by EUMETSAT. In addition, a significant gap was observed between MET-2 and -3 and the other MFG satellites, which made it necessary to introduce a correction factor to rectify their calibration coefficients. This is shown in Figure 6 for the MET7-like WV radiances and in Figure 7 for the MET7-like IR radiances.

To address these issues, it was decided to use the newly released beta version of the Global Space-based Inter-Calibration System (GSICS) recalibration of MVIRI that is derived from comparisons of collocated observations with the High-resolution Infrared Radiation Sounder (HIRS) instrument (R. Stöckli and A. Tetzlaff, pers. comm.). Calibration with respect to an independent stable reference is a prerequisite for derivation of long-term products from different satellites as well as for increasing confidence in the calibration of the individual satellites (Theodore and Heinemann, 2008). Using the EUMETSAT/GSICS recalibration provides much more stable results than the operational calibration. However, the MFG absolute level is decreased by about a factor of 0.3%. To ensure a good match between both generations of Meteosat satellites during the overlap period (2004-2006), a correction factor has been applied on the MFG WV and IR radiances to correct for this decrease. Since the

recalibration coefficients are not yet available for MET-2 and -3, the operational calibration has been used meanwhile. Information about the operational calibration is provided on the EUMETSAT webpage. Since 29th May 2000, it relies on the internal blackbody that has been added to Meteosat-7 while before that, it relies on a vicarious method using meteorological data and radiative transfer model. The coefficients provided by EUMETSAT are valid from the indicated time slot onwards, until the next calibration is provided.

The GSICS recalibration of MET-2 and -3 is expected to be available by the end of 2016 and may be used in a later version of this data record.
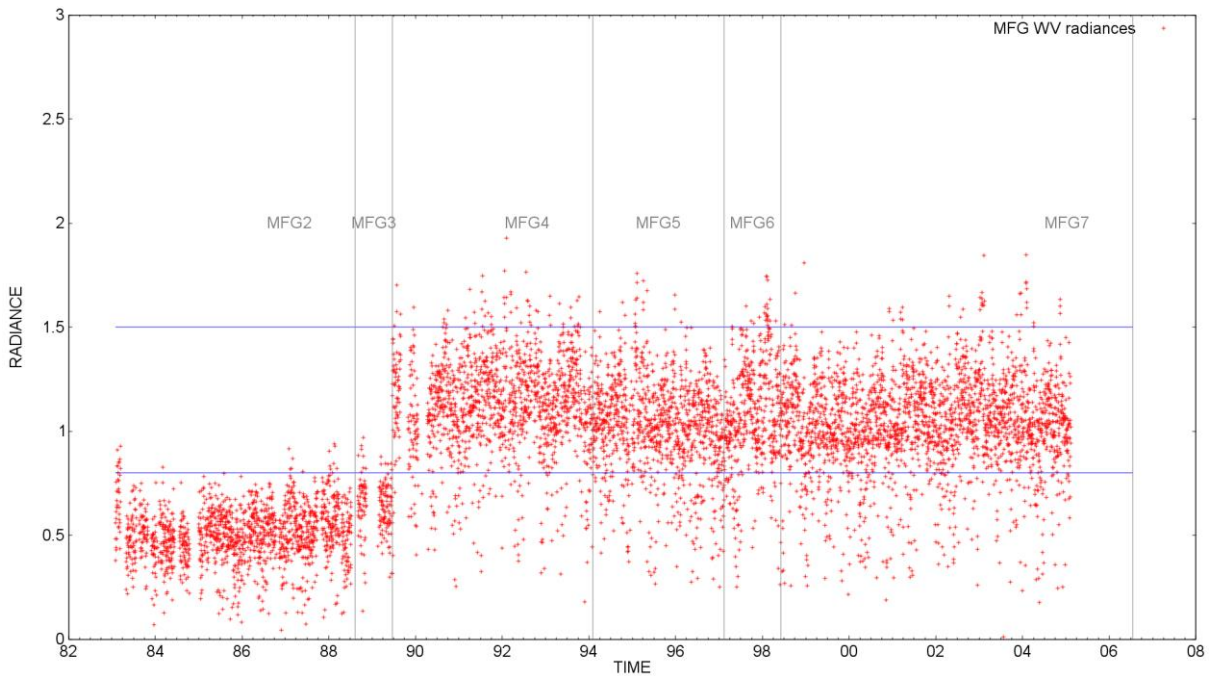
Figure 6: Time series of MET7-like WV radiances of all the MFG instruments from 1983 to 2006 for the pixel x=1292 and y=757. Blue lines give the position of 0.8 and 1.5 W.m^{-2}.sr^{-1} radiances. MET-2 and MET-3 data are clearly out of this range.
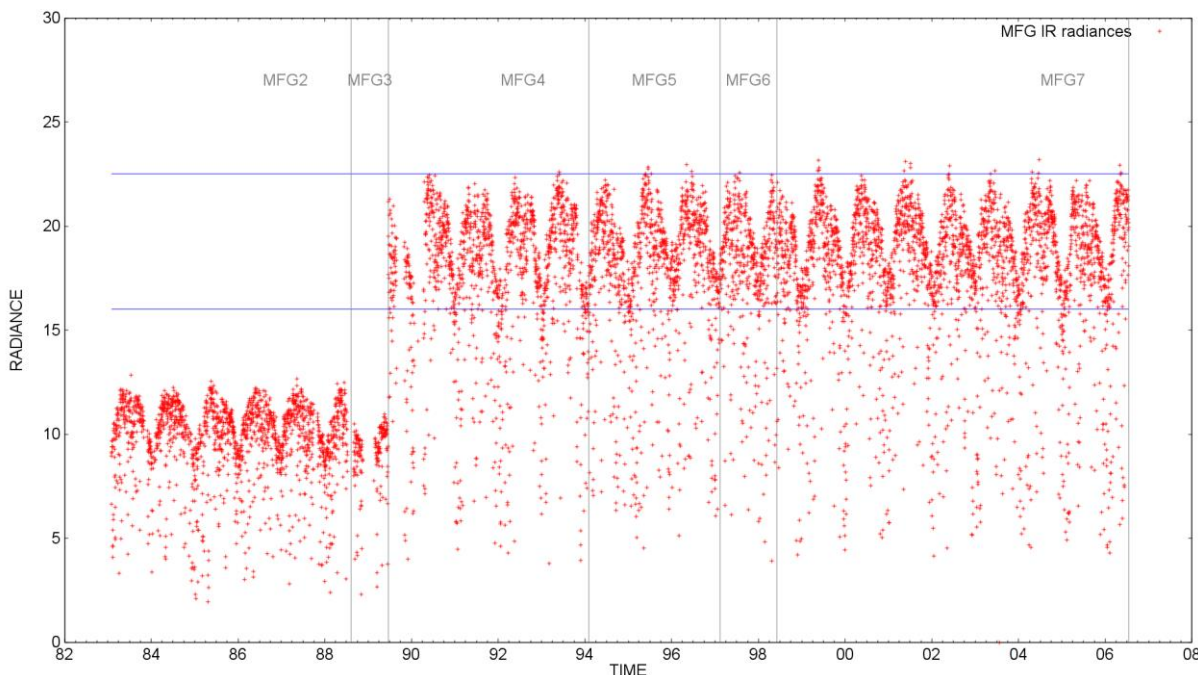
Figure 7: Time series of MET7-like IR radiances of all the MFG instruments from 1983 to 2006 for the pixel x=1292 and y=757. Blue lines give the position of 16.0 and 22.5 W.m^{-2}.sr^{-1} radiances. MET-2 and MET-3 data are clearly out of this range.

4.2   SEVIRI Level 1.5 data

4.2.1 Introduction

Meteosat Second Generation (MSG, Schmetz et al., 2002) is the second generation of spin-stabilised geostationary meteorological satellites developed by the European Space Agency (ESA) in close co-operation with EUMETSAT. The first satellite of this new generation, Meteosat-8, was launched in August 2002. So far the 4 MSG satellites (Meteosat-8, -9, -10 and -11) have been sent into space. The launch dates and status of all the MSG satellites are summarised in Table 7. The MSG prime satellites have always been located at a nominal longitude of 0°, except Meteosat-8 which has been operating at 3.5° West.

Table 7: Lifetime and services of the Meteosat Second Generation satellites.

Satellite	Launch date	Prime date	Retirement date	Current status
Meteosat-8	28/08/2002	19/01/2004	TBD ~2019	Backup service for the FES and RSS
Meteosat-9	21/12/2005	18/07/2006	TBD	Rapid Scan Service (RSS)
Meteosat-10	05/07/2012	21/01/2013	TBD	Prime satellite for the Full earth Scan (FES)
Meteosat-11	15/07/2015	TBD	TBD	Commissioning before in orbit storage

On the MSG satellites the successor of MVIRI is called the Spinning Enhanced Visible and Infrared Imager (SEVIRI). SEVIRI observes the Earth through 12 spectral channels: 11 narrow channels and one broader High-Resolution Visible (HRV) channel. The SEVIRI instrument provides an unprecedented repeat cycle of 15 minutes. The 11 narrow channels are composed of 3 solar and 8 thermal infrared channels in which SEVIRI observes the full Earth's disk with a sampling distance of 3 km at nadir. The Meteosat FOV is scanned from South to North and from East to West. Due to data rate limitations, the HRV channel provides images of only half of the Earth's disk in the East-West direction but with a 1 km resolution at sub-satellite point.

To generate the MVIRI/SEVIRI data record 5 SEVIRI channels are used. These bands and their spectral characteristics are summarized in Table 8.

Table 8: Spectral channel characteristics of SEVIRI in terms of central, minimum and maximum wavelength of the channels, resolution at sub-satellite point, and the main application areas of each channel.

Spectral band	Characteristics of spectral band (µm)			Resolution at sub-satellite point (km)	Main observational application
	λ_{cen}	λ_{min}	λ_{max}		
VIS 0.6	0.635	0.56	0.71	3	Observation of the surface, detection of clouds and retrieval of wind fields (daytime)
VIS 0.8	0.81	0.74	0.88	3	
WV 6.2	6.25	5.35	7.15	3	Determination of the amount of water vapour in the upper troposphere and detection of high level clouds and atmospheric instability
IR 10.8	10.80	9.80	11.80	3	Observation of the surface, detection of clouds, retrieval of wind fields and detection of atmospheric instabilities (day and night)
IR 12.0	12.00	11.0	13.00	3	

The SEVIRI Level 1.5 data are retrieved from the EUMETSAT Data Center in count images of 3712 x 3712 pixels coded on 10 bits. As for MVIRI, those data are retrieved from the original Level 1.0 data by correcting them for undesirable geometrics effects and by geolocating them using the rectified reference projection.

4.2.2 Spectral response of the instruments

All the SEVIRI channels are measured each with three NB detectors, while nine are used for the HRV channel. The normalised spectral response curves of the five SEVIRI channels that are used to generate the CM-23311 and CM-23341 data records are shown as a function of wavelength in Figure 8 for the two VIS channels, in Figure 9 for the WV channel and in Figure 10 for the two IR channels. The corresponding channel of Meteosat-7 is also given in each figure for comparison. All the SR curves were downloaded from the EUMETSAT webpage (data as available on 21th January 2015). For the thermal channels, the SR curves at the nominal focal plane temperature (95 K) have been selected.
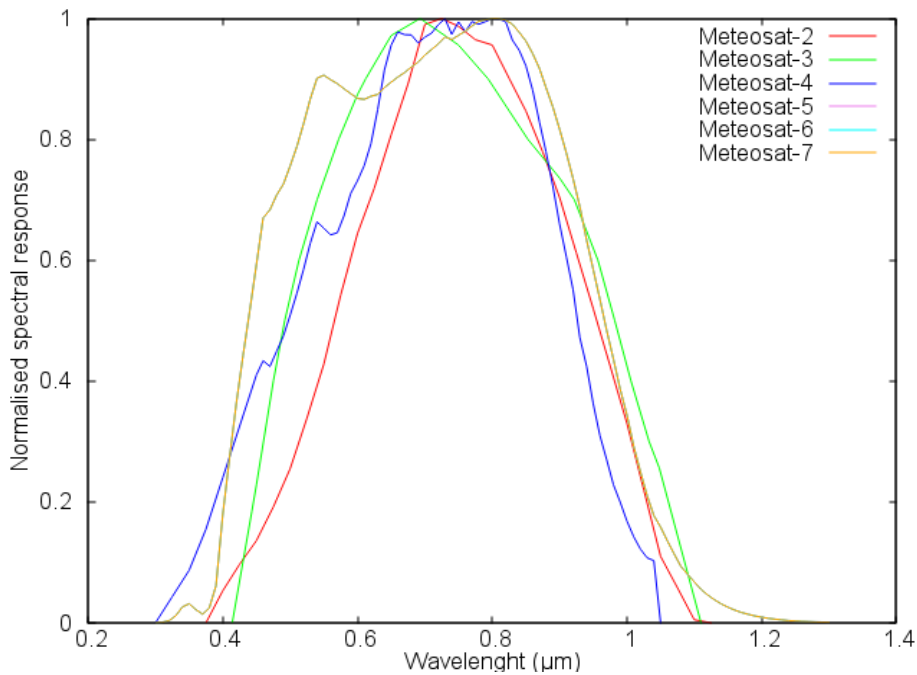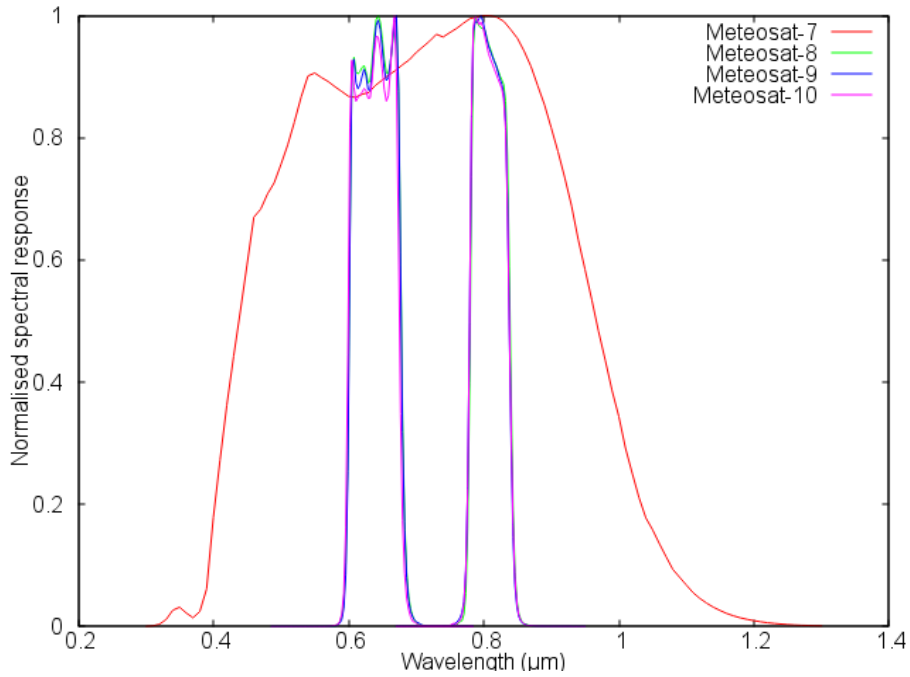
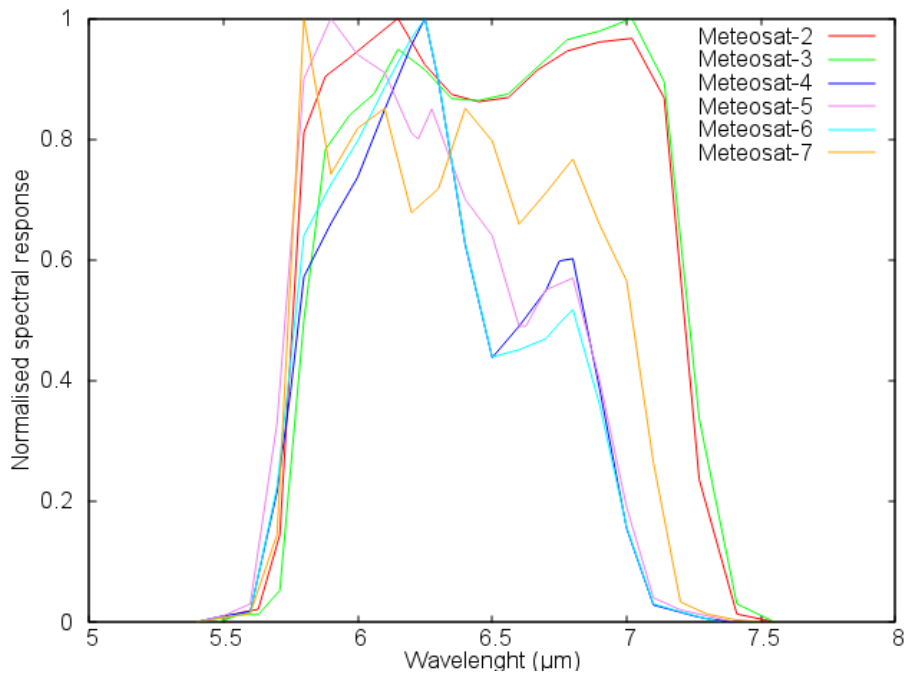**Figure 8: Normalised spectral response curves of the MSG and MET-7 VIS channels**

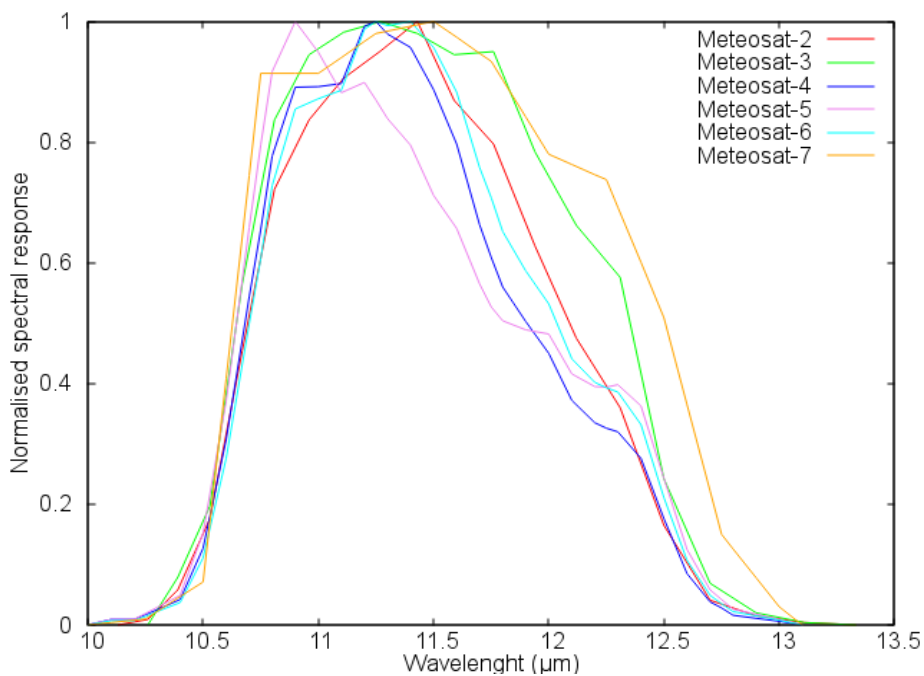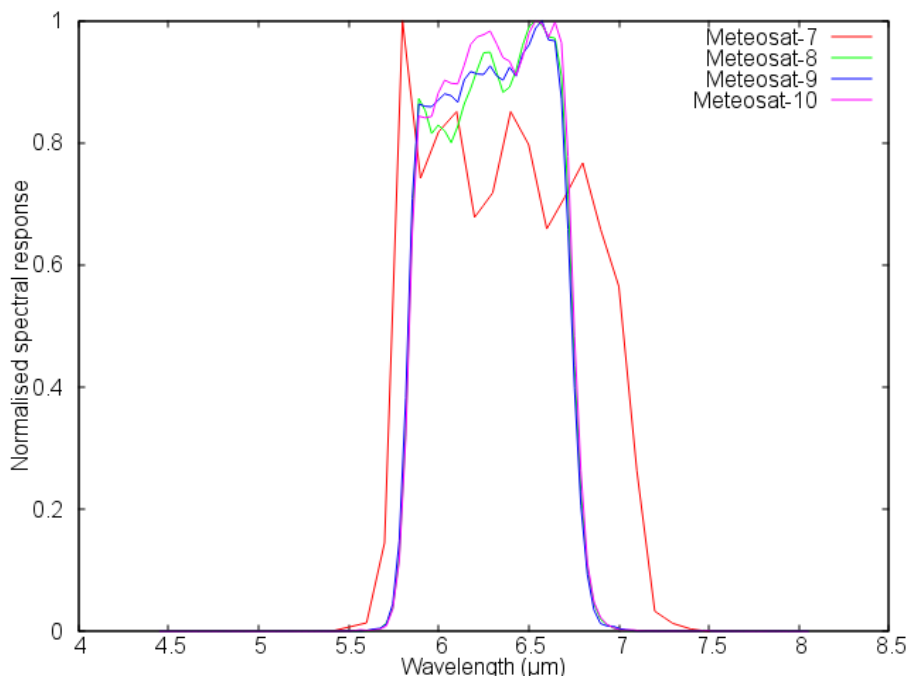**Figure 9: Normalised spectral response curves of the MSG and MET-7 WV channels**
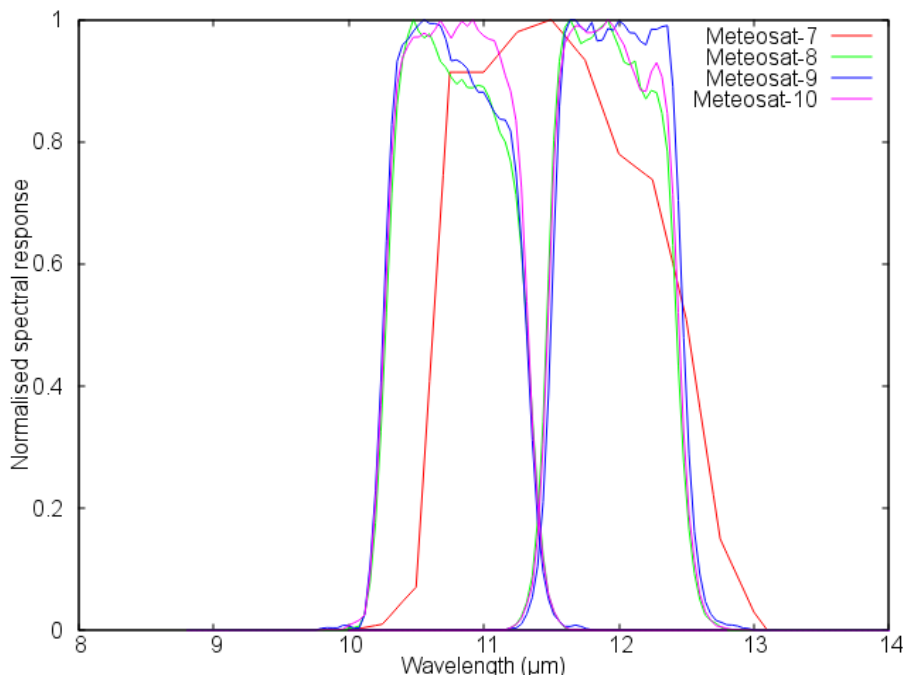
Figure 10: Normalised spectral response curves of the MSG and MET-7 IR channels

4.2.3 VIS 0.6 and VIS 0.8 channels calibration

The SEVIRI VIS 0.6 µm and VIS 0.8 µm channels are calibrated using the latest update of the inter-calibration of SEVIRI with the Moderate Resolution Imaging Spectroradiometer (MODIS) on board the polar-orbiting Aqua satellite. The whole calibration information is provided on the web page of J.F. Meirink at KNMI (http://msgcpp.knmi.nl/mediawiki/index.php/MSG-SEVIRI_solar_channel_calibration). The inter-calibration method, which is described in Meirink et al. (2013), is based on regressions of collocated near-nadir reflectances from the geostationary and the polar-orbiting imagers' solar channels. The NB radiances (L), expressed in $mW.m^{-2}.sr^{-1}.(cm^{-1})^{-1}$, can be obtained from the integer count value (C) provided in the images using a constant offset factor (L_0), expressed in $mW.m^{-2}.sr^{-1}.(cm^{-1})^{-1}$, and a calibration coefficient (c_f), expressed in $mW.m^{-2}.sr^{-1}.(cm^{-1})^{-1}.count^{-1}$ with the following relation:

$$L = c_f.C - L_0$$

To correct for the degradation with time of the instrument's optics and detectors in the visible channels (ageing effect), the calibration coefficient (c_f) is chosen to be linearly increasing over time. As already mentioned in Section 4.1.3, an exponential model would be better suited to capture the ageing process and its saturation in time, however the effect of the VIS channel spectral ageing on the Earth Radiation Budget is limited for MVIRI (Decoster, 2014b) and then presumably also for SEVIRI. The calibration slopes used are the latest updates provided on the web page of J.F. Meirink at KNMI.

According to Meirink et al. (2013), the SEVIRI operational calibration is found to be stable during the years 2004 to 2009, but offset by −8 and −6% for VIS 0.6 µm and VIS 0.8 µm channels, respectively. Uncertainties in the inter-calibration method are estimated to be 1 % and 1.5 % respectively. The full MSG era, including MET-10, was recently updated using

Aqua-MODIS Collection 6 reflectances as a reference. It should be noted that the MET-10 record is still too short to obtain reliable trend estimates.

Finally, the calibration coefficient and the offset are converted to the same units as MFG using the following equations

$$g = 0.001 * c_f * FI$$

$$O_v = -L_0/c_f$$

where FI is the filter integration in (cm-1).

The updated calibration coefficients (expressed in $mW.m^{-2}.sr^{-1}.(cm^{-1})^{-1}.count^{-1}$) and the daily drifts (in $mW.m^{-2}.sr^{-1}.(cm^{-1})^{-1}.count^{-1}.day^{-1}$) from the KNMI SEVIRI recalibration , the offset values (in count), the filter integration (in cm^{-1}) as well as the filtered solar irradiance (FSI, in $W.m^{-2}$) are shown in Table 9 for each MSG satellite.

Table 9: Calibration parameters of the VIS 0.6µm and 0.8µm channels of the Meteosat Second Generation satellites.

Satellite	From	Channel	Calibration coefficient ($mW.m^{-2}.sr^{-1}.(cm^{-1})^{-1}.count^{-1}$)	Offset (count)	Drift per day ($10^{-5} .mW.m^{-2}.sr^{-1}.(cm^{-1})^{-1}.count^{-1}.day^{-1}$)	FI (cm^{-1})	FSI ($W.m^{-2}$)
Meteosat-8	20000101	VIS 0.6	0.024346	51.0	0.03739	1847.1	120.5
		VIS 0.8	0.030989	51.0	0.03111	873.1	63.8
Meteosat-9	20000101	VIS 0.6	0.021026	51.0	0.02556	1784.0	116.3
		VIS 0.8	0.026875	51.0	0.01835	859.5	62.9
Meteosat-10	20000101	VIS 0.6	0.020755	51.0	0.04079	1724.2	113.0
		VIS 0.8	0.025558	51.0	0.06371	855.4	62.6

4.2.4 **WV 6.2, IR 10.8 and IR 12.0 channels calibration**

For the thermal channels, the EUMETSAT operational calibration relies entirely on the internal blackbody that is present on board each MSG satellite (Pili, 2000). This blackbody is used as warm source and the deep space as cold source. The whole calibration information is available in the prologue of the L1.5 Meteosat images. As previously, it needs to be converted to the same units as MFG prior to its use.

Different works have addressed the stability of the MSG thermal channels, e.g. by comparison with IASI in GSICS or by Maidment et al. (2014). Although biases can be identified, the 6.2µm, 10.8µm and 12.0µm channels show a good stability in time and the data can therefore be used in empirical regressions.

4.3 GERB Level 2 data

4.3.1 Introduction

The GERB instruments (Harries et al, 2005) are broadband (BB) radiometers designed to fly on the Meteosat Second Generation satellites (2002-2020). Similarly to its predecessors, GERB provides total wave (TW) and shortwave (SW) radiances, the latter being obtained through a quartz filter. Estimation of the LW radiation is obtained by subtracting the SW from the TW.

The GERB ground processing is distributed between Germany (EUMETSAT), the UK (Rutherford Appleton Laboratory, Imperial College London) and Belgium (Royal Meteorological Institute of Belgium). The GERB processing generates level 2 TOA solar and thermal fluxes into 3 formats:

- The **Averaged Rectified and Geolocated** (ARG, +/- 45km, 17') data for which no attempt is made to correct for the GERB Point Spread Function (PSF).

- The **Binned Averaged Rectified and Geolocated** (BARG, 45km, 15') data which are corrected for the effect of the PSF and also for geolocation and rectification errors. This is achieved by using the fine-scale estimates of the BB radiances inferred from SEVIRI.

- The **High Resolution** (HR, 9km, 15') data which are also produced by combining the fine-scale SEVIRI BB estimates with GERB observations and are provided as instantaneous values at the time of the SEVIRI observations.

The GERB data are not used directly to generate the data records but are used "off-line" to derive narrowband to broadband regressions. To this end, the BARG data from the GERB-2 instruments have been merged with the MVIRI data from Meteosat-7 and SEVIRI data of Meteosat-8. Details are given in Section 7.3.2.

4.3.2 Summary of GERB quality

The primary source of information concerning the quality of the GERB data is the "Quality Summary for GERB Edition 1 L2 ARG Product" (Russell, 2006), available through the GERB project's websites. Strictly, the document only covers the ARG product and is not aimed to document the quality of the HR data.

4.3.3 GERB-2 SW calibration

A recalibration of the GERB-2 instrument has been performed and published in Feb. 2011 by the GERB team: *"(…), all users of the GERB-2 radiation data are advised to multiply all solar (SW) radiances and fluxes by a factor of 0.976. Data so treated should be referred to as SW cal update. This update reduces the difference between Met-8 and Met-9 but does not totally suppress it."* This calibration update is applied in CM SAF. This is of paramount importance for the MVIRI/SEVIRI data record since the empirical narrowband-to-broadband regressions for MVIRI and SEVIRI are based on GERB-2 data.

4.3.4 **GERB SW channel ageing**

Broadband instruments like GERB or CERES are, in general, more prone to temporal degradation in the SW than narrowband instruments, as they are not protected by spectral filters. In [RD7] the GERB-2 SW channel ageing is evaluated at -0.74%/year for deep convective cloud.

In this work the GERB data have not been corrected for ageing. The effect of ageing is limited as only data from 2004-2006 have been used, thus soon after the MSG-1 launch on August 28th 2002.

4.4 **Ancillary data**

4.4.1 **IGBP surface type map**

A fixed surface type map at a spatial resolution of $(1km)^2$ has been compiled from AVHRR data in the frame of the International Geosphere Biosphere Program (IGBP) (Loveland et al., 2000; Townshend, 1994). This map is available from the USGS EROS Data Center (EDC) Distributed Active Archive Center (DAAC) webpage. The version 2.0 of the IGBP surface type map has been re-gridded to the MVIRI and SEVIRI full resolution grids (at $(2.5 \text{ km})^2$ and $(3 \text{ km})^2$ resp.). Each pixel contains therefore a mixture of IGBP pixels from which a map of the surface type is compiled as follows. The 17 IGBP surface classes are first reduced to 5 classes – ocean, desert, bright and dark vegetation, ice/snow – using Table 10. Since the IGBP map is not sufficient to have a good discrimination between dark and bright desert, the desert class is further split according to the CERES classification (and more specifically to the albedo) (Ipe, 2011). This post-discrimination process is performed using a coarser CERES surface type map at 10' resolution (N. Loeb, pers. comm.). This way, the 17 IGBP surface types were aggregated into the 6 types that were used to define the CERES TRMM SW ADMs (Loeb et al., 2003). Then, if more than 50% of the pixels are "ocean" the surface type is set to ocean. Otherwise, the most represented class within each Meteosat pixel is allocated to the pixel. The final reduced IGBP surface type map for the Meteosat FOV is illustrated in Figure 11. Maps of the fractions of the different CERES TRMM land surface types are also computed.

Table 10 : IGBP surface types and corresponding CERES TRMM SW ADMs surface types.

	IGBP Surface type		CERES TRMM SW ADMs surface type
1	Evergreen Needle leaf Forest	2	Dark vegetation
2	Evergreen Broadleaf Forest	2	Dark vegetation
3	Deciduous Needle leaf Forest	2	Dark vegetation
4	Deciduous Broadleaf Forest	2	Dark vegetation
5	Mixed Forest	2	Dark vegetation
6	Closed Scrublands	2	Dark vegetation
7	Open Scrublands	4	Dark desert
8	Woody Savannas	2	Dark vegetation
9	Savannas	3	Bright vegetation
10	Grasslands	3	Bright vegetation
11	Permanent Wetlands	2	Dark vegetation
12	Croplands	3	Bright vegetation
13	Urban and Built-Up	4	Dark desert
14	Cropland/Natural Vegetation Mosaic	3	Bright vegetation
15	Snow and Ice	6	snow
16	Barren or Sparsely Vegetated	5	Bright desert
17	Water Bodies	1	Ocean
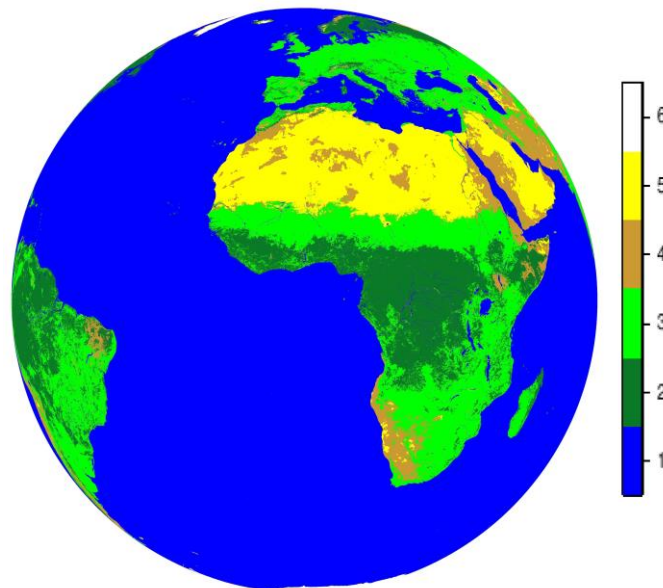
Figure 11: IGBP surface type map for the Meteosat FOV. 1 is ocean, 2 is dark vegetation, 3 is bright vegetation, 4 is dark desert, 5 is bright desert and 6 is ice/snow.

As said, the map of the surface type is fixed and does not account for the changes in vegetation cover that are known to exist in many regions (e.g. the Sahel region). The GERB team is currently developing a temporally varying version of the surface type map, based on the SEVIRI NDVI. This data is expected to improve the TRS fluxes in GERB ED02. This approach is however not directly applicable over the full Meteosat time series as the NDVI can not be estimated from MFG.

4.4.2 Water fraction map

Similarly, the IGBP land mask at (1km)^2 is used to compute the water fraction (WF) for each MVIRI and SEVIRI pixel. This water fraction map is used in the visible clear-sky processing algorithm to perform a post-processing scheme over the pure ocean pixels, i.e. with WF=100%, in an attempt to remove persistent cloudiness. The condition on 100% water fraction ensures that the pixel is not contaminated by coast lines or small islands.

4.4.3 CERES TRMM SW ADMs

The CERES TRMM SW ADMs (Loeb et al., 2003) are derived from 8 months of observations of the Clouds and Earth's Radiant Energy System (CERES) (Wielicki et al., 1996) instrument in Rotating Azimuth Plane Scan (RAPS) mode on board the Tropical Rainfall Measurement Mission (TRMM) satellite. The scene type information is inferred from the Visible and InfraRed Scanner (VIRS) imager on the same platform. Since the TRMM satellite is flying on a sun precessing orbit, these models span the entire SZA range, from the terminator (SZA≈90) to the nadir illumination. This makes the CERES TRMM models well suited to process geostationary satellite observations. On the other hand, as the inclination of the TRMM orbit is only 35° above the Equatorial plane, the mid- and high-latitude regions have not been sampled. The CERES TRMM models are therefore representative of the scenes between 38°S and 38°N but may be less accurate to describe the anisotropy of higher latitudes.

The CERES TRMM SW ADMs are used in the TOA fluxes processing to convert the measured directional radiances into hemispheric fluxes. They are stratified according to the 6 surface types mentioned previously (see Table 10) except snow as well as the cloudiness above these surfaces. Figure 12 shows the variation of the TOA albedo as a function of the SZA for those surface types. For the clear ocean, the "all wind speeds" model is used. The cloudiness is characterised by its cloud phase (water or ice cloud), the cloud fraction over the footprint and the average cloud optical depth over the cloudy part of the footprint.
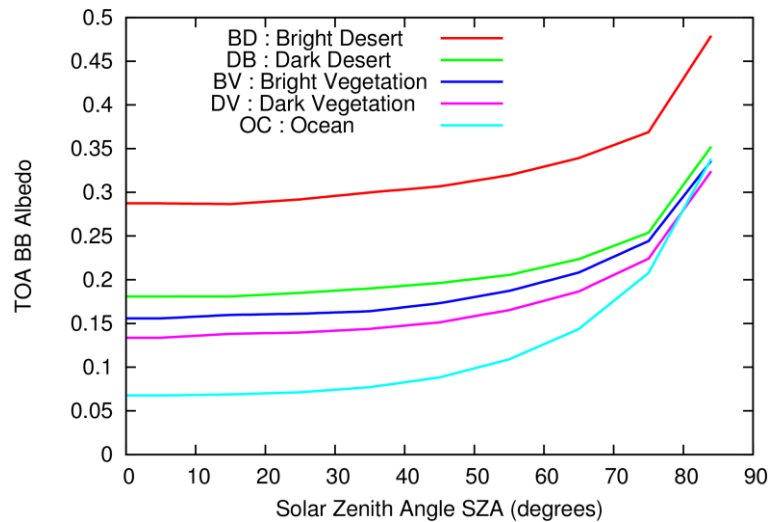
Figure 12: TOA BB albedo provided in the CERES TRMM SW ADMs (from [RD 7]). The ocean curve corresponds to the "all wind speeds" curve.

4.4.4 ERA-Interim wind speed data

Wind speed data are used in the selection of the appropriate clear (cloud fraction = 0%) ocean (water fraction of 100%) CERES TRMM SW ADM in order to convert the SW radiances into fluxes. The CERES TRMM ADMs are defined for wind speeds (ws) < 3.5 m/s, 3.5 m/s < ws < 5.5 m/s, 5.5 m/s < ws < 7.5 m/s and ws > 7.5 m/s.

Wind speeds from the ERA Interim Reanalysis (Simmons et al., 2007; Dee et al., 2011) from the European Centre for Medium-Range Weather Forecasts (ECMWF) have been used over the whole data record period (1983 - 2015). ERA-Interim is a reanalysis of the global atmosphere starting in 1979 and continuing in real time. It replaces the ERA-40 reanalysis (Uppala et al., 2005) which covers the time period 1957-2002. The spatial resolution of the data record is +/- 80 km on 60 vertical levels from the surface up to 0.1 hPa. The ERA-Interim wind speed data consist of eastward and northward components computed at a height of 10 meters. The 10m wind speeds (10u and 10v) have been collected from the ECMWF archive (MARS) under the GRIB format at a spatial resolution of 0.7° x 0.7° and at a 6-hourly temporal resolution. They have then been re-gridded at the MVIRI and SEVIRI full resolution by bilinear interpolation. A linear temporal interpolation is performed between the 6-hourly fields of the reanalysis.

4.4.5 Cloud persistence climatology map

The cloud persistence is here defined as the maximum number of successive days a region may remain cloud covered. The cloud persistence climatology map is based on the climatology of cloud frequencies over the Meteosat FOV from the International Satellite Cloud Climatology Project (ISCCP) (Rossow and Schiffer, 1999), shown in Figure 13(a). More specifically, the cloud persistence, expressed in days, is retrieved from the ISCCP D2 annual mean cloud cover by taking into account the three following constraints about persistent cloudiness and transient surface variability areas:

- A minimum of 20 days over the regions with the lowest cloud occurrences to guarantee insensitivity to cloud shadows,

- A maximum of 60 days over the regions with persistent cloudiness to ensure the stability of the underlying surface reflectances,

- A time period of 30 days shows good performance over regions with a cloud amount of about 50% (such as the Sahel region) and removes the cloud artifacts due to seasonal changes of the vegetation (dry-wet seasons).
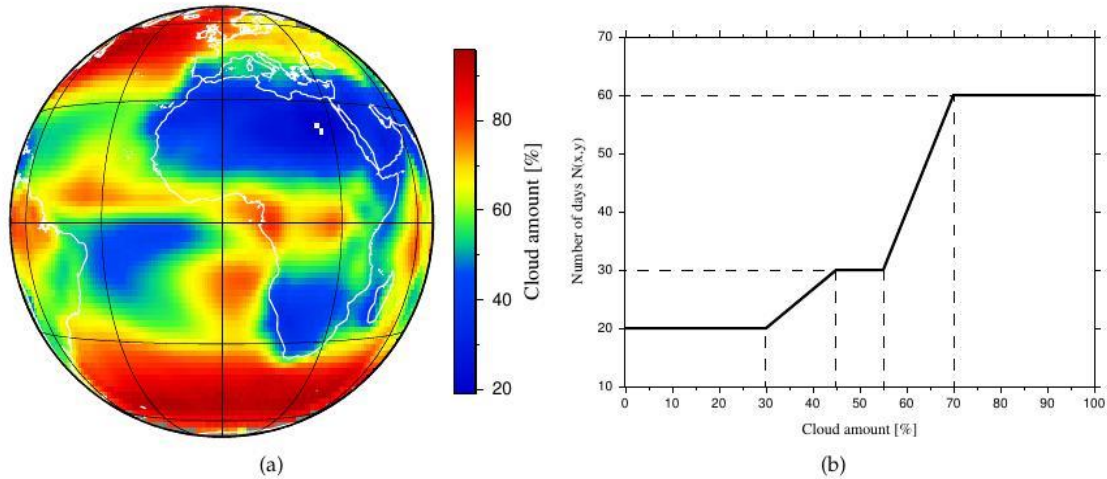
Figure 13: (a) ISCCP D2 annual mean cloud cover for Meteosat FOV and (b) time period mapping of the cloud amount (from Ipe, 2011).

For simplicity, linear transitions are selected between the three plateaus (see Figure 13(b)). The resulting cloud persistence climatology map is shown in Figure 14.
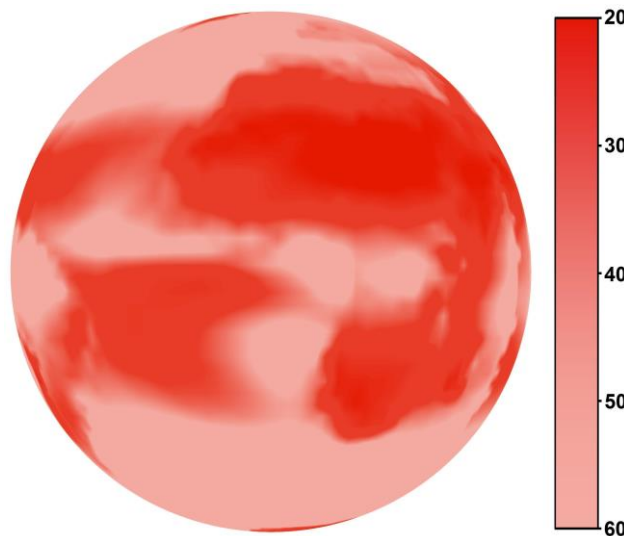
Figure 14: Cloud persistence climatology map over the Meteosat FOV.

4.4.6 **Total Solar Irradiance Composite**

In this first edition of the data records, the Total Solar Irradiance (TSI) composite that has been used is the daily time series produced at RMIB by the group of Steven Dewitte. As it starts in 1981, it covers the full temporal extent of the data records (1983-2015). The methodology used to obtain this TSI composite is described in Mekaoui and Dewitte (2008). It is based on TSI measurements provided by multiple instruments. In particular, the Differential Absolute Radiometer / Variability of solar Irradiance and Gravity Oscillations (DIARAD/VIRGO) instrument on board the Solar and Heliospheric Observatory (SOHO) satellite provides the most frequently updated measurements (Dewitte et al, 2004). The TSI absolute level has been revised following Dewitte et al. (2012) and Janssen et al. (2013) and is about 1362.8 W/m^2. The RMIB TSI composite is shown in Figure 15.
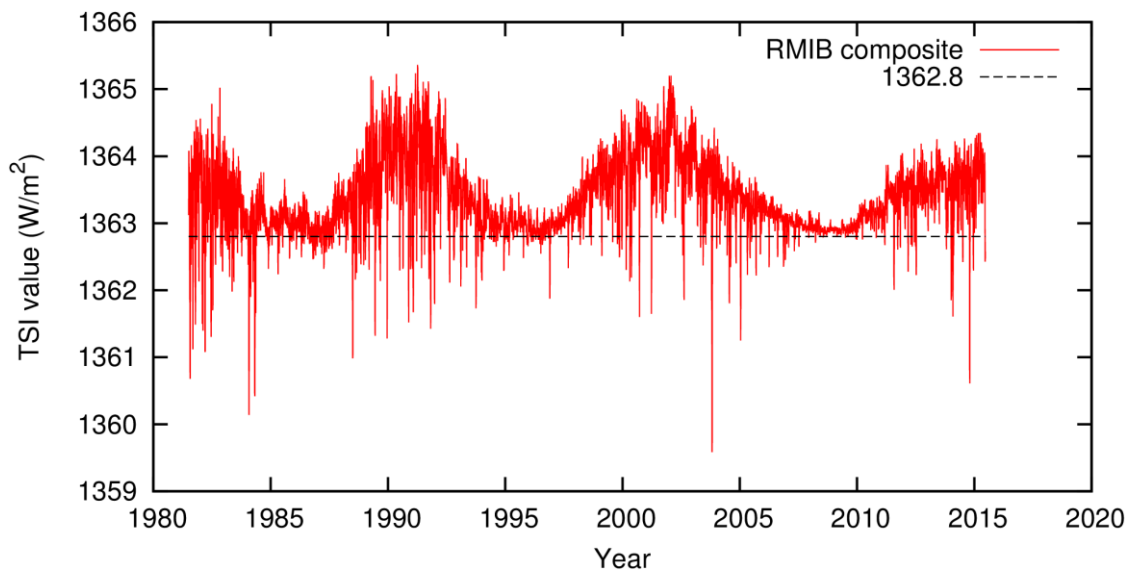
Figure 15: TSI composite produced at RMIB (Steven Dewitte, pers. comm.)

It is worth to mention that the TSI level in this time series is about 2 W/m^2 higher than the values obtained on the state of the art TIM instrument on the SORCE satellite.

5 Algorithm Description (part 1/4): Visible clear-sky processing

5.1 Purpose of the visible clear-sky processing

The objective of this first part of the processing is to estimate the clear-sky VIS image that would have been observed in the absence of any cloud. Figure 16 shows an example of clear sky image (right) with the corresponding all-sky image (left) for 10 June 1995 at noon. The clear-sky images are computed at the full spatial and temporal resolution of the MVIRI and SEVIRI instruments.

The visible clear-sky data are used to perform the scene identification and to "unfilter" the MVIRI and SEVIRI reflectance to estimate the broadband unfiltered reflectance needed for the computation of the TOA fluxes.
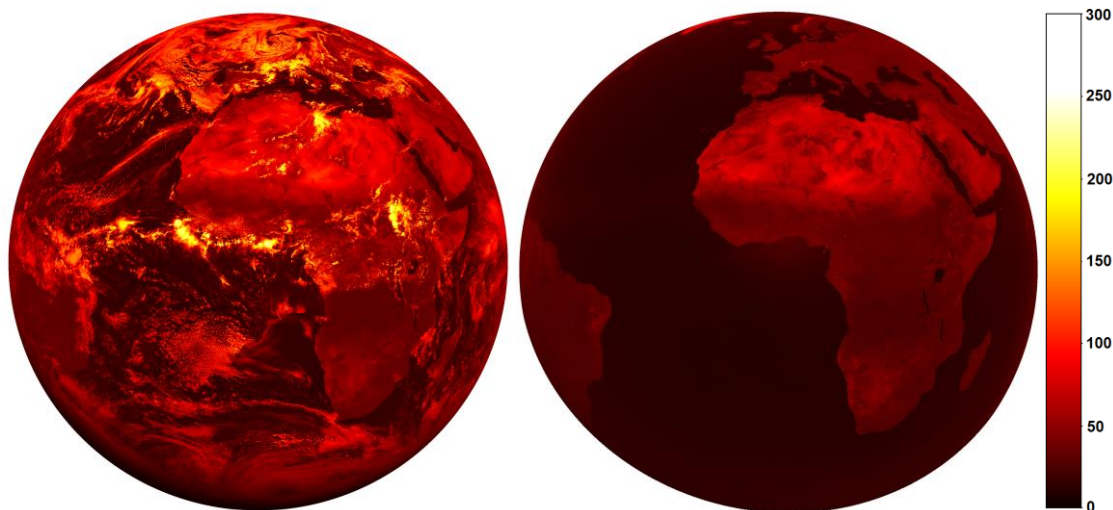
Figure 16: All-sky VIS image (left) and corresponding VIS CS product (right), expressed in counts, for 10 June 1995 at noon.

5.2 Algorithm overview

The estimation of the visible clear-sky is based on the approach developed in Ipe et al. (2003). This method accounts for the main sources of variation within TOA measurements, making it one of the best approaches to isolate changes in atmospheric conditions and therefore to estimate clear-sky conditions. Further improvements have been introduced in high latitudes' regions associated to persistent cloudy conditions where cloud contamination was still observed.

The visible clear-sky processing is based on a buffer of N days of visible data. To estimate the clear-sky image for the repeat cycle hhmm for a given day 'D', the algorithm can use data for up to (N-1)/2 days before and (N-1)/2 days after 'D'. Figure 17 gives an overview of the recursive loop while the logic of the clear-sky VIS processing algorithm is given in Figure 18.

D = first day

Initialisation : read VIS data for $\frac{N-1}{2}$ before to $\frac{N-1}{2}$ after the first day (D) (same repeat cycle hhmm)

D = next day

VIS clear-sky processing for day D

Trash data for $D - \frac{N-1}{2}$ (replace by) Read data for $D + \frac{N-1}{2} + 1$

D < last day

Clear-sky DC

Day = last day → end
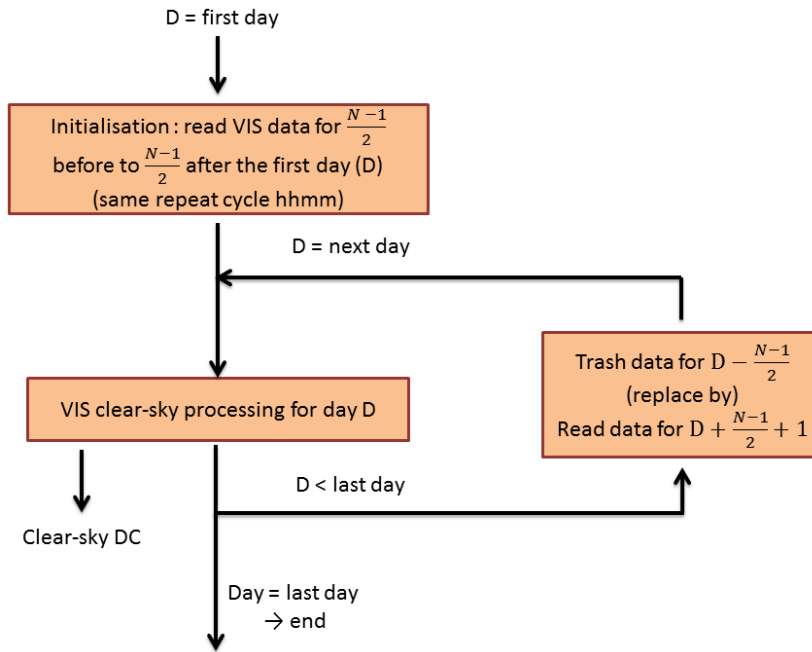
Figure 17: Overview flowchart for the visible clear-sky processing algorithm. The inputs are TOA VIS measurements in DC units. The clear sky VIS outputs are also expressed in DC.

Data from $\frac{N-1}{2}$ before to $\frac{N-1}{2}$ after day D

DC → reflectance

Computing the ratios' vector of length N

Reducing vector length using cloud climatology

Taking 4th lowest value of ratios' vector

Ocean post processing

Ratio → DC

Writing CS image

End of the processing of day D
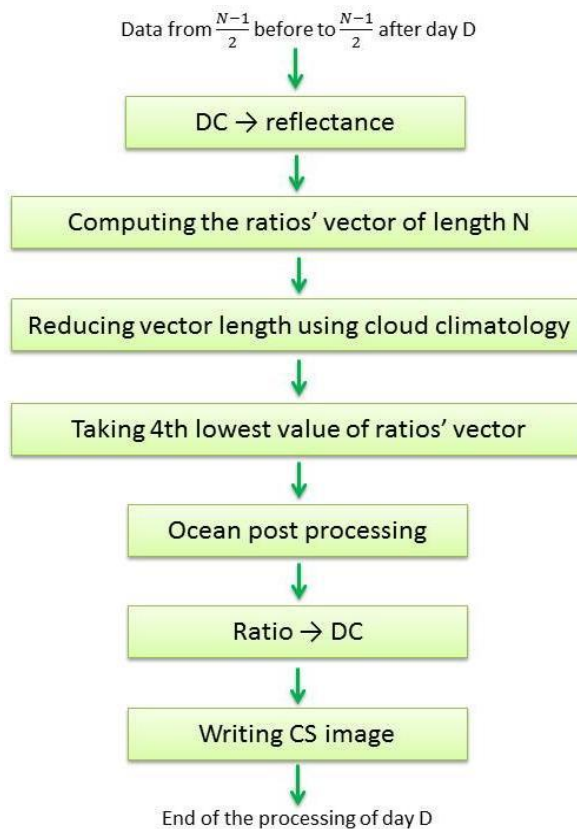
Figure 18: Overview flowchart for the clear-sky VIS processing algorithm for day D included in the visible clear-sky processing recursive loop shown in Figure 17.

42

5.3 Algorithm description

5.3.1 DC to reflectance

The SEVIRI Solar Channels Calibration (SSCC) (Govaerts et al., 2004) and the KNMI SEVIRI recalibration (Meirink et al., 2013) are used respectively to convert the MVIRI and SEVIRI measurements from DC to radiances following the method already exposed in Section 4.1.3. The calibration coefficient (g) is obtained by adding to the reference calibration coefficient (g_{ref}) the number of days since the reference date (N) multiplied by the daily drift (D) and by a constant factor of 10^{-5}

$$g = g_{ref} + D.N.10^{-5}$$

The launch of the satellite is taken as reference for MFG while the 1st Jan 2000 is taken for all the MSG satellites. The values of the calibration coefficient and drift were previously given in Tables 6 and 9, respectively, for each of the MVIRI and SEVIRI instruments.

The radiances (L) are then converted into reflectances (ρ) using the filtered solar irradiance (*FSI*, also given in Tables 6 and 9) of the instrument, the Earth-Sun distance (d) and the solar zenith angle (*SZA*)

$$\rho = \frac{L.\pi.d^2}{FSI.\cos(SZA)}$$

5.3.2 Ratio computation

The method of Ipe et al. (2003) to estimate the composite TOA clear-sky visible reflectances is built on the fact that a time series of chronological daily visible measurements can be split into three components:

- A base curve representative of the clear-sky conditions,

- A component representing the clouds contributions to the pixel signal (in general a positive effect),

- A cloud shadows effect, for areas with broken clouds, responsible for a decrease in the reflectance of neighboring pixels below the expected clear-sky value (negative effect).

The clear-sky CERES SW broadband ADMs (Loeb et al., 2003) are used to extract the visible clear-sky base curve from the signal. These models only depend on the surface type and the scene geometry: the solar zenith angle (SZA), the viewing zenith angle (VZA) and the relative azimuth angle (RAA). These angles are illustrated in Figure 19. The clear-sky SW CERES curve, ρ_c, and clear-sky visible Meteosat base curve, ρ_{cs}, are assumed to only differ by a constant multiplicative factor over some temporal extend, N

$$\rho_{cs} = \alpha.\rho_c$$

In Ipe et al. (2003), this multiplicative factor α is determined by taking the fifth percentile of the ratios between the Meteosat visible reflectance and the associated clear-sky SW CERES

reflectance over the whole period of time N. It appears that the best choice to correctly estimate the clear-sky VIS reflectance was to set the base period of time N equal to 60 days.
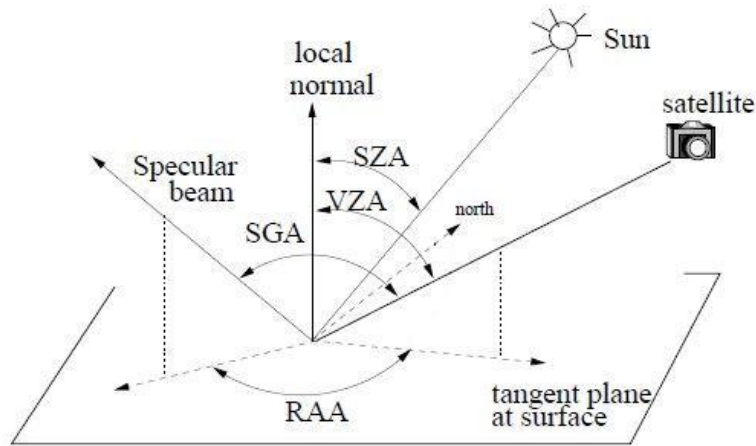
Figure 19: Definition of the Solar Zenith Angle (SZA), Viewing Zenith Angle (VZA), Relative Azimuth Angle (RAA), and Sun Glint Angle (SGA).

As shown in Figure 17, the clear-sky processing described above is applied inside a recursive loop. During the initialization of the process, the 30 VIS images before to 30 after the considered day D (at the considered repeat cycle) are read and the clear-sky process is applied for each pixel. The ratios are computed for the 61 days and kept in memory inside a vector. The VIS clear-sky image of day D is computed from those ratios. At the second iteration, the oldest ratio value (day D-30) is discarded from the vector and the ratio for day D+31 is computed. This new value is added at the end of the vector and the VIS clear-sky image of day D+1 is generated. For each following day, the same procedure is applied. This recursive loop allows processing the VIS clear-sky images for a long period of time while substantially saving CPU resources.

5.3.3 Cloud climatology

Because a longer time span seems useful for regions with high cloud persistence while it is the opposite for low clouds occurrence regions, a cloud climatology is used to select an adequate time span for each pixel. The cloud climatology is described in details in Section 4.4.5.

A fixed maximum span of 61 days appeared to be the best choice to estimate the clear-sky reflectance as a higher value did not lead to a higher correlation. On the other hand, a minimum span of 20 days was fixed over the regions with the lowest cloud occurrences to guarantee insensitivity to cloud shadows.

5.3.4 4th lowest value

Selecting the 5th percentile (or any other constant percentile) to compute the clear-sky reflectance appears problematic when taking shorter time spans. Indeed, such a criterion does not allow discarding all the observations contaminated by the cloud shadows of neighboring pixels. These observations would therefore mistakenly be considered as clear-sky values. For this reason the 4th lowest value in the ratios' vector was taken instead. This means that each time span is expected to contain no more than 3 days contaminated by

cloud shadows or at least 4 clear days. This approach results in similar clear-sky ratios without the previously mentioned issues.

5.3.5 **Ocean post-processing**

Despite significant improvements in the estimation of the composite TOA clear-sky visible reflectance with respect to the method developed in Ipe et al. (2003), some cloud contamination still remains. Those clouds are mainly located in high latitudes, in particular in oceanic regions like the Southern Ocean or region close to Greenland. Since oceanic regions are characterized by spatially homogeneous reflectance, a spatial filter was applied over the oceans to remove the effect of persistent cloudiness. Only the ratios from neighboring pixels having a water fraction equal to 100% are compared to each other. These pixels are selected from inside a moving window with a specific sampling. The number of neighboring pixels located inside this window was chosen to be constant across the whole Earth's disk. This number was found to be optimal when fixed at 23 x 23 samples. Moreover, the sampling distance inside the window was chosen to be dependent on the cloud persistence given that the clear-sky pixels are scarcer and more scattered in cloudier regions. It implies a spatial dependency of the sampling distance as illustrated in Figure 21 by the green boxes. For each ocean pixel, the cloud persistence climatology $C(x,y)$ was used to adjust the sampling distance inside the moving window according to the nearby cloud persistence. The sampling distance S is obtained using

$$S = \begin{cases} 1 & \text{if } C(x,y) < 30 \\ 1 + \frac{12.(C(x,y)-30)}{30} & \text{if } 30 \leq C(x,y) \leq 60 \\ 13 & \text{if } C(x,y) > 60 \end{cases}$$

As the objective is to remove any persistent cloud, a low percentile of 2% of the subset of the neighboring pixels' clear-sky ratio values is used. However, the choice of a constant percentile is problematic when looking at the vicinity of the sun glint spot. Indeed, sun glint pixels are much brighter than other pixels and thus, taking the second percentile over a window of mixed pixels would most likely lead to consider by mistake the non sun glint pixels as clear-sky estimate. For this reason the percentile was chosen to vary according to the Sun Glint Angle (SGA, illustrated in Figure 19) as shown in Figure 20.
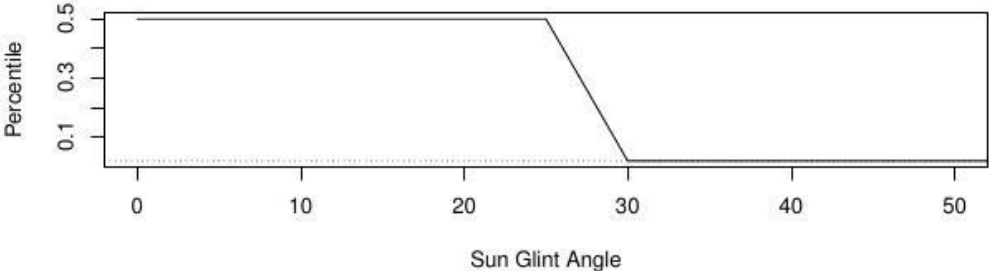
Figure 20: Dependence of the percentile on the SGA.

The effect of the ocean post-processing on the estimation of the composite TOA clear-sky VIS reflectance is illustrated in Figure 21. The cloud contamination is significantly reduced over oceanic regions with persistent cloudiness.
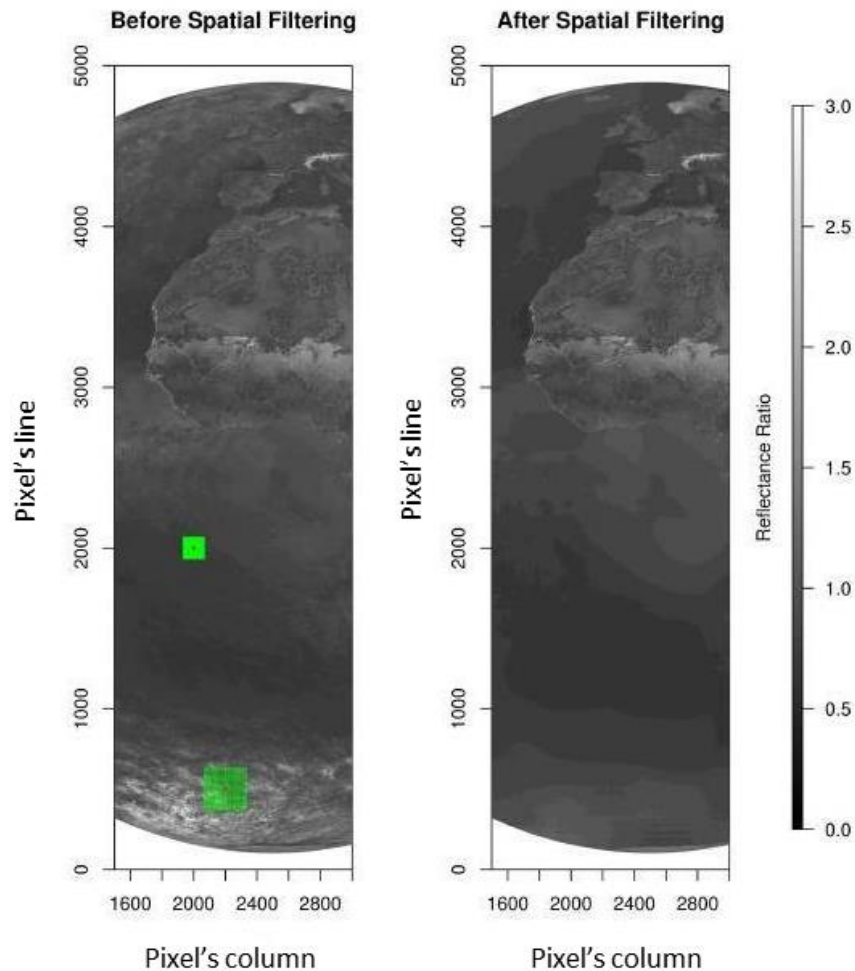
Figure 21: Effect of the spatial filtering used in the ocean post-processing for the 1st March 2004 at 12:00 UTC. The green boxes illustrate the size of the filtering window depending on the cloud persistence climatology.

The algorithm also provides a fast option that allows saving CPU resources by performing the ocean post-processing on a reduced grid. The spatial filtering is then performed every 10 pixels and a bilinear interpolation is used to infer the ocean ratios of the remaining pixels. This option is enabled by default.

5.3.6 Clear sky ratio to digital counts

The estimate of the clear-sky ratios are then reconverted into reflectance using the appropriate CERES TRMM model according to the scene type. Specifically, the Meteosat clear-sky VIS reflectances are re-obtained by multiplying the ratios by the clear-sky SW CERES reflectance corresponding to the same geometry. The reflectance values are then converted back into radiances and finally into digital counts. This leads to VIS images consistent with the original level 1.5 images (i.e. in counts that follow the ageing) but with the cloud removed.

5.4   Algorithm validation

Validation of the main part of the visible clear-sky processing algorithm (section 5.3.2) can be found in Ipe et al. (2003). This section summarizes the validation of the improvements that are proposed to this method.

The leave-one-out cross-validation method was applied to optimally estimate the parameters used in the processing, such as the time period or the threshold criterion for the clear-sky estimation as well as the number of neighboring pixels for the ocean post-processing. This method consists in discarding the considered pixel while computing its clear-sky value. It means that a period of time of N-1 days is used instead of N days. Since the objective is to evaluate the ability of the processing to accurately estimate the clear-sky conditions, the considered pixel is specifically chosen as a known clear pixel. The CM SAF MSG/SEVIRI CMa cloud mask (doi 10.5676/EUM_SAF_CM/CMA_SEVIRI/V001) is used for this purpose. The estimated value and the measured value are then compared to each other to evaluate the method using Taylor diagrams (Taylor, 2001). Such diagrams give a graphical representation of how well estimates match the actual observations. Estimates and observations are compared using their correlation (circular axis), their normalised root mean square (RMS) difference (grey circles emanating from the bottom axis) and the amplitude of their variations, i.e., their normalised standard deviations (SD) (left and bottom axis).

To determine the optimal period of time allowing to accurately estimate the clear-sky condition, various time periods were used to run the processing and the estimated values were then compared to the real measured value. The comparison is given in Figure 22 for 1st Mar. 2004 at 12:00 UTC, distinguishing between frequently cloudy areas (circles) and frequently clear areas (triangles). Note that for this Figure the number of days 'N' corresponds to the value (N-1)/2 in the algorithm overview (Section 5.2). It can be noted that any period of time longer than two days (N=1, i.e. one before and one after the considered slot) leads to a good agreement over frequently clear regions. However, a slight downgrade appears for periods longer than 20 days (N=10). On the other hand, clear-sky estimates over regions with persistent cloudiness improve with longer period of time. However a period longer than 60 days (N=30) does not lead to higher correlation while it reduces the variability. The optimal maximum time period of 60 days (61 considering the central slot) is therefore justified.
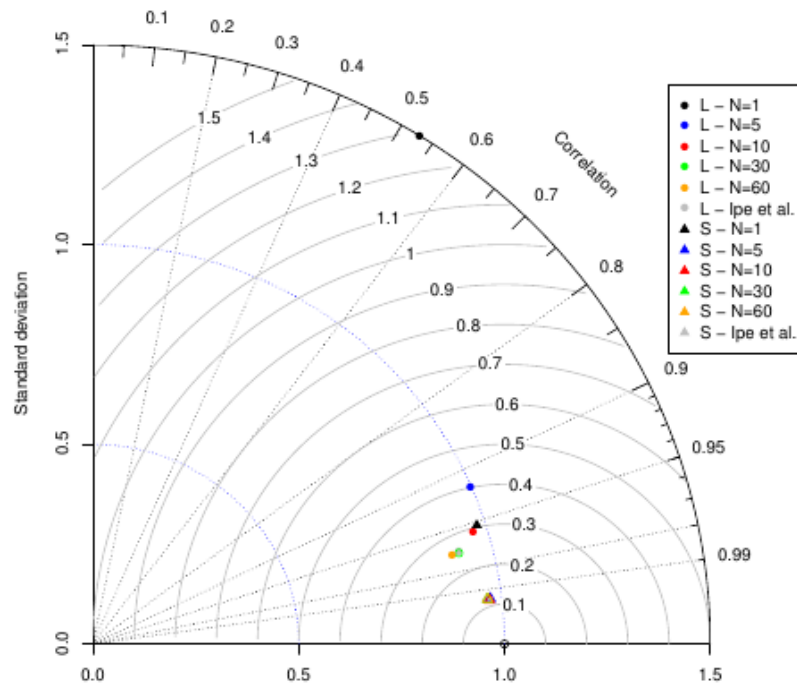
Figure 22: Taylor diagram of the clear-sky estimates for various period of time. Circles (denoted as L in the legend) correspond to frequently cloudy areas while triangles (denoted as S) correspond to frequently clear areas.

As mentioned before (see section 5.3.4), selecting any constant percentile to compute the clear-sky reflectance does not allow discarding all the shadowed observations from the ratios' vector when considering short periods of time. An alternative to the percentile is a uniform threshold criterion applied on the chronologically organised vector regardless of its length which consists in taking its nth smallest ratio's value. To determine the optimal threshold, the clear-sky conditions were estimated using various threshold values and were then compared to the real measured value. As it can be seen in Figure 23, higher correlations are found over the tropics, the ocean and the vegetation for lower threshold value. However, only higher thresholds lead to high standard deviations. Over desert, taking the 3rd lowest value provide a slightly lower correlation. Globally, estimates vary little according to the threshold. As a compromise between capturing variability and maintaining high correlation, the 4th lowest value is chosen as the optimal threshold.

Figure 23 shows results for the slot of 12:00 UTC on 1st Mar. 2004. Similar results were obtained by changing the slot even though higher thresholds are slightly performing better for higher SZA due to the increase of shadow contamination.
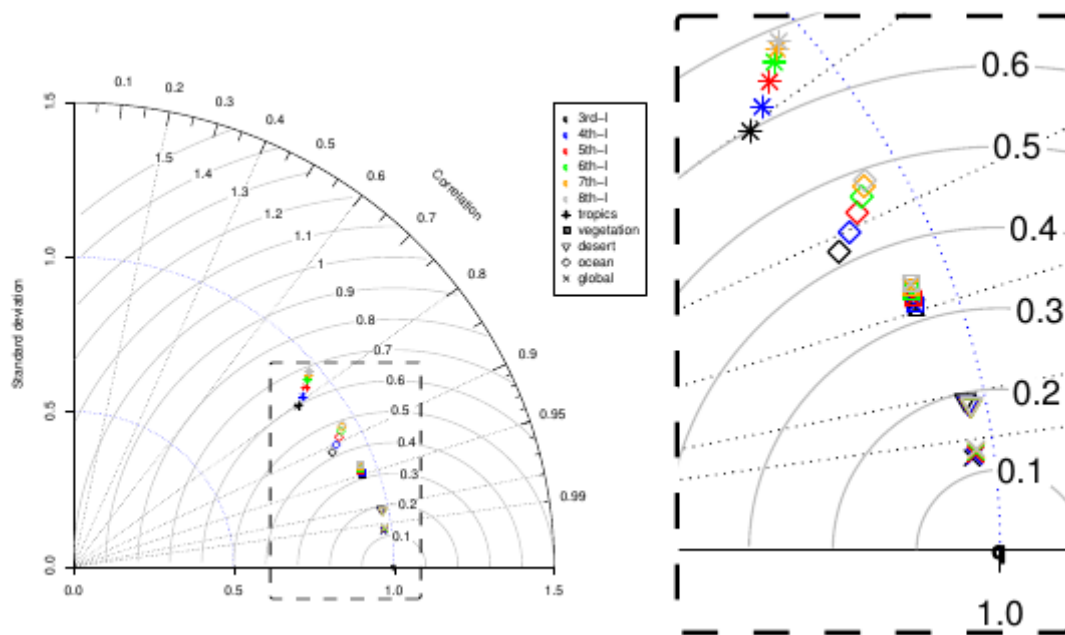
Figure 23: Taylor diagram of the clear-sky estimates for various threshold criterions. Results are shown for tropical regions (stars), vegetated surfaces (square), deserts (triangle), oceans (diamond) and for all surfaces included (cross). A zoom of the rectangular section is given on the right.

To remove the remaining effect of persistent cloudiness a spatial filter is applied over the ocean pixels where cloud contamination can still be observed. This spatial filter consists in the comparison of ocean neighboring pixels from inside a moving window with a sampling distance varying according to the local cloud persistence. As the sampling distance is fixed by the local cloudiness, the number of pixels involved in the ocean post-processing only depends on the grid size. To determine the optimal number of neighboring pixels to be considered inside the moving window, the clear-sky conditions are estimated using various grid sizes and are then compared to the real measured value over a clear ocean region. As shown in Figure 24 for 1 Mar. 2004 at 12:00 UTC, ocean areas with low cloud persistency (stars) do not optimally require any spatial filtering. The second best option involves 23x23 samples and gives the highest correlations and lowest RMS values. Considering all ocean areas altogether, the option without spatial filtering gives the highest variability but shows low correlations. All estimates are independent of the grid size. The optimal number of neighboring pixels considered inside the moving window is then selected to 23 x 23 samples.
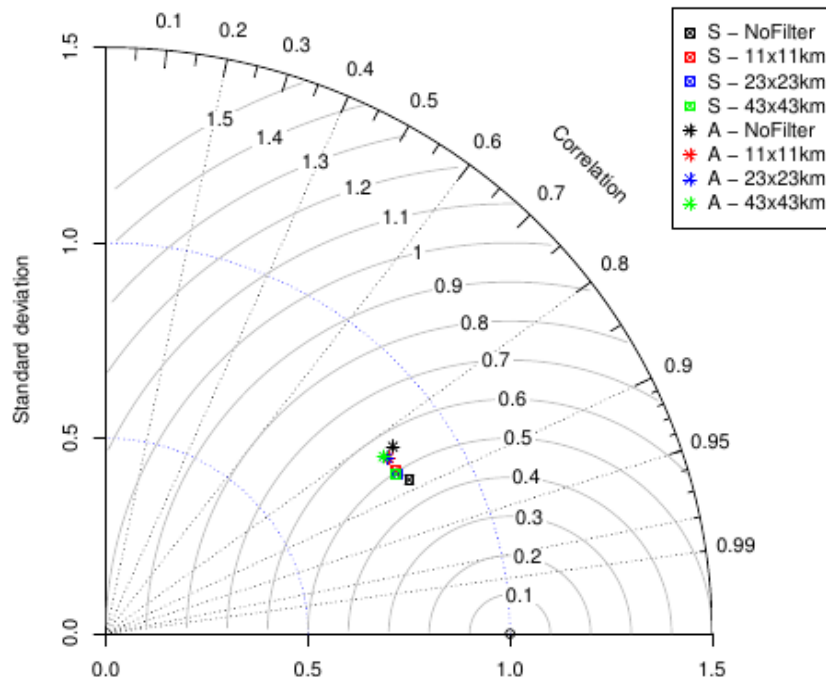
Figure 24: Taylor diagram of the clear-sky estimates for various grid sizes within the ocean post-processing. Stars indicated pixels over frequently clear ocean areas while squares indicate pixels over all kind of ocean areas.

As those parameters are optimised from measurements made only during the month of March 2004, the algorithm performance was then investigated over the whole year (data available from February until December). Contrary to what was done before, the clear-sky conditions were estimated including the considered slot, i.e., for a period of time of N days. Figure 25 shows the cloud-free fraction (panel A), the bias (panel B) and the RMS error (panel C) of the estimates over the year 2004 for various surface types. For all types, the cloud-free fraction appears relatively stable over the year. However, the bias and the RMS error surprisingly appear more significant in March than during the other months of the year. The clear-sky conditions are globally underestimated during this month, mostly due to vegetation and ocean surfaces. It appears to be the consequence of a temporal instability of those surface parameters. For vegetated surfaces, a comparison with maps on phenological transition dates (Zhang et al., 2006) led to the conclusion that it was due to a rapid change in vegetation greenness. For oceanic surfaces, based on Goudie and Middleton (2000), severe dust storm events seem to be the cause of this temporal instability. It should be noted that polar regions are prone to sea ice and snow leading to very high biases. Apart from March, a global bias of 1 to 2 DC in the clear-sky estimation is observed over the whole year.
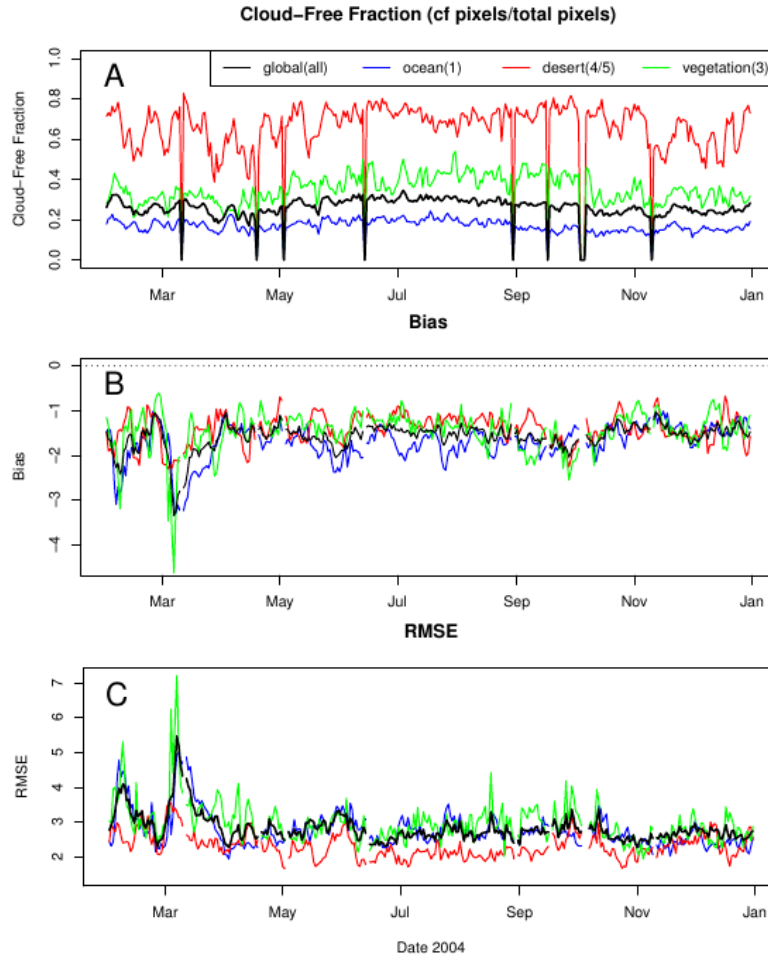
Figure 25: Cloud-free fraction (A), bias (B) and RMS error (C) of the clear-sky estimates for the year 2004 (from Feb. until Dec.) according to various surface types (colored curves) and the full FOV (black curve). Missing data appearing as zero values in the cloud-free fraction were excluded from the bias and RMS error time lines.

5.5 Assumptions and limitations

The visible clear-sky processing algorithm relies on the following assumptions.

- The CERES TRMM SW BB ADMs derived for broadband unfiltered solar reflected radiation can be used for the Meteosat VIS channels.

- The ocean post-processing assumes ice free ocean. This leads to mask the radiances increase due to sea ice during some seasons in the region between 45°S and 60°S.

- It is considered better not to mix data from different satellites in the N-days buffer and thus in the clear-sky products. Indeed, jumps are expected in the multi-satellite data record for clear-sky scenes due to the spectral ageing (Decoster et al., 2013a, 2013b, 2014a; Decoster, 2014b).

5.6 Future enhancements

- Instead of using a single annual cloud climatology map, one may consider seasonal or even monthly climatology maps.

- The fixed surface map could be replaced by a seasonal varying surface map.

- A further improvement could be the use of a dynamic surface map, especially for vegetation and desert according to the NDVI as foreseen for the GERB Edition 2 processing.

- Another possible investigation could be to adapt the clear-sky algorithm parameters according to the surfaces (e.g. vegetation, snow and ice).

6 Algorithm Description (part 2/4): Data preprocessing

6.1 Purpose of the data preprocessing

The objective of the data preprocessing is to perform several corrections on the input data such as calibration, ageing correction, stripes' interpolation and conversion to an equivalent Meteosat-7 signal. Those manipulations are required to generate a homogeneous time series of TOA fluxes. Currently, efforts are done by agencies like EUMETSAT in view of reprocessing their satellite observation records in homogeneous data records called Fundamental Climate Data Record (FCDR). Once Meteosat FCDRs will be available for the VIS, WV and IR channels, the preprocessing described in this section will not be necessary anymore.

The input data consist of the Level 1.5 data from the visible, water vapour and infrared channels of the imager as well as the CS visible estimate evaluated during the previous VIS clear-sky processing step. All those data are given in digital count units. They are converted to MET7-like signal. Meteosat-7 is selected as reference because of its temporal overlap with GERB during the period 2004-2006.

The output data are given in different units according to the channel. The visible and CS visible data are expressed in reflectance, the water vapour data in radiances while the infrared data are in radiances as well as in brightness temperatures. The temporal resolution of the outputs is equal to 30 minutes for MFG and 15 minutes for MSG.

6.2 Algorithm overview

Figure 26 shows the main steps of the data preprocessing.

For MSG, data from two narrow channels are combined to estimate the VIS (from the VIS 0.6 and VIS 0.8) and the IR signals (from the IR 10.8 and IR 12.0). For the WV signal, only data from the WV 6.2µm channel is used.

For the MVIRI instruments, an additional correction needs to be performed when stripes are present in the VIS images. The missing lines are interpolated from the 2 adjacent lines.

Then, calibration (including ageing correction) and conversion to MET7-like are performed. These MET7-like data are expressed in radiances, reflectances or brightness temperatures depending on the channel.
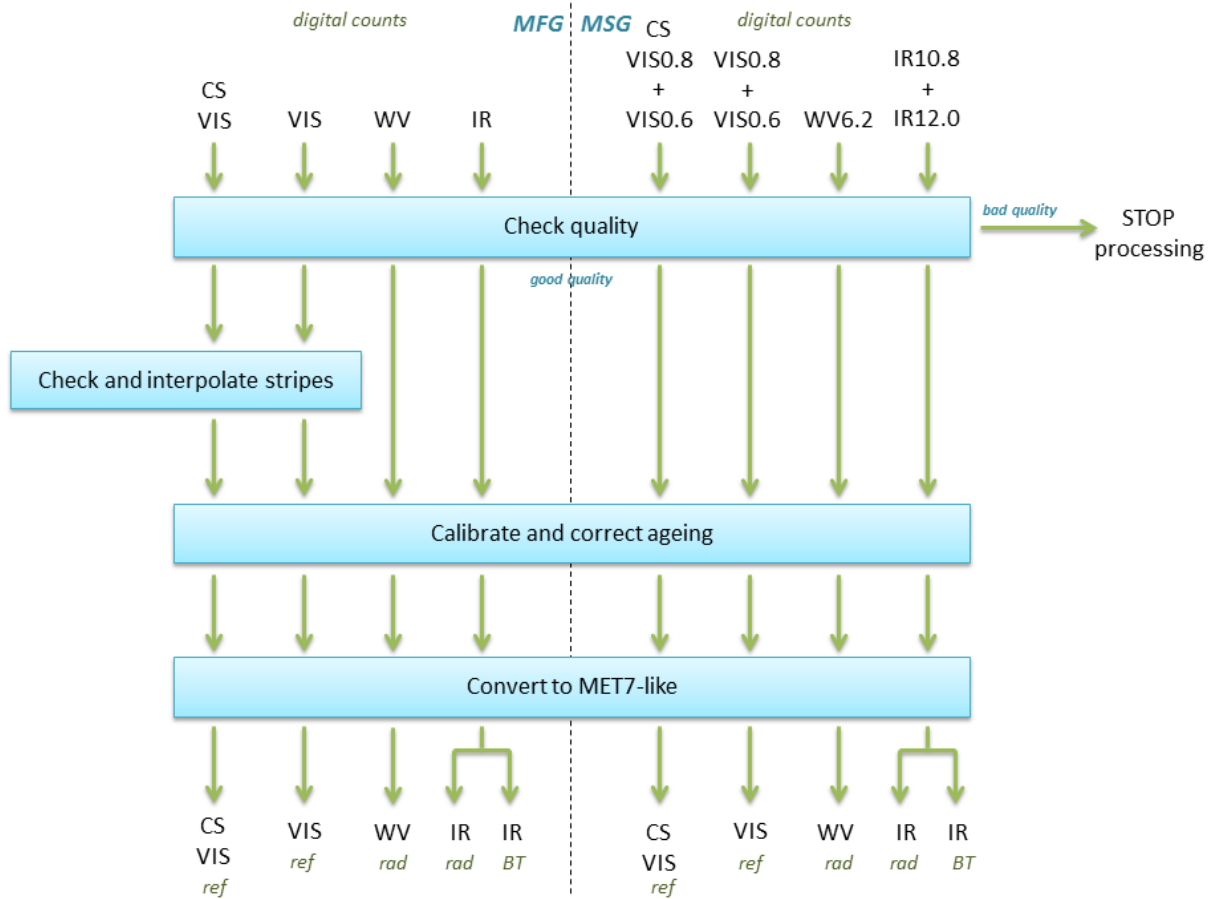
Figure 26: Overview flowchart for the data preprocessing algorithm (left part is for MFG data, right for MSG).

6.3 Algorithm description

6.3.1 Quality check

The first step of the algorithm aims at checking the quality of the input Level 1.5 data before their processing. It discards corrupted data and therefore avoids generating erroneous TOA fluxes. The analysis of the raw data extracted from the EUMETSAT Data Center was performed by the Deutscher Wetterdienst (DWD) in the frame of the Surface Solar Radiation DataSet - Heliosat (SARAH) development (see SARAH ATBD, doi: 10.5676/EUM_SAF_CM/SARAH/V001). This analysis covers the period 1983-1994. Different issues were identified within the input images such as a detector's failure, a wobble of the satellite FOV, a total corruption or stripes (MFG VIS images only). A detector's failure results in missing or broken lines in the image. It can only affect a small area while stripes are observed all over the image. Sometimes just some lines are missing, but it can also happen that a large part of the image is missing. On the other hand, stripes are only found in MVIRI VIS images usually before 1990 (MFG-2 and -3) due to the switch off of one of the two VIS detectors. A wobble of the satellite FOV leads to an incorrect location of the pixels across the Meteosat FOV. Finally, a total corruption of the data means unusable erroneous data over all or part of the image. It can be due to a problem during the downlink transfer or the on-board treatment of the raw data.

From these data reported as corrupted, data showing a detector's failure or stripes are not discarded from the processing since missing lines or parts of the image are not really problematic. All the other corrupted images are rejected.

6.3.2 Stripes check and interpolation

Even if missing lines are not really an issue for the processing, it was chosen to interpolate the stripes appearing in the MVIRI VIS images because of their very high occurrence mainly during the MET-2 and MET-3 operational phase. An extended switch off of one of the two MVIRI detectors operating in the VIS channel is responsible for those recurrent stripes. A short routine has been used to detect the presence of stripes within the MVIRI VIS image and their location over even or odd lines (depending on which detector is failing). When stripes are detected, the missing lines (even or odd) are interpolated from the two lines on either side. It should be noted that for a few cases double stripes of different default error values (0 or 255) are appearing within the images. Therefore, it is necessary to reset these images to a same single error value so that it could be accurately considered as empty by the processing. An example of the effect of this interpolation is shown in Figure 27.

Figure 27: Example of the effect of stripes interpolation. Earth disk's area for day 1985.12.01 at 12:00 (MFG-2) before (left) and after (right) interpolation.

6.3.3 MVIRI/SEVIRI calibration

An accurate calibration of the spectral channels is of prime importance for this work.

In this first edition of the data records, the SSCC calibration method (Govaerts et al., 2004) and the KNMI SEVIRI recalibration (Meirink et al., 2013) have been used for the VIS channels of the MVIRI and SEVIRI instruments, respectively. The use of a spectrally

dependent ageing model as in (Decoster et al., 2013a, 2013b, 2014a) has been considered but is not adopted for this work for 2 reasons. First, the effect on the all sky TOA TRS flux is limited (the main improvement concerns the clear sky TRS over clear ocean). Second, revisit of the Meteosat spectral responses and their temporal variations is currently investigated in the HOR2020 FIDUCEO project.

For the IR and WV channels of MVIRI, the EUMETSAT/GSICS recalibration of MVIRI using HIRS has been applied (R. Stöckli and A. Tetzlaff, pers. comm.). However, since the recalibration coefficients were not yet available for MET-2 and -3, the operational calibration has been used meanwhile in spite of significant stability issues. Information about the operational calibration is provided on the EUMETSAT webpage. Operational calibration coefficients are valid from the indicated time slot onwards, until the next calibration is provided. The EUMETSAT/GSICS recalibration of MET-2 and -3 is expected to be available by the end of 2016 and may be used in a later version of this data record. This would most probably solve the stability issues observed within the operational calibration of the WV and IR channels provided by EUMETSAT.

For the IR and WV channels of SEVIRI, the operational calibration available in the prologue of the L1.5 Meteosat images is used. As it can be seen in Table 11 for "ambient calibrations" at 95 K, the radiometric noise on each pixel is the highest for the 13.4 μm SEVIRI channel which is not used in the data record. The GSICS recalibration of SEVIRI using the IASI could be used in a later stage but currently this work does not cover the full MSG era.

Table 11: Level 1.0 radiometric noise for "ambient calibrations" at 95 K for the 3 SEVIRI instruments (cold channels) (from EUMETSAT (2012)).

Channel IR	3.9	6.2	7.3	8.7	9.7	10.8	12.0	13.4
MSG-1 Noise [K]	0.013	0.045	0.065	0.07	0.115	0.065	0.12	0.185
MSG-2 Noise [K]	0.09	0.05	0.05	0.075	0.10	0.07	0.10	0.205
MSG-3 Noise [K]	0.09	0.04	0.05	0.06	0.09	0.065	0.135	0.25

6.3.4 Spectral correction to MET7-like

Once the input data are calibrated, a spectral correction is applied on the radiances measured by the different MFG and MSG instruments to convert them into equivalent Meteosat-7 radiances (MET7-like). This step of the data preprocessing aims at limiting the discontinuities between the Meteosat instruments to get a homogeneous time series. As shown in Table 12, different methods are used for this conversion depending on the satellite and channel.

Table 12 : Method used for the spectral correction to MET7-like according to the satellite and channel.

Satellites	Visible	Thermal
Meteosat-2	Theoretical regressions dependent on the scene type and geometry	Theoretical regressions independent of the scene type and geometry
Meteosat-3		
Meteosat-4		
Meteosat-5	No conversion	
Meteosat-6		
Meteosat-8	Empirical regressions dependent on the scene type and geometry	
Meteosat-9		
Meteosat-10		

For the VIS channel of Meteosat-2 to -4, the MET7-like radiances have been computed using theoretical regressions dependent on the scene type and geometry. The 12 investigated scene types consist of the 6 surface types previously defined in Table 10 either cloudy or clear. A large database of simulated spectral radiances built using the Version 2.4 of the plane-parallel Santa Barbara DISORT Atmospheric Radiative Transfer model (SBDART, Ricchiazzi et al., 1998) has been indirectly used to tune those regressions. This database was generated to capture as much as possible the variability of the spectral signature of the scenes. It is made of simulations for 750 realistic conditions of the Earth surface, the atmosphere and the cloudiness. The Discrete Ordinate Radiative Transfer (DISORT) computations are performed using 20 streams to obtain an accurate representation of the dependency of the scene spectral signature with the Sun-target-satellite geometry. For each of the 750 simulations, the TOA radiances are computed for SZA varying between 0 and 80° in steps of 10°, VZA varying between 0 and 85° in steps of 5° and RAA varying between 0 and 180° in steps of 10°. A full description is provided in Clerbaux et al. (2008a). These simulations have then been convolved with the spectral response filters of the VIS channels of each Meteosat instrument to obtain their VIS filtered radiances. Thus it is actually these simulated VIS filtered radiances that have been used to tune the theoretical regressions between the Meteosat instruments and Meteosat-7. Therefore, the MET7-like VIS radiances (L_{MET7}) can be inferred from the VIS radiances measured by one of the Meteosat instrument (L_{METx}) using the following theoretical second order regression depending on the scene type and geometry:

$$L_{MET7} = a + b.L_{METx} + c.(L_{METx})^2$$

Since the parameters a, b and c are dependent on the scene type, i.e. the surface type and the cloud cover (clear or cloudy), a limited scene identification is first required to compute the MET7-like VIS radiances. The surface type is simply provided by the reduced IGBP surface type map described in section 4.4.1 while the cloud cover is inferred from the computation of the cloud coverage index C using the following equation:

$$C = \frac{\rho_{VIS} - \rho_{CS\,VIS}}{\rho_{OV\,VIS} - \rho_{CS\,VIS}}$$

where ρ_{VIS} is the measured reflectance, $\rho_{CS\ VIS}$ is the reflectance under clear-sky conditions (previously computed in section 5) *and* $\rho_{OV\ VIS}$ is the reflectance under overcast conditions. The latter is derived from a set of 5 models (corresponding to the 6 surface types defined in Table 10 except snow) as a generalised angular function (VZA, SZA, RAA). These models are computed using an overcast thick cloud layer that is assumed to be in the liquid phase in a first approximation. The cloud phase will be determined more accurately in section 7.3.1 by using the IR brightness temperatures. The regression coefficients a, b and c corresponding to the scene are finally interpolated according to the geometry. The regression can be chosen of the first (c=0) or second order (c≠0) in the configuration file. By default, the first order is selected as no significant improvement is gained by taking the second order, as shown by the RMS error values in Table 13 (for the regression between MET-2 and MET-7 and for an illustrative geometry : VZA of 40°, SZA of 40° and RAA of 90°). Taking the first order also avoid any divergence of the fitting curve at extreme radiances where few data are found (see Figure 28 for the regression between MET-2 and MET-7 over a cloudy and snowy surface).

Table 14 shows the coefficients and the RMS values obtained by regrouping the clear and cloudy scenes while Table 15 shows the results for all scenes combined. Looking at the RMS errors from the last 3 tables, it can be seen that the MET7-like radiances are much better simulated when separating the scenes according to their cloud cover and surface type. Similar conclusions are obtained for the regressions between MET-3 or MET-4 and MET-7.
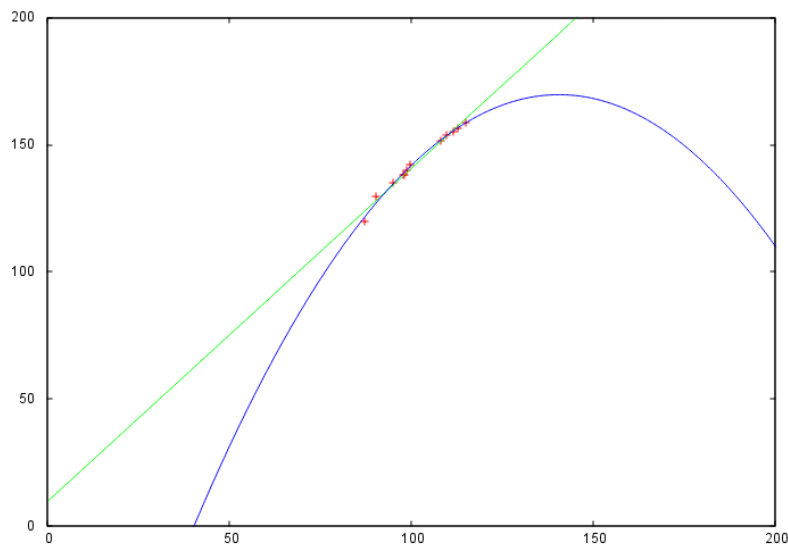
Figure 28: Regression of first (green line) and second order (blue curve) between MET-2 (x axis) and MET-7 (y axis) radiances in W.m^{-2}.sr^{-1} for a cloudy and snowy surface superimposed on data (red crosses).

Table 13: Coefficients and RMS values of the regression between the VIS channels of MET-2 and MET-7 for varying cloud cover, surface type and regression order. Geometry is taken at VZA of 40°, SZA of 40° and RAA of 90°.

Cloud cover	Surface type	Regression order	a	b	c	RMS (W.m^{-2}. sr^{-1} (%))
Clear	**Ocean**	**1st**	2.05214	1.47866		0.289708 (3.1%)
		2nd	2.20284	1.42508	0.00365947	0.289404 (3.1%)
	Dark vegetation	**1st**	-3.32415	1.3689		1.22057 (2.8%)
		2nd	4.38013	0.958282	0.00504438	0.983567 (2.2%)
	Bright vegetation	**1st**	- 0.530511	1.29589		1.28028 (3.3%)
		2nd	4.74893	0.966766	0.00470315	1.02475 (2.6%)
	Dark desert	**1st**	-0.616917	1.34282		1.81953 (4.0%)
		2nd	3.19705	1.12823	0.00246374	1.61791 (3.6%)
	Bright desert	**1st**	0.913169	1.32761		1.77351 (3.2%)
		2nd	4.22484	1.14764	0.00198122	1.59683 (2.9%)
	Snow	**1st**	-7.11203	1.49538		0.945136 (0.7%)
		2nd	-46.9748	2.52545	-0.00640256	0.675353 (0.5%)
Cloudy	**Ocean**	**1st**	2.37749	1.36631		0.590476 (0.6%)
		2nd	2.88861	1.34064	0.000210751	0.558931 (0.6%)
	Dark vegetation	**1st**	-4.14131	1.42846		0.827285 (0.8%)
		2nd	-4.51858	1.44173	-9.41755e^{-05}	0.831608 (0.8%)
	Bright vegetation	**1st**	-2.91378	1.41727		0.977783 (1.0%)
		2nd	-2.60002	1.40587	8.26766e^{-05}	0.98001 (1.0%)
	Dark desert	**1st**	-1.769	1.40625		1.0122 (1.0%)
		2nd	-1.53029	1.39795	5.92113e^{-05}	1.01504 (1.0%)
	Bright desert	**1st**	-1.51854	1.40314		1.10708 (1.0%)
		2nd	-1.29517	1.39602	4.85601e^{-05}	1.11415 (1.0%)
	Snow	**1st**	9.71371	1.31		1.63243 (1.1%)
		2nd	-163.601	4.7431	-0.0168751	1.12989 (0.79%)

Table 14: Coefficients and RMS values of the regression between the VIS channels MET-2 and MET-7 for varying surface type and regression order, by combining cloudy and clear scenes. Geometry is taken at VZA of 40°, SZA of 40° and RAA of 90°.

Surface type	Regression order	a	b	c	RMS (W.m^{-2}. sr^{-1} (%))
Ocean	1st	2.55934	1.36439		0.508267 (1.0%)
	2nd	2.65595	1.35171	0.000122771	0.497764 (0.9%)
Dark vegetation	1st	-5.38002	1.4395		1.22649 (1.6%)
	2nd	-3.95007	1.38284	0.000424928	1.20523 (1.6%)
Bright vegetation	1st	-4.10584	1.42695		1.51677 (2.2%)
	2nd	-1.73419	1.3255	0.000790694	1.43099 (2.1%)
Dark desert	1st	-2.3908	1.40837		1.71359 (2.3%)
	2nd	-0.0280122	1.30636	0.000810262	1.6054 (2.2%)
Bright desert	1st	-1.35686	1.39528		1.79367 (2.2%)
	2nd	2.10802	1.25637	0.00107498	1.57726 (1.9%)
Snow	1st	2.48634	1.38603		1.67244 (1.2%)
	2nd	-42.3979	2.3899	-0.00551301	1.10971 (0.8%)

Table 15: Coefficients and RMS values of the regression between the VIS channels of MET-2 and MET-7 for the 1st and 2nd order and for all scenes combined. Geometry is taken at VZA of 40°, SZA of 40° and RAA of 90°.

Surface type	Regression order	a	b	c	RMS (W.m^{-2}. sr^{-1} (%))
ALL	1st	-0.839468	1.39005		2.34287 (3.3%)
	2nd	2.20853	1.22003	0.00146684	1.83789 (2.6%)

For Meteosat-5 and -6, no spectral correction is needed since their spectral responses are identical to the one of Meteosat-7.

For Meteosat-8 to -10, the MET7-like VIS radiances have been computed using empirical regressions dependent on the scene type and geometry. More specifically, these empirical regressions were derived from simultaneous and collocated observations of Meteosat-7 (MVIRI) and Meteosat-8 (SEVIRI). Two narrow VIS channels (VIS 0.6 and VIS 0.8) are used to simulate the MET7-like radiances. The MET7-like VIS radiances (L_{Met-7}) are then inferred

from the VIS 0.6 and VIS 0.8 radiances measured by one of the METx instrument (L_{METX}) using the following theoretical first (with $d=e=f=0$) or second order regression depending on the scene type and geometry:

$$L_{VIS}^{MET7} = a + b.L_{VIS0.6}^{METx} + c.L_{VIS0.8}^{METx} + d.\left(L_{VIS0.6}^{METx}\right)^2 + e.\left(L_{VIS0.8}^{METx}\right)^2 + f.L_{VIS0.6}^{METx}.L_{VIS0.8}^{METx}$$

By default, the first order is selected as no significant improvement is gained by taking the second order. As for Meteosat-2 to -4, the regression coefficients are derived according to the scene type (surface type and the cloud cover) using a same scene identification.

For the thermal channels, the MET7-like radiances are inferred from the measured radiances using a theoretical regression that no longer depends on the scene type and geometry. Actually the thermal emission of the Earth depends on the VZA but this dependence is quite low. This can be seen for example in Table 16 by the slight dependence on the VZA of the regression coefficients between MET-2 and MET-7 for the IR channel (the same is observed for WV). The corresponding coefficients and RMS values for a regression independent of the geometry are given in Table 17. Furthermore, since no night time scene identification is foreseen, those regressions can no longer depend on the scene type. For the MVIRI instruments, the MET7-like IR or WV radiances are simply inferred from the radiances measured in the corresponding channel of the instrument. For the SEVIRI instruments, the MET7-like IR radiances are inferred from both the IR10.8 and IR12.0 narrowband channels while for the WV radiances, only the WV6.2 channel is used. This choice is based on the fact that these channels optimally cover the Meteosat-7 broadband thermal channels, as shown in Figure 29 and Figure 30 for Meteosat-8. In conclusion, for MVIRI, the theoretical regression used to infer the MET7-like thermal radiances has the same form as the one used for the VIS channel:

$$L_{MET7} = a + b.L_{METx} + c.(L_{METx})^2$$

For SEVIRI, the MET7-like WV radiances (L_{MET7}) are inferred from the WV6.2 radiances measured by the METx instrument (L_{METx}) using the same following first (c =0) or second order regression

$$L_{WV}^{MET7} = a + b.L_{WV6.2}^{METx} + c.\left(L_{WV6.2}^{METx}\right)^2$$

On the other hand, the MET7-like IR radiances are inferred from the METx measured IR radiances using the following first (d=0, e=0 and f=0) or second order regression

$$L_{IR}^{MET7} = a + b.L_{IR10.8}^{METx} + c.L_{IR12.0}^{METx} + d.\left(L_{IR10.8}^{METx}\right)^2 + e.\left(L_{IR12.0}^{METx}\right)^2 + f.L_{IR10.8}^{METx}.L_{IR12.0}^{METx}$$

The order of those regressions can be chosen in the configuration file. By default, the second order is taken since a significant improvement is gained against the first order, contrary to the VIS case, as it can be seen by looking at the RMS values in Tables 16 and 17 for the IR channel (the same is observed for WV).

Table 16: Coefficients and RMS values of the regression between the IR channels of MET-2 and MET-7 for varying VZA value and regression order.

VZA	Regression order	a	b	c	RMS (W.m^{-2}. sr^{-1} (%))
0	1st	0.125117	1.24708		0.0351409 (0.4%)
	2nd	0.0183499	1.27947	-0.00199591	0.0214767 (0.2%)
20	1st	0.125158	1.24687		0.0350353 (0.4%)
	2nd	0.0185537	1.27946	-0.00202304	0.0214613 (0.2%)
40	1st	0.124986	1.24619		0.0344738 (0.4%)
	2nd	0.0192961	1.27934	-0.00211089	0.0212004 (0.2%)
60	1st	0.123534	1.24485		0.0324652 (0.3%)
	2nd	0.0211939	1.27883	-0.0022906	0.0198576 (0.2%)
80	1st	0.116853	1.24158		0.0271658 (0.3%)
	2nd	0.0252889	1.27701	-0.0027975	0.0176041 (0.2%)

Table 17: Coefficients and RMS values of the regression between the IR channels of MET-2 and MET-7 for the 1st and 2nd order, all VZA combined.

Regression order	a	b	c	RMS (W.m^{-2}. sr^{-1} (%))
1st	0.116669	1.24629		0.037328 (0.4%)
2nd	0.0356695	1.27224	-0.00169183	0.0306004 (0.3%)
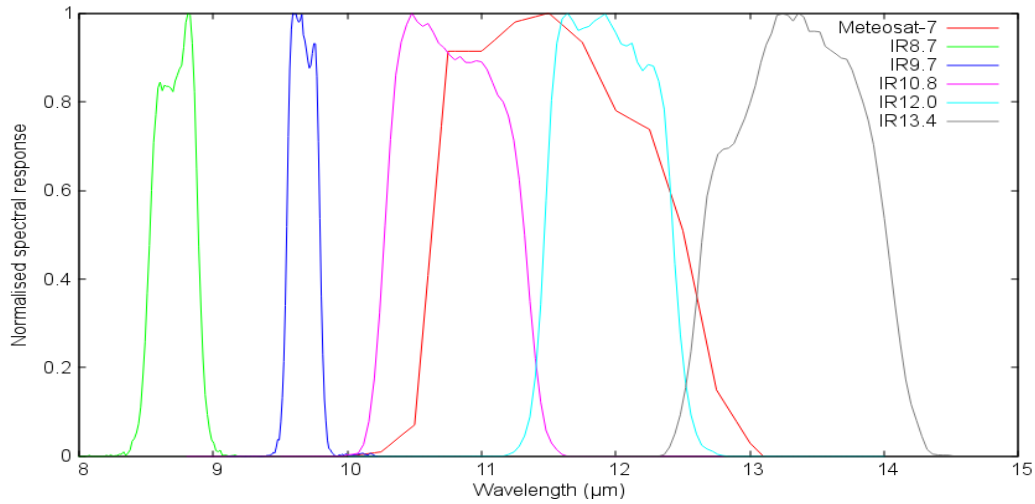
Figure 29: Curves of the spectral responses of the infrared channels of MET-8 and MET-7 (red curve).
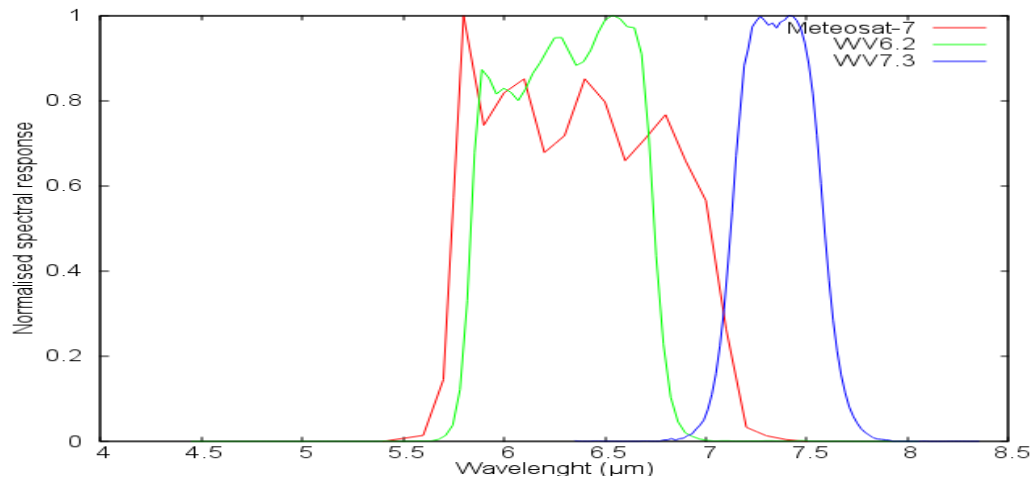
Figure 30: Curves of the spectral responses of the water vapour channels of MET-8 and MET-7 (red curve).

6.3.5 Radiance to reflectance/brightness temperature

For the VIS channel, the outputs of the preprocessing subsystem are given in reflectance. The measured MET7-like VIS radiances L (in $W.m^{-2}.sr^{-1}$) are converted into reflectance ρ (dimensionless) using the equation:

$$\rho = \frac{L.\pi.d^2}{FSI.\cos(SZA)}$$

where *FSI* is the filtered solar irradiance for the VIS channel of Meteosat-7 (690.8 W.m^{-2}) and *d* is the Sun-Earth distance in AU at the acquisition time of the image.

For the IR and the WV channels, the outputs of the preprocessing subsystem are given in radiances. In addition, the brightness temperatures of the IR channel are estimated as they are needed later in the processing. The IR brightness temperatures T_B, expressed in Kelvin, are estimated from the MET7-like IR NB radiances *L* using the logarithmic fit

$$T_B = \frac{-B}{A - \log(L)}$$

The coefficients *A*=6.9618 and *B*=-1255.5465 K for Meteosat-7 are taken from the EUMETSAT calibration webpage.

6.4 Algorithm validation

6.4.1 Stripes interpolation

In order to evaluate the impact on the TOA fluxes of the stripes interpolation process applied on the MVIRI VIS images, stripes were simulated over initially complete images and the fluxes before and after the simulation were compared. The stripes were simulated both over odd and even lines. Table 18 shows the bias introduced in the TOA fluxes by the stripes interpolation process for 1 June 2005 at 06:00, 12:00 and 18:00 UTC (Meteosat-7). It can be seen that the bias is very similar for stripes simulated over odd or even lines and always remains below 1 W.m^{-2}.

Table 18: Impact of the stripes interpolation process on the TOA fluxes in terms of bias for 1 June 2005 at 06:00, 12:00 and 18:00 UTC. Stripes were simulated both over even and odd lines of the Meteosat-7 images.

	Bias (W.m^{-2})	
	Even stripes	**Odd stripes**
06:00 UTC	-0.68	-0.69
12:00 UTC	-0.59	-0.57
18:00 UTC	-0.76	-0.77

6.5 Assumptions and limitations

- For the Met-2 to -6 satellites, the spectral response correction is based on the published spectral response curves. Those curves are known to be inaccurate, especially for the VIS channel.

- As the quality check of the input data from the EUMETSAT Data Center was only performed over the period 1983-1994 (included), corrupted data may have been introduced in the processing outside this period.

- For SEVIRI the operational calibration is used for the WV 6.2µm and IR 10.8µm and 12µm channels. Although some bias is reported for those channels when compared with other instrument (e.g. IASI within GSICS), the biases are quite constant and do not change significantly during decontamination of the instrument (such a change during decontamination is observed with the IR 13.4µm channel which is not used in this work).

6.6 Future enhancements

Future enhancements of the data-preprocessing would mainly consist in using Meteosat FCDR as input data, making the preprocessing not needed anymore. Those FCDRs are expected to be available in the +/- 2020 time frame.

7 Algorithm description (part 3/4): TOA fluxes processing

7.1 Purpose of the TOA fluxes processing

In this third part of the processing, the TRS and TET fluxes are estimated from the MET7-like data delivered by the preprocessing algorithm. This involves sucessively: (i) a scene identification, (ii) a conversion from narrowband (MET7-like) to unfiltered broadband radiances and (iii) the fluxes estimation from the radiances.

The output fluxes are expressed in $W.m^{-2}$ and are computed at the full spatial and temporal resolution of either the MFG or the MSG instruments, i.e., at $(2.5\ km)^2$ or $(5\ km)^2$ and every 30 minutes for MVIRI and at $(3\ km)^2$ and every 15 minutes for SEVIRI. Those fluxes are "instantaneous" fluxes, valid at the time of Meteosat acquisition.

7.2 Algorithm overview

Figure 31 shows the three main processing steps: the scene identification, the narrowband to broadband conversion and the TOA fluxes computation.
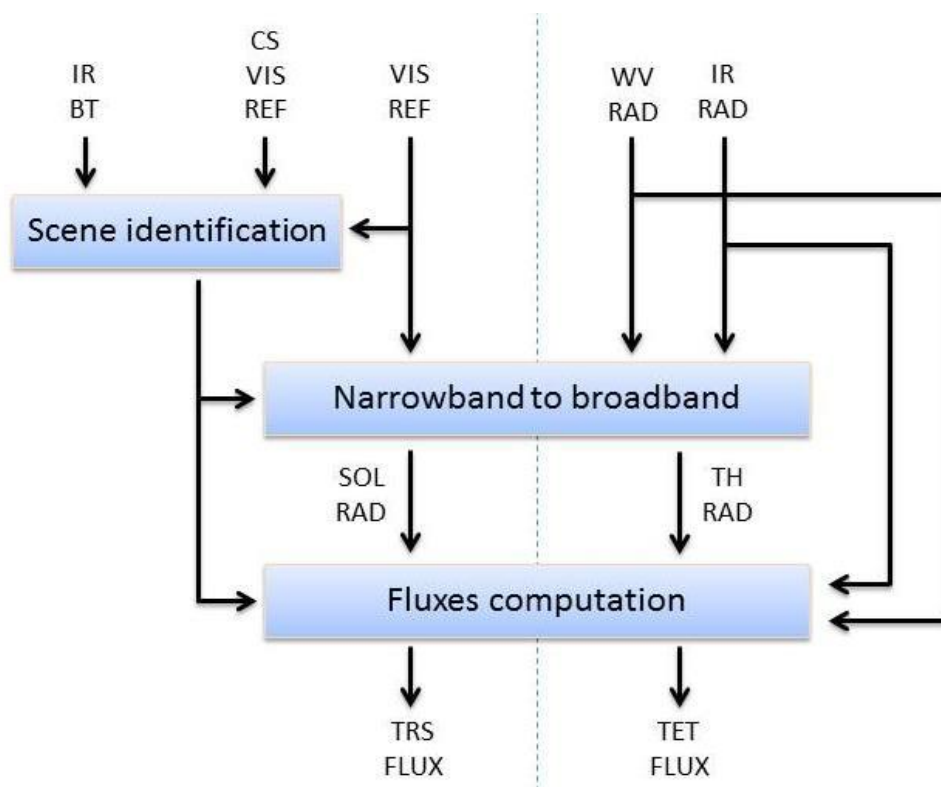
Figure 31: Overview flowchart for the TOA fluxes processing algorithm.

The scene identification is performed during daytime (SZA < 80°) based on the VIS and CS VIS reflectance in combination with the IR brightness temperatures. The algorithm allows identifying the cloud features of the scene which is needed information for the NB to BB conversion as well as for the SW ADM selection. Indeed the NB to BB algorithm computes the unfiltered solar radiation from the VIS reflectances using empirical regressions that are dependent on the scene. On the opposite, the unfiltered thermal radiation computation is based on the WV and IR radiances without relying on any information about the scene. The final step of the processing uses the unfiltered broadband radiances to compute the TOA fluxes. For the SW fluxes, this is done by again using the scene identification information while for the LW fluxes it requires the filtered IR and WV radiances besides the unfiltered thermal radiation.

In the solar region the conversion in flux is carried out using the CERES TRMM SW ADMs (see section 4.4.3). Since these ADMs are stratified according to specific scene properties, the SW fluxes computation has to rely on a scene identification to select the best suited ADM. On the other hand, theoretical models independent of the scene are used for the LW fluxes computation and therefore no scene identification is required.

The SW processing takes as input the VIS and CS VIS reflectances as well as the IR brightness temperatures (used for scene identification) while the LW processing only takes as input the WV and IR radiances coming from the data preprocessing. The algorithm design only allows delivering one of the two components if some input data are missing.

7.3   Algorithm description

7.3.1 Scene identification

The scene identification is a preliminary step necessary for the processing, in particular for the selection of the best suited ADM for the SW fluxes computation. It is also used to derive the regressions between the narrowband (MET7-like) and broadband radiances. The scene identification is performed only during daytime (SZA < 80°) and for VZA < 80°. It requires the VIS, the CS VIS, the brightness temperature (BT) in the IR channel and the full resolution surface type (ST) images as input. The method is based on the commonly accepted assumptions that the clear-sky variations in reflectance are smaller in time than in space and that the reflectance variations induced by the surface are smaller than variations induced by clouds. In particular, it is mainly based on the scene identification implemented and validated by Ipe (2011) and Ipe et al. (2010, 2004). It should be noted that this scene identification process is highly unreliable over snow covered regions as they exhibit VIS reflectances similar to the ones of clouds.

Following Ipe (2011), the scene identification process involves the computation of four parameters for each pixel (see the flow diagram in Figure 32). These cloud properties are retrieved at the full resolution (2.5 km for MVIRI and 3 km for SEVIRI) and are then averaged over a 3x3 pixels' footprint to maintain consistency with the CERES TRMM SW ADMs (10 km resolution at nadir). Those four parameters are:

- The cloud thermodynamic phase,

- The cloud optical depth (COD),

- A scene flag indicating if the scene is either clear, cloudy, uncontrasted, shadowed or undefined,

- The cloud fraction.

The scene identification process is actually divided in two parts, the first part dealing with the processing of each pixel across the 3x3 pixels' box and the second with the averaging over the box. In particular, this averaging is performed over the cloudy part of the box. The cloud fraction is defined as the number of cloudy pixels divided by the total number of valid pixels (clear, cloudy and shadowed) provided that the number of clear and cloudy pixels represents the majority. Details about the scene identification scheme are given in the remainder of this section.
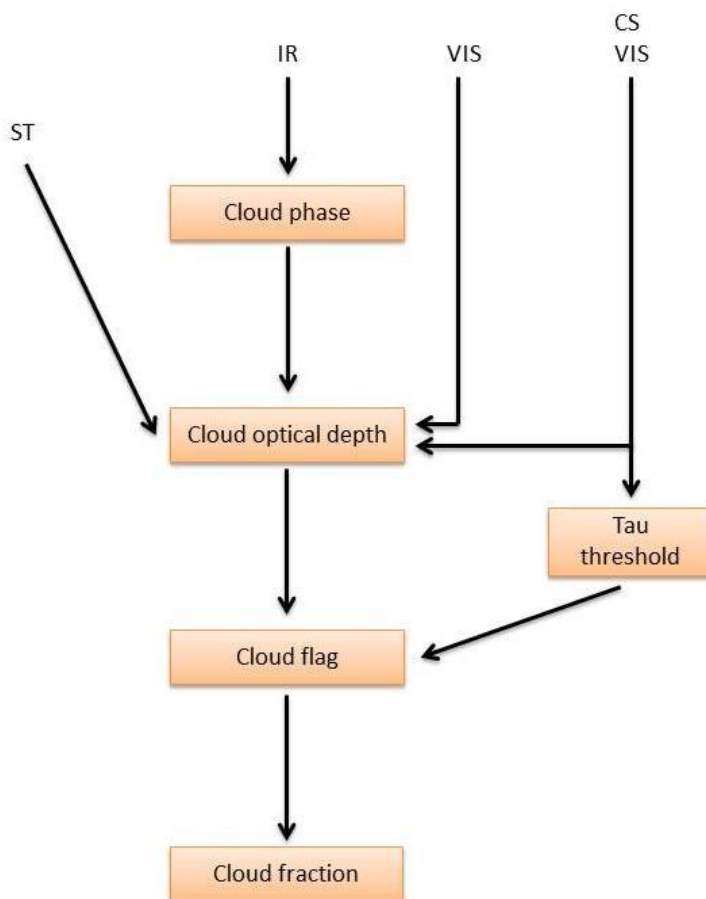
Figure 32: Flow diagram of the scene identification scheme.

The first step of the scene identification is the computation of the cloud thermodynamic phase for each pixel across the box. An index is used to discriminate between water and ice cloud pixels from the MET7-like brightness temperatures (BT) in the IR channel and two empirical threshold values (BT_{max}=265K and BT_{min}=245K from Ipe (2011))

$$Index = \begin{cases} 0 & \text{if } BT > BT_{max} \\ \dfrac{BT_{max} - BT}{BT_{max} - BT_{min}} & \text{if } BT_{min} \leq BT \leq BT_{max} \\ 1 & \text{if } BT < BT_{min} \end{cases}$$

Since the ADMs only exist for water or ice cloud phases, the pixel is assigned to pure ice when the index is above 0.5 and to pure water otherwise.

The COD is estimated using a set of Look-Up-Tables (LUTs) of VIS NB radiances retrieved from a radiative transfer model (RTM) for a restricted number of ideal scenes with varying COD and the comparison with the associated CS VIS reflectances. The RTM used in this scheme is the plane-parallel STREAMER RTM (Key and Schweiger, 1998). Following Ipe et al. (2004), the COD is not directly retrieved from the measured VIS NB radiance using the LUTs. First, the mean cloud amount (or cloud coverage index) C is calculated using the following equation:

$$C = \frac{\rho_{VIS} - \rho_{CSVIS}}{\rho_{OVVIS} - \rho_{CSVIS}}$$

where ρ_{VIS} is the measured reflectance, $\rho_{OV\ VIS}$ is the reflectance under optically opaque cloudy (i.e. overcast) conditions and $\rho_{CS\ VIS}$ is the reflectance under clear-sky conditions. By definition, the overcast situation corresponds to a cloud thickness of $\tau = 128$ (consistent with the CERES scene identification) (Minnis et al., 2011) and the CS situation to $\tau = 0$. The overcast reflectance is derived from a set of ten models as a generalised angular function (VZA, SZA, RAA). Those models have been derived for the 6 surface types defined before (see Table 10) except snow and for 2 cloud phases (ice or water) using an overcast cloud layer. The clear-sky reflectance is coming from the visible clear-sky processing. The C value is computed only if the denominator is above a threshold of 0.2, otherwise the pixel is flagged as **uncontrasted**. Furthermore, if the value of C is below a threshold of -0.1, the pixel is flagged as **shadowed** and the COD is not computed. The empirical law of the reflectance relative to the COD is rescaled with C values ranging from 0 to 1. The COD (τ) is finally retrieved from the mean cloud amount by inversing a sigmoidal fit

$$\tau = \begin{cases} \dfrac{\tau_0 C^x}{(A - BC)^x} & \text{for } C < \dfrac{A}{B} \\ 128 & \text{for } C \geq \dfrac{A}{B} \end{cases}$$

with $x \neq 0$, $\tau_0 > 0$. The parameters A, B, τ_0 and x, which depend on the geometry, the cloud phase and the surface type, are obtained through a least square fit on the theoretical simulations values by using the Powell multidimensional fitting approach (Press et al.,1992).

The cloud flag is based on a threshold test on the COD. For each pixel inside the 3x3 pixels' box, this threshold is dynamically determined from the composite CS reflectance (ρ_{CS}) using the following equation

$$\tau_{thres} = MIN\left[\tau_{max}, \alpha + \beta\left(\rho_{CS}^{max} - \rho_{CS}^{min}\right)\right]$$

The notations *min* and *max* denotes a minimum or maximum value searched in a 3x3 pixels' box around the pixel of interest. It is found that parameters values of 3.0 for τ_{max}, 0.6 for α and 30.0 for β give good results in heterogeneous Earth surface boundary regions (Ipe, 2011). The pixel is classified as **clear-sky** if the COD is under this threshold and **cloudy**

otherwise. In practice the threshold is increased in regions of strong contrast like the coastlines.

Once the cloud properties are computed for each pixel, these are "averaged" over the 3x3 pixel's box and the mean value is allocated at the central pixel. The pixel is flagged as undefined if no valid pixel (clear, cloudy or shadowed) is found inside the box and if the number of undefined pixels is higher than the number of uncontrasted pixels. It is flagged as uncontrasted in the other case. If at least one pixel is valid and if the majority of them is shadowed, the central pixel is considered as shadowed. Otherwise, it is flagged as clear if no pixels are cloudy, and cloudy alternatively. For cloudy pixels, the cloud phase and COD (actually its logarithm) are computed by simply taking the average over the cloudy part of the 3x3 pixel's box while the cloud fraction is computed as the number of cloudy pixels divided by the number of valid pixels provided that the number of clear and cloudy pixels represents the majority. For clear pixels, the cloud fraction is set to zero.

In the sun glint region and in the terminator, the scene identification could be temporally interpolated/extrapolated using a method developed by the GERB team (E. Baudrez, personal communication). Basically, the methodology consists in replacing the scene identification of every pixel affected by the sun glint or located in the terminator by the timely closest unaffected one.

7.3.2 Narrowband to broadband conversion

To derive the TOA fluxes, it is first necessary to "unfilter" the MET7-like radiances in order to get spectrally integrated energies. The unfiltered broadband (BB) radiances are estimated from the filtered narrowband (NB) measurements using spectral modeling techniques. Empirical and theoretical approaches are possible. The first one relies on collocated co-angular NB and BB observations while the second one is based on radiative transfer computations to simulate a database of spectra. Different NB-to-BB regressions have been derived and used to generate unfiltered data, in particular within the GERB and CM SAF processing systems. For the LW radiation, Dewitte and Clerbaux (1999) provided theoretical regressions to generate the unfiltered data from Meteosat-7. Third order regressions have also been developed to generate the SW unfiltered data from simulated Meteosat-7 VIS data (details on the method can be found in Bertrand et al. (2003)).

For this data record, empirical regressions were preferred to their theoretical counterparts. The main disadvantages of the theoretical approach are the quite high biases introduced in the estimation of the BB radiances, especially where the scene presents 3-dimensional effects that are difficult to model, and in addition for the SW radiation, the absence of stratification according to the surface type. Theoretical regressions are actually mainly being used to improve and/or fill gaps in empirical models.

This section summarizes the main steps of the adopted empirical "unfiltering" method, yet the whole methodology is presented in details in Clerbaux (2008) and Clerbaux et al. (2007).

The "unfiltering" process takes advantage of the overlap period between MVIRI on MET-7 and GERB on MET-8 (located at a 0° and -3.5° longitude respectively), from 1 February 2004

up to 14 June 2006. The co-angular validated unfiltered radiances from the GERB-2 BARG products of the GERB Edition 1 data record[4] have been used. The BARG format was preferred to the ARG due to its easier comparison with other instruments and to avoid the scene dependency affecting the ARG which results from the non compensation of the PSF (J. Russell and L. Gonzalez, pers. comm.). Due to the difference in longitude between both instruments, the BARG radiances have been first corrected to infer the radiances that would have been measured by the instrument at 0° longitude.

For the SW case, a database of co-angular MET-7 VIS radiances and corresponding GERB SW unfiltered radiances has been built. The MVIRI data are downscaled from the 2.5 km spatial resolution of the MVIRI VIS channel to the lower 45 km resolution of the BARG GERB pixel by box averaging. A maximum time difference of 450 seconds is allowed so that each MET-7 radiance can be associated with a BARG pixel radiance. Furthermore, only observations with SZA<80° and VZA<80° are taken into account. The database has been sorted according to the GERB surface type (the 6 classes from Table 10), the SZA and VZA (in 20° bins), the RAA (in 45° bins) and the type of cloud cover (clear-sky, broken cloud, thin cloud water, thin cloud ice, thick cloud water, thick cloud ice). This stratification defines 2304 bins. For each of these bins, the best linear fit between the filtered NB reflectances of MET-7 (ρ_{VIS}) and the unfiltered BB reflectances of GERB (ρ_{BB}) is computed using the least mean square technique:

$$\rho_{BB} = a + b\,\rho_{VIS}$$

Clerbaux et al. (2007) showed that empirical regressions to generate unfiltered data from the MVIRI VIS channel are adequate as long as they are defined for a sufficient number of surfaces and cloud types. Table 19 provides the biases and RMS errors of the ratio between the theoretical and empirical estimates and the GERB Edition 1 for different scene types and seasons over $(135\ \text{km})^2$ boxes (Clerbaux, 2008). Empirical regressions exhibit better results than theoretical regressions. The RMS error for the empirical approach is only about 1.4% for clear scenes and 0.8% for cloudy scenes. The overall bias in the empirical approach (-0.4%) is due to ageing of the instrument as different time periods are used to fit the regressions and to evaluate their performances.

---

[4] The GERB-2 BARG products are not currently available in the GERB Edition 1 dataset but will be soon.

Table 19: Biases (with respect to 1.0) and RMS errors of the ratio between the NB-to-BB theoretical and empirical estimates and the GERB Edition 1 evaluated in 135km×135km boxes (from Clerbaux, 2008). Only the boxes with VZA < 70° have been taken into account.

Scene Type	Theoretical		Empirical	
	Bias (%)	RMS (%)	Bias (%)	RMS (%)
Clear	-10.4	2.0	-0.4	1.4
Cloudy	-8.3	1.0	-0.4	0.8
Broken cloud	-7.9	1.4	-0.4	1.1
Thin water cloud	-7.8	1.4	-0.4	1.1
Thin ice cloud	-8.5	1.2	-0.3	0.9
Thick water cloud	-8.3	1.3	-0.4	1.0
Thick ice cloud	-8.6	1.0	-0.4	0.8
Winter	-9.7	1.9	-0.3	1.2
Spring	-9.6	1.7	-0.4	1.2
Summer	-9.3	2.1	-0.1	1.4
Autumn	-9.9	1.9	-0.8	1.2

For the LW case, a database of co-angular MET-7 WV and IR radiances and corresponding GERB LW unfiltered radiances has been built. It was decided to estimate the BB radiances (L_{BB}) from the NB WV and IR measurements (L_{WV} and L_{IR} resp.) using the following second order regression without crossed terms (Dewitte & Clerbaux, 1999)

$$L_{BB} = C_0 + C_1 L_{WV} + C_2 L_{IR} + C_3 L_{IR}^2$$

The coefficients C_i of the regression are dependent on the VZA. The empirical regressions were fitted using boxes of 12x12 BARG pixels (540x540 km^2) and on a seasonal basis (DJF, MAM, JJA, SON). This aims to account for the spatial and seasonal patterns of water vapour in the atmosphere and for local variation of the surface emissivity.

Clerbaux (2008) reports RMS error of about 0.4% for the empirical estimates at a regional scale of 135km, as shown in Table 20. The improvement relative to theoretical regressions is significant. It is also showed that, in general, better NB-to-BB results are observed over the ocean than over land surfaces. Most of the monthly mean residual errors seem to result from changes in desert surface emissivity (see Clerbaux (2011), pages 129-130 and Figure 5.15 (page 130)).

Table 20: Biases (with respect to 1.0) and RMS errors of the ratio between the NB-to-BB theoretical and empirical estimates and GERB in the 135km×135km boxes with VZA < 70° for the theoretical and empirical MET-7 NB-to-BB regressions (from Clerbaux, 2008).

Month	Theoretical		Empirical	
	Bias (%)	RMS (%)	Bias (%)	RMS (%)
200410	1.7	0.8	0.1	0.4
200501	1.4	0.8	0.1	0.3
200507	1.7	1.1	-0.1	0.3
200604	0.8	0.6	-0.1	0.4

7.3.3 Broadband radiances to fluxes conversion

The unfiltered BB radiances obtained through spectral integration are still directional measurements of radiation. To study the Earth radiation budget (ERB), the hemispheric fluxes need to be inferred from those directional values. Fluxes (*F*) and radiances (*L*) are linked by the following relation

$$F = \int_{VZA=0}^{\frac{\pi}{2}} \int_{RAA=0}^{2\pi} L(SZA, VZA, RAA) . \cos(VZA) . \sin(VZA) \, dVZA \, dRAA$$

In the ideal case of an isotropic (Lambertian) radiance field, the radiance to flux conversion is trivial and this equation reduces to *F= π.L*. However, this is not the case for real scenes and a characterization of the angular distribution of radiance, i.e. the anisotropy, is needed for the conversion from radiance to flux. The anisotropy factor *R* is defined as the ratio of the equivalent Lambertian flux (*π.L*) to the hemispheric flux *F*

$$R(SZA, VZA, RAA) = \frac{\pi . L(SZA, VZA, RAA)}{F}$$

This equation is widely used to infer the flux from the directional measurement after angular modelling of the anisotropy of the radiance field at the TOA. As for the NB-to-BB conversion, empirical and theoretical approaches are possible. The first one relies on anisotropy models derived from multi-angle BB instrument observations while the second one is based on radiative transfer computations to model the anisotropy of the radiance field. Because each scene has a particular anisotropy, the selection of the best suited model to infer the flux from the radiance requires a characterization of the observed scene. However, since the explicit scene identification is mainly based on the VIS channels, it is not available during the night. Therefore, the selection of the best suited model to infer the LW fluxes relies on an "implicit identification". Theoretical models are used for the LW fluxes retrieval while empirical models dependent on the scene identification are used for the SW fluxes retrieval.
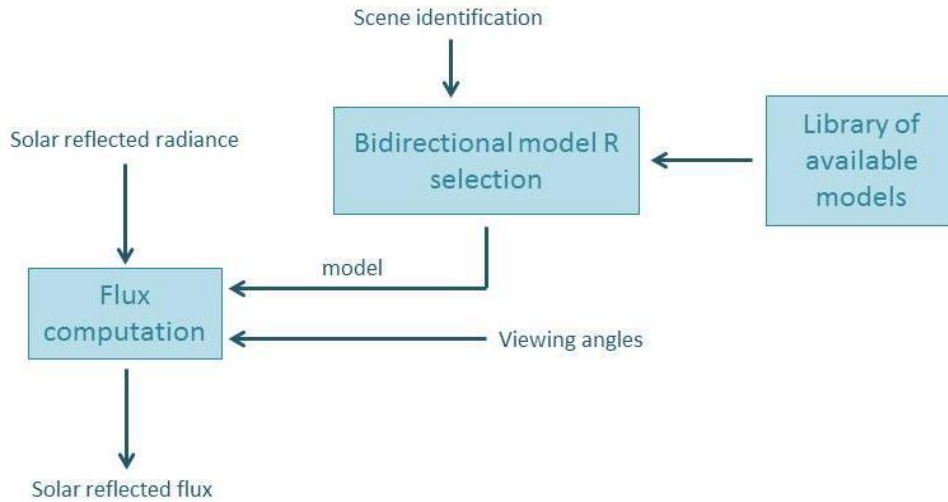
Figure 33: Overview flowchart for the SW BB radiance to flux conversion.

For the SW radiation, the CERES TRMM ADM models (Loeb et al., 2003) are used to infer the flux from the radiance. These models have been widely used to process geostationary observations, for instance from GERB, GOES, Meteosat or MTSAT by the CERES Time-Space Averaging (TISA) group. The selection of the best suited ADM requires a characterization of the observed scene which is provided by the cloud properties retrieval process (see section 7.3.1) and the use of a fixed surface type map (reduced IGBP surface type map developed in section 4.4.1). It should be noted that since the scene identification is used in the ADM selection, distinct spatial resolutions between MVIRI and those ADMs could lead to a systematic bias in the TOA fluxes estimation. Nevertheless, since the CERES scene identification is based on collocated VIRS measurements, this issue is mitigated by the fact that the VIRS and MVIRI imagers have similar spatial resolutions. Figure 33 provides an overview of the method that is used to infer the flux from the SW BB radiance. To select the best suited ADM, the surface type fractions are first extracted from the surface type map for each pixel. In case of mixed pixels, the anisotropic factor R is obtained using the adequate weighting (Bertrand et al., 2005; Suttles et al., 1988):

$$R(SZA, VZA, RAA) = \frac{\sum_i \omega_i . A_i(SZA) . R_i(SZA, VZA, RAA)}{\sum_i \omega_i . A_i(SZA)}$$

where ω_i is the fraction of the surface type i in the footprint and A_i and R_i are the corresponding TOA albedo and anisotropic factor. For each surface type, the best suited CERES TRMM ADM is selected depending on the scene identification (scene flag, cloud fraction, cloud phase, COD). Over clear ocean, separate ADMs are provided for four intervals of wind speed (v_k). In this case, the 6-hourly wind speed fields from the ECMWF ERA Interim Reanalysis (Simmons et al., 2007; Dee et al., 2011) are used in combination with the scene identification and the surface type map to select the best suited model. Interpolation is done between the available CERES TRMM ADMs angular bins. This is achieved using a simple trilinear interpolation on the R values over the scene geometry. There is no interpolation on the cloud fraction, the cloud phase and the COD. Following the CERES team advice, an ADM normalisation process is implemented. The normalisation factor accounts for a nonlinear variation of the radiance within an ADM's angular bin. This factor is added to the TOA fluxes to remove any bias from the trilinear interpolation process. A theoretical adjustment of the clear-sky ocean ADMs is also performed to account for the

reduction of anisotropy in presence of aerosols. The TOA fluxes are first inferred in any viewing geometry from wind speed-dependent empirical ADMs and are then adjusted as follows (Loeb et al., 2003):

$$F = \frac{\pi . L(SZA,VZA,RAA)}{R(v_k,SZA,VZA,RAA).\left[\frac{R^{th}(v_k,I)}{R^{th}(v_k,\bar{I})}\right]}$$

$R(v_k,SZA,VZA,RAA)$ is determined from wind speed-dependent empirical ADMs. $R^{th}(I)$ and $R^{th}(\bar{I})$ are theoretical radiative transfer model anisotropic factors evaluated at the measured and mean radiances, respectively $I(SZA,VZA,RAA)$ and $\bar{I}(SZA,VZA,RAA)$, in a given ADM angular bin. Basically, the aerosol correction is proportional to the difference between the observed BB radiance and the theoretical radiance of the ADM. Due to the limited observations over snow, no CERES TRMM ADM is provided for snow covered surfaces. Therefore, the bright desert ADMs are used for permanent snow/ice surfaces, since they are the closest models in terms of albedo. Besides the CERES TRMM ADMs, the following additional models are used:

- The **Lambertian model** used over shadowed regions and for SZA higher or equal to 90°. Shadowed pixels may appear for grazing SZA (dawn and dusk) at the borders of cloud formations (specifically near high level clouds). The shadow flag is generated by the cloud analysis within the scene identification process. In that particular case, the anisotropic factor is equal to 1 and the flux is isotropic.

- The **Sun Glint model** used in the sun glint region (SGA<25°) over clear ocean surfaces. The flux is estimated using the modelled ocean albedo A_{ocean} instead of the measured radiance as follows:

$$F(SZA) = A_{ocean}(SZA).\cos(SZA).E_0$$

  where E_0 is the solar constant (from the RMIB TSI composite, see Section 4.4.6) corrected for the Earth-Sun distance. Indeed, as the radiance increases strongly in the sun glint region due to specular reflection on the ocean surface, the retrieval of the flux from this radiance could lead to important errors.

- For **SZA>85**, no instantaneous fluxes are computed. A specific twilight model (Kato and Loeb, 2003) will be applied in the daily and monthly averaging process (see section 8).
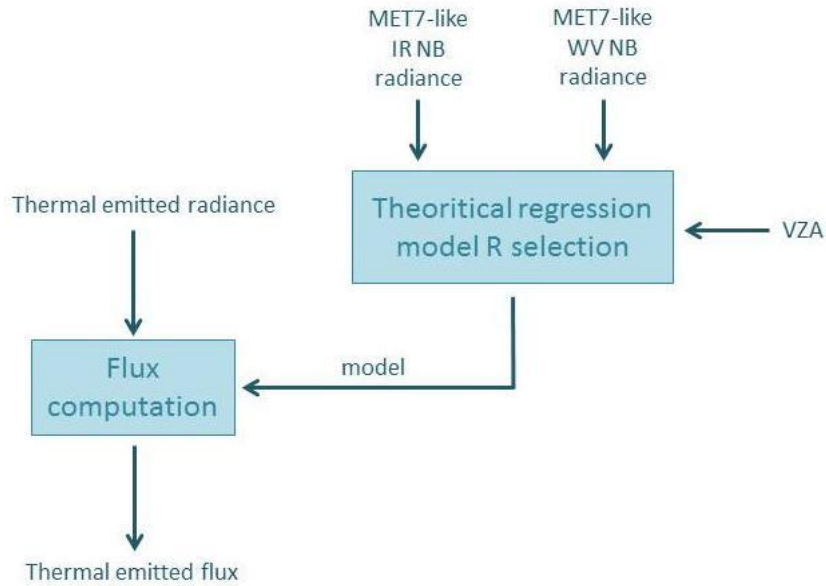
Figure 34: Overview flowchart for the LW BB radiance to flux conversion.

For the LW radiation, since no cloud retrieval is available with Meteosat during night time, theoretical regressions developed at RMIB are used instead (Clerbaux et al., 2003a, 2006; Clerbaux, 2008). These regression models are not selected by an explicit scene identification but through the analysis of the NB radiances of the imager ("implicit identification"). Figure 34 provides an overview of the method used to infer the flux from the LW BB radiance using the MET7-like NB IR and WV radiances. Since the thermal radiation field exhibits negligible dependency on the azimuth direction, the anisotropy factor is only modelled according to the VZA. The anisotropy factor mainly represents the limb darkening function of the scene which mostly depends on the atmospheric state and cloudiness (the surface emission is considered isotropic as a first approximation). Thermal radiation fields are generated using the SBDART (Ricchiazzi et al., 1998) model. For a set of 4632 different Earth/Atmosphere conditions, the radiation field and the corresponding thermal flux are simulated at VZA varying between 0 and 85° in steps of 5°. The Earth-Atmosphere system can be characterised by surface parameters, atmospheric profiles, trace gases concentrations and cloud conditions. The anisotropic factor R is fitted using a second order regression on the MET7-like WV and IR NB radiances (L_{IR} and L_{WV} respectively):

$$R = c_0 + c_1 L_{WV} + c_2 L_{IR} + c_3 L_{IR} L_{WV} + c_4 L_{WV}^2 + c_5 L_{IR}^2$$

The flux F is then obtained from the thermal BB radiance $L_{TH\,BB}$ through:

$$F = \frac{\pi . L_{TH\,BB}(VZA)}{R(VZA)}$$

For small VZA, the measured radiance is mainly coming from the surface (or optically thick objects like clouds) while for higher VZA (at grazing angles), the influence of the increased atmospheric path is predominant due to its absorption/emission. The radiance measured at nadir is then statistically higher than the mean hemispherical radiance because the surfaces have higher temperatures than high altitude atmospheric layers. On the other hand, for grazing angles, the measured radiance is usually smaller. Therefore, the anisotropic factor

should be higher than 1 for small VZA values and smaller than 1 for grazing angles. At mid-value VZA, near 50°, the measured radiance is a good average of these two effects and is then a good estimator of the flux (Clerbaux et al., 2006; Otterman et al., 1997).

7.4 Algorithm validation

This section presents the validation works of the successive steps involved in the TOA fluxes processing. Note that further validation of the monthly mean fluxes against CERES EBAF data are presented in section 9.1.

7.4.1 Scene identification

The methods involved in the scene identification process have been validated by Ipe et al. (2010, 2004) and Ipe (2011).

7.4.2 Narrowband to broadband conversion

The NB to BB conversions have been validated in Clerbaux (2008).

7.4.3 Broadband radiances to fluxes conversion

The CERES TRMM SW ADMs have been validated by Loeb et al (2003b). Instantaneous SW flux error is evaluated at 13 W/m^2.

The thermal flux estimation from the Meteosat WV and IR channels has been addressed by several teams. For the proposed scheme, see Clerbaux (2008).

7.5 Assumptions and limitations

- The cloud phase retrieval suffers from several limitations. For example, the misidentification of super cooled water clouds as ice clouds and the misidentification of transparent clouds as water clouds. It seems difficult to improve the cloud phase determination given the limited information available in the 3 channels of MVIRI.

- The scene identification process is highly unreliable over snow covered regions as they exhibit VIS reflectance similar to the ones of clouds. The frequency of snow is however relatively limited in the Meteosat FOV.

- For permanent snow/ice surfaces, the bright desert ADMs are used since they are the closest models in terms of albedo. However, empirical snow ADMs are now available from Kato & Loeb (2005). They might be used in future Editions of the data record.

- The NB-to-BB regressions and the ADM selection are based on constant surface type map. This could introduce flux error in region of seasonally varying vegetation like the Sahel and also in regions that have experienced significant changes during the last decades.

- The spectral dependency of the emissivity is not taken into account within the SBDART plane-parallel radiative transfer model simulations. The surface emissivity is a random number with uniform distribution of probability in the range [0.85, 1]. This range is selected to represent the emission decrease observed over sandy surface.

- High and semi-transparent clouds (cirrus) are insufficiently represented in the SBDART data record (only 5% of the simulations).

- Clerbaux et al. (2003b) have shown that the geostationary TET fluxes may exhibit some bias (about 1%) in mountainous areas as the angular dependency models do not account for azimuthal anisotropy. Indeed, from a geostationary orbit, the Northern hemisphere is always observed from the South while it is the reverse in the Southern hemisphere. A correction could be based on statistical analysis of CERES observations in the Meteosat FOV to perform an a-posteriori correction of the clear sky thermal fluxes. It is currently not foreseen to correct this effect in this edition of the CM SAF clear sky product.

- It is expected that the ADM for the thermal radiation will underestimate the anisotropy in case of high semi-transparent clouds. This results in overestimation of the thermal flux in the center of the field of view (VZA < 50°) and underestimation on the disk edges (VZA > 50°). Similar effect is observed in the GERB ED01 data record. This effect is especially apparent over the warm tropical oceans (see the comparison with CERES EBAF in the Validation Report [RD9]).

7.6   Future enhancements

Future enhancements of the TOA fluxes processing may concern the limitations and assumptions stated in the previous section.

8   Algorithm description (part 4/4): Daily and monthly averaging and spatial re-gridding

8.1   Purpose of the daily and monthly averaging

The purpose of this last part of the processing is to average and output the daily mean, monthly mean and monthly mean diurnal cycle of the TRS and TET fluxes. The outputs are projected on a regular grid at a spatial resolution of 0.05° to maintain consistency with other CM SAF products.

In the absence of missing data, the averaging algorithm is straightforward: a simple integration would provide the wanted quantities. However, a large number of missing data affects the data record. These slots consist of initially lacking data but also of corrupted data that were discarded from the processing to avoid computing erroneous fluxes (see section 6.3.1). Missing TRS data is also observed in case of ocean sun glint conditions. The daily averaging process accounts for these gaps by interpolating the missing data. However, the interpolation of too many successive missing slots could bias the daily mean. It is therefore important to estimate the maximum acceptable number of successive missing slots which can be interpolated. Figure 35 shows how accepting short data gaps reduces the number of days (out of 9104) for which the daily mean is not estimated.
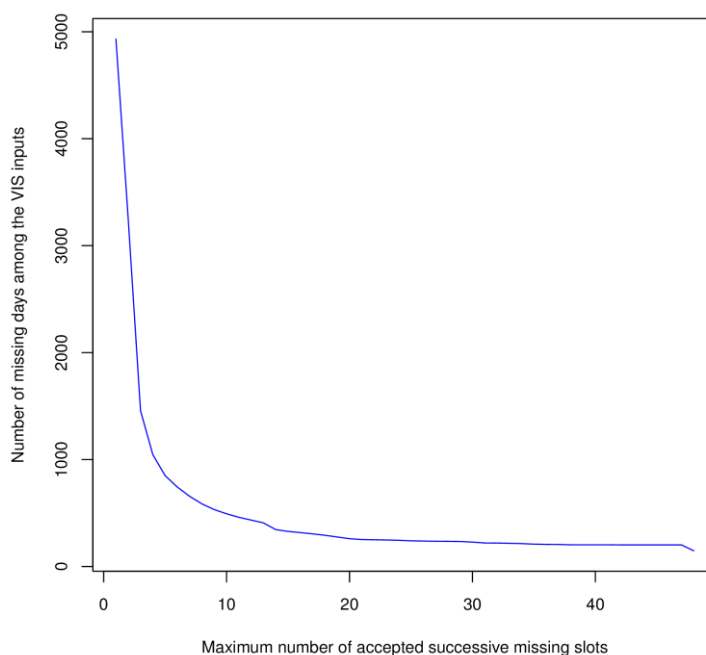

Figure 35: Number of rejected days among the VIS inputs as a function of the criterion on the maximum number of successive 30 minutes missing MVIRI slots.

Clearly, a limited amount of successive missing data should be accepted in the averaging algorithm provided that it does not bias the products and improve their RMS difference with the true averaged fluxes. Missing data are interpolated between a maximum of 3 hours, which correspond to 5 successive missing data for MVIRI and 11 for SEVIRI. An objective estimation of this maximum acceptable number of successive missing data is given in Section 8.4 to justify this choice.

With this criterion, the number of missing days among the MVIRI VIS inputs is 850 out of 9104. Most of these missing days (579) are found during the Meteosat-2 operational period. The effect on the averaged products is discussed in section 8.4.

8.2   Algorithm overview

The first step of the algorithm performs the solar and thermal fluxes averaging in hourly intervals (defined in UTC time). This process is also in charge of the interpolation of the missing data. The daily averaging is then performed from these hourly means. A 'daily flag' indicates if the criterion of the 3 maximum successive missing hours is met or not (at the image level, not at the pixel level). Then the monthly mean diurnal cycle is computed from the hourly means, excluding the days which were flagged as incomplete. A minimum number of 15 days is required to compute the monthly mean for each hourly interval (diurnal cycle). In addition, the seasonal change in solar insolation during the month is taken into account in the implementation of the diurnal cycle. Finally, the monthly mean is evaluated as simple averaging of the diurnal cycle.

To avoid introduction of discontinuity in the diurnal cycle, only the days which are not flagged as incomplete are considered.

It should also be noted that the non-linearity of the fluxes according to the SZA is taken into account in the TRS fluxes integration by converting the TRS fluxes into TOA albedos. Therefore, changes in the SZA values over the month is also taken into account when computing the monthly mean diurnal cycle.
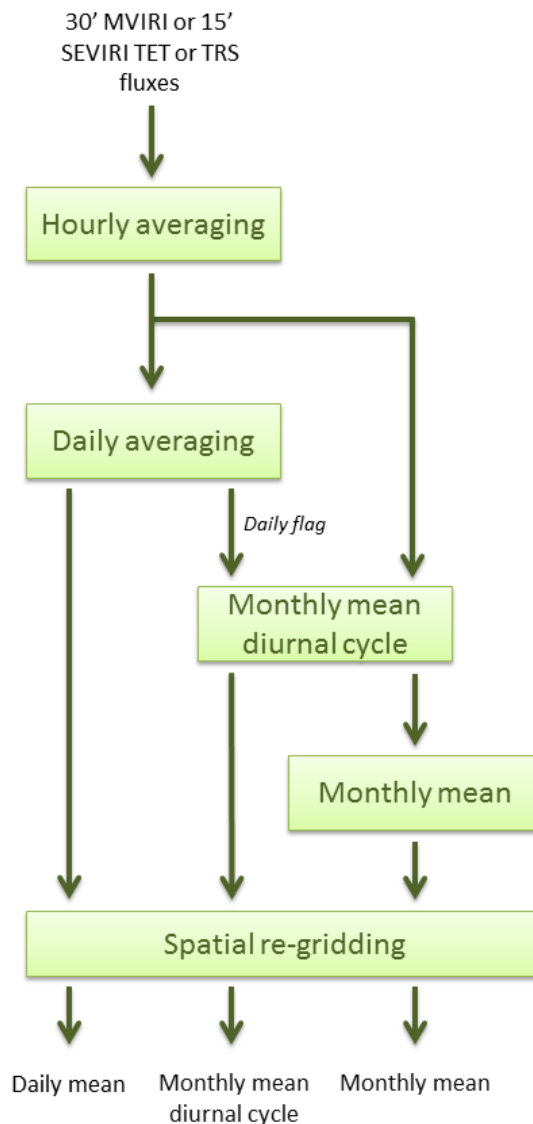
Figure 36: Overview flowchart for the daily and monthly averaging. The 'daily flag' indicates if the criterion on the maximum number of successive missing repeat cycles is met or not (at the image level, not at the pixel level).

8.3 Algorithm description

8.3.1 Hourly integration

The hourly integration process starts with a preprocessing of the input TRS and TET fluxes. The two 30' MVIRI (resp. four 15' SEVIRI) measurements done within the 1-hour interval are collected. Since the hourly integration process is also in charge of the interpolation for the gaps filling, the five (resp. eleven) measurements done just before and just after the interval are also collected. It allows interpolating missing data from measurements located within a maximum period of time of 3 hours. The TRS fluxes integration also requires collecting the SZA at the time of acquisition to convert the TRS fluxes into TOA albedos. The reason for this conversion is that the non-linearity of the TOA fluxes according to the SZA is more pronounced than for the albedos. Moreover, the conversion is only performed for SZA < 85°

using the cosine of the SZA and the TSI (from the RMIB TSI composite, see Section 4.4.6) corrected for the Earth-Sun distance (*d*).

The hourly integration of the TRS albedos and TET fluxes is carried out by piecewise integration between the available measurements using 12 time intervals of 5 minutes. Such a division allows accounting for the highly non-linear variations of the SZA with time.

For the TRS, the averaged flux is computed according to the SZA at the centre of the interval as:

- 0 in night-time condition (SZA > 100°),

- a modelled flux (Kato and Loeb, 2003) in twilight condition (SZA > 85° and < SZA 100°),

- the flux at the centre of the interval computed from the TOA albedo interpolated at this time from the available time series of albedos (*Alb*), using the following relation :

$$F_{TRS} = \frac{Alb.TSI.\cos(SZA)}{d^2}$$

It should be noted that since the processing limits were previously fixed at SZA=80°, the fluxes for the region 80°<SZA < 85° are extrapolated at this time from the time series of observations with SZA<80°. The extrapolation is done by assuming a constant albedo.

When no data is available before or after one of the 12 time intervals of 5 minutes, the flux at the centre of the interval is extrapolated from the available measurements located respectively after or before the interval within a maximum 1.5 hour period. This situation is most likely occurring at dusk and dawn. When no interpolation or extrapolation is possible, the hourly mean is set to incomplete.

8.3.2 Daily mean

For each pixel, the daily mean is computed from the 24 hourly integrations. In case one or several of these 24 values are missing (it was set to incomplete), the daily mean pixel is set to the fill-value, i.e. -1.0. The basic principle of the daily averaging is shown on the Figure 37.

If this occurs for all the pixels, the day is flagged as 'incomplete' and no daily mean will be issued (this flag is also used to discard the day in the monthly averaging, see after).
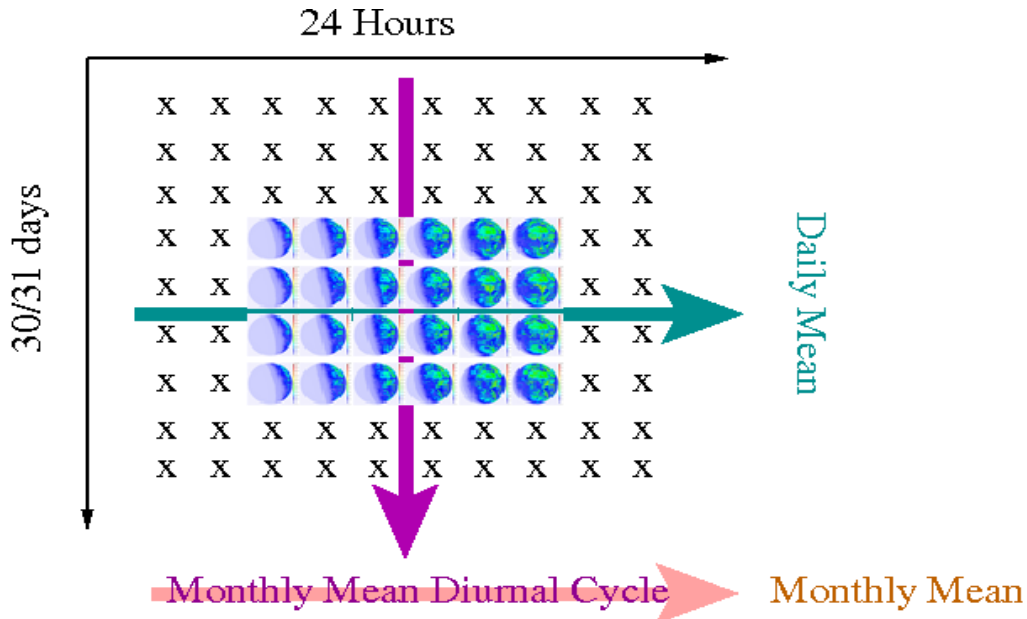
Figure 37 : Averaging strategy: from the hourly integrated data to the daily mean, to the monthly mean diurnal cycle and to the monthly mean product.

8.3.3 Monthly mean diurnal cycle

From the hourly data, the diurnal cycle is computed as the average of the available hourly values for the calendar month. To avoid introduction of discontinuity in the diurnal cycle, only the days which are not flagged as incomplete are considered. A minimum number of 15 days is required to compute each hourly interval of the diurnal cycle (at the pixel level). In addition, the seasonal change in insolation during the month is taken into account by correcting the monthly mean of the available TRS hourly integrations ($MD_{H, TRS}$) as follows:

$$MD_{H,TRS} = MD_{H,TRS} * \frac{MD_{H,TIS}}{MD_{H,TIS\ with\ obs}}$$

where $MD_{H, TIS}$ is the monthly mean of the TIS hourly integrations for all the days, even those without any TRS hourly observation, while $MD_{TIS\ with\ obs}$ is only computed over the days with available TRS hourly observations.

If the 15 days criterion of available hourly integrations is not met for all the pixels, the diurnal cycle is flagged as 'incomplete' and no monthly mean will be issued for this hourly interval.

8.3.4 Monthly mean

Finally, the monthly mean is evaluated as simple averaging of the diurnal cycle. In case one or several of the 24 monthly 1-hourly means are missing (it was set to incomplete), the monthly mean pixel is set to the fill-value, i.e. -1.0. If this occurs for all the pixels, the month is flagged as 'incomplete' and no monthly mean will be issued.

Obviously, the seasonal change in insolation during the month is therefore also taken into account in the monthly mean. It should be noted that there is no mixture of MVIRI and SEVIRI in the monthly products.

8.3.5 Spatial re-gridding

To ensure consistency with other CM SAF products, the TRS and TET fluxes data records are re-gridded on a common regular latitude-longitude grid at a spatial resolution of 0.05°. To perform the transformation, a twin target image is built in which each target pixel has a list of the corresponding pixels in the source image and their associated weights. The re-gridding is performed supposing the energy (density of flux) equally distributed in the original pixel. This assumption allows estimating the re-gridded pixel flux using the surface intersection as weighting of the original pixel flux densities.

After re-gridding, the spatial coverage may be limited, e.g. to 60°N - 60°S and 60°W- 60°E. This will be decided in view of the validation results.

8.4   Algorithm validation

The methods involved in the daily and monthly averaging steps have already been validated for the GERB Edition 2 data record and are documented in [RD 7]. The validation mainly concerns the gap filling and how to set objectively the maximum acceptable number of successive missing repeat cycles (MRC). To this end, gaps have been simulated in the data record for one day with full coverage (by removing input data) and the effect on the daily mean product has been evaluated in terms of bias and RMS. Table 21 gives the biases and RMS errors that were obtained for simulated gaps of 3, 6, 9, 12, 15, 18 and 21 MRC (out of 96 per day for GERB), each time by averaging 10 simulations with varying position of the gap.

As the MVIRI/SEVIRI data record targets a stability of 0.6 W/m^2/dec, it is proposed to set the maximum acceptable number of successive MRC to 5 for MVIRI and 11 for SEVIRI, so the systematic effect of the missing cycles (the mean absolute bias) remains lower than 0.6 W/m^2/dec. With this criterion, the RMS error on the daily mean product will be about 4 W/m^2 for the TRS and 1 W/m^2 for the TET, which is in-line with the target accuracy. This criterion allows the interpolation of missing data up to 3 hours between actual observations and it is thus a trade off between data record completeness and daily mean accuracy. It is also consistent with most satellite climatologies (like the ISCCP) which have historically been based on 3-hourly geostationary data.

Table 21 : Effect of successive missing 15' repeat cycle (MRC) on daily mean TRS and TET fluxes from [RD 7].

Number of successive 15' MRC	TRS mean bias (W/m^2)	TRS mean abs. bias (W/m^2)	TRS RMS (W/m^2)	TET mean bias (W/m^2)	TET mean abs. bias (W/m^2)	TET RMS (W/m^2)
3	-0.0155	0.0372	0.5220	-0.0005	0.0005	0.1991
6	-0.0787	0.1790	1.3863	0.0008	0.0008	0.5008
9	-0.2295	0.4605	2.5884	0.0017	0.0017	0.8680
12	-0.5115	0.9630	4.1190	0.0049	0.0049	1.2865
15	-0.9686	1.6298	5.9550	0.0086	0.0086	1.7490
18	-1.5665	2.5190	8.0909	0.0239	0.0239	2.2697
21	-2.3092	3.6872	10.4854	0.0457	0.0457	2.8475

8.5 Assumptions and limitations

- In case of missing data the TRS flux is obtained by interpolation in terms of TOA albedo which is known to increase at high SZA. This could introduce a small underestimation of the flux in case of missing data close to the SZA=85° limit. The TOA albedo interpolation would ideally incorporate some typical variation with the SZA.

- With geostationary observations, the viewing geometry is obviously fixed. This is likely to introduce some systematic error in the diurnal cycle products.

8.6 Future enhancements

Future enhancements of the daily and monthly averaging steps may concern the limitations stated in the previous section.

9   Preliminary validations

This section presents some comparisons of products generated with the described algorithm with corresponding CERES EBAF products. These results are based on a preliminary processing of the data record which did not display all the features included in the final version of the data record. In particular, the operational calibration provided by EUMETSAT was used to process the IR and WV channels of the MVIRI instruments instead of the EUMETSAT/GSICS recalibration of MVIRI using HIRS (R. Stöckli and A. Tetzlaff, pers. comm.). In addition, the VIS channels of SEVIRI were processed using the SSCC calibration method (Govaerts et al., 2004) instead of the KNMI inter-calibration with MODIS (Meirink et al., 2013). Comprehensive and updated validations will be provided in the Validation Report [RD9].

9.1   Comparison with CERES EBAF Ed2.8

The monthly mean fluxes have been compared with CERES EBAF Edition 2.8. As examples, results of June 2000 for Meteosat-7 are displayed on Figure 38 (TRS) and Figure 39 (TET). Mean values, RMS errors and standard deviations computed in the region between 50°S, 50°N, 50°E and 50°W (which approximately corresponds to VZA<60°), are also provided in the figures. This gives a preliminary insight on the CM SAF monthly mean accuracy at 1°x1° spatial scale (to be consolidated in the validation activities).

Concerning the solar fluxes (Figure 38), the mean difference between CM SAF and CERES EBAF Ed2.8 fluxes is 2.18 W.m^{-2} with a standard deviation of 4.16 W.m^{-2} (i.e. bias corrected RMS) which lies very close to the target accuracy of 4 W.m^{-2} for the TRS monthly mean flux In this example, differences are mainly observed over the Gulf of Guinea, over Mozambique and Tanzania and around the Bab-el-Mandeb strait. For other months of the time series (not shown) the areas with significant CM SAF / CERES differences seem to move according to the Intertropical Convergence Zone's position.

Concerning the thermal flux (Figure 39), the mean difference between CM SAF and CERES EBAF Ed2.8 fluxes is -7.73 W.m^{-2} with a standard deviation of 3.09 W.m^{-2}. The significant bias is introduced by the GERB thermal flux level which is about 2% lower than CERES. This significant bias is also observed in the GERB-CERES comparison (Clerbaux et al., 2009). The standard deviation of 3.09 W.m^{-2} lies between the threshold and target accuracies (resp. 4 W.m^{-2} and 2 W.m^{-2}). Looking at the difference panel on Figure 39 most of the error can be attributed to the thermal ADM in case of high semi-transparent clouds. This is the likely reason of the slight underestimation of the anisotropy that introduces the apparent "limb-darking" in the difference and ratio images: positive differences are observed in the centre of the FOV (close to nadir Meteosat observation) and negative differences on the edge of the FOV (grazing observation).

Figures 40 and 41 show similar patterns of regional differences, respectively for the TRS and TET fluxes for the months of June from 2001 to 2006. The comparisons are similar as for June 2000 except for the TET fluxes for June 2001. For this month many regional differences with respect to CERES EBAF Ed2.8 are observed. After investigation, the calibration does not seem to be responsible for these regional patterns. The reason for these patterns is quite

difficult to attribute. Most likely, it may come from missing MVIRI or CERES data affecting the monthly mean TET sampling for this month.
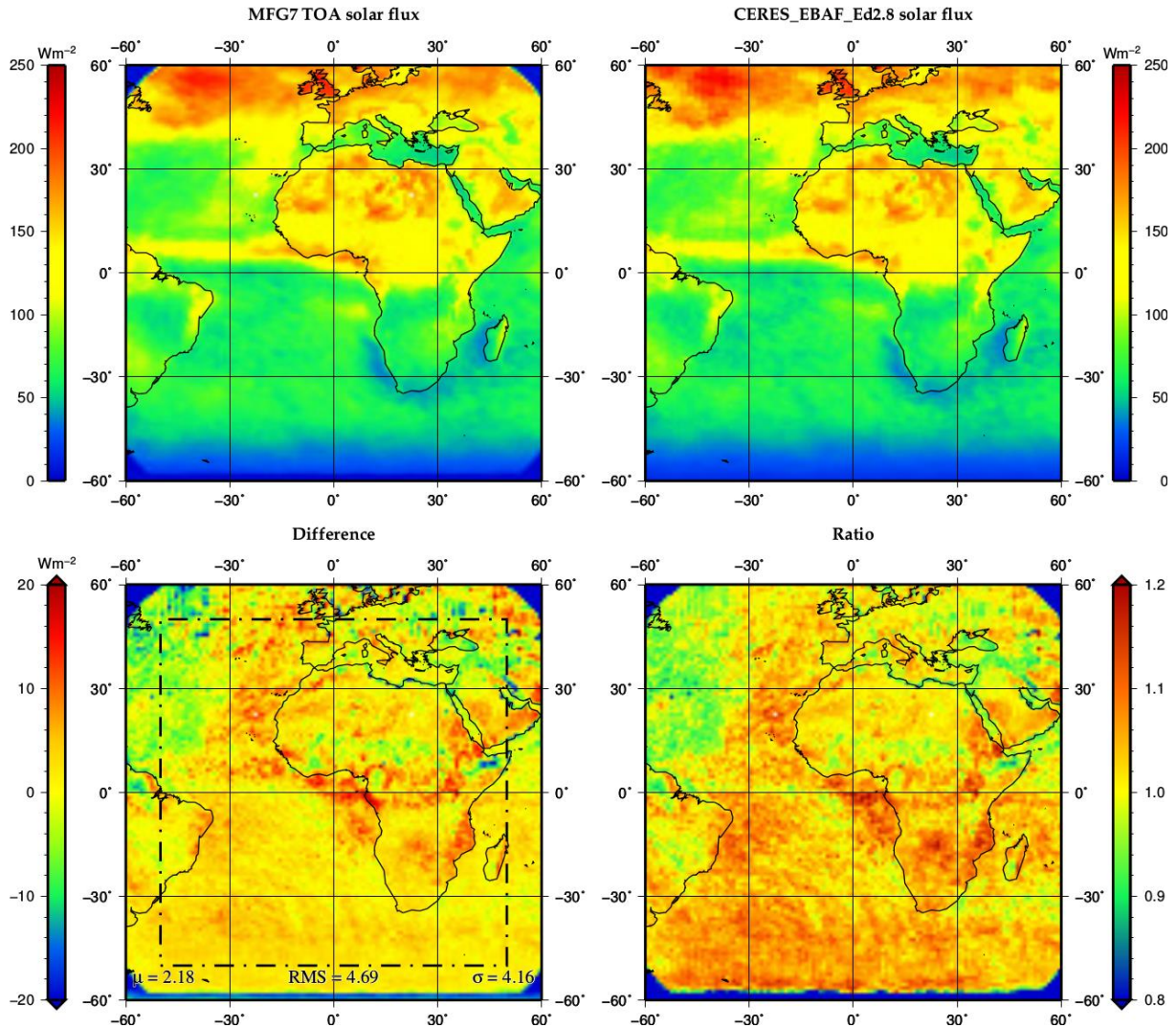
Figure 38 : Comparison of June 2000 MET-7 monthly mean TRS fluxes from CM SAF (top left) and CERES EBAF Ed2.8 (top right). The bottom images show the difference (left) and ratio (right).

Figure 39: Comparison of June 2000 MET-7 monthly mean TET fluxes from CM SAF (top left) and CERES EBAF Ed2.8 (top right). The bottom images show the difference (left) and ratio (right).

Figure 40: MET-7 monthly mean TRS comparison with CERES EBAF Ed2.8 for June 2001 (top left), 2002 (top right), 2003 (middle left), 2004 (middle right), 2005 (bottom left) and 2006 (bottom right). For each month, 4 images are provided that give the CM SAF and EBAF fluxes and their difference and ratio, as for Figure 39.

Figure 41: MET-7 monthly mean TET comparison with CERES EBAF Ed2.8 for June 2001 (top left), 2002 (top right), 2003 (middle left), 2004 (middle right), 2005 (bottom left) and 2006 (bottom right). For each month, 4 images are provided that give the CM SAF and EBAF fluxes and their difference and ratio, as for Figure 39.

Similar comparisons have been done for months based on MSG. As examples, results for June 2004 are displayed on Figure 42 (TRS) and Figure 43 (TET). Concerning the solar fluxes, the mean difference between CM SAF and CERES EBAF Ed2.8 fluxes is 2.39 W.m^{-2} with a standard deviation of 3.79 W.m^{-2}. Here also the product is close to the accuracy target of 4 W.m^{-2}. The main differences are observed over and west of the Gulf of Guinea and around the Bab-el-Mandeb strait.

Concerning the thermal flux, the mean difference between CM SAF and CERES EBAF Ed2.8 fluxes is -7.60 W.m^{-2} with a standard deviation of 2.52 W.m^{-2}. The product accuracy is then close to the target accuracy of 2 W.m^{-2} (and agrees with the threshold accuracy of 4 W.m^{-2}). Figures 44 and 45 show similar patterns of regional differences, respectively for the TRS and TET fluxes, for the months of June 2005 and 2006.

Figure 42: Comparison of June 2004 MET-8 monthly mean TRS fluxes from CM SAF (top left) and CERES EBAF Ed2.8 (top right). The bottom images show the difference (left) and ratio (right).
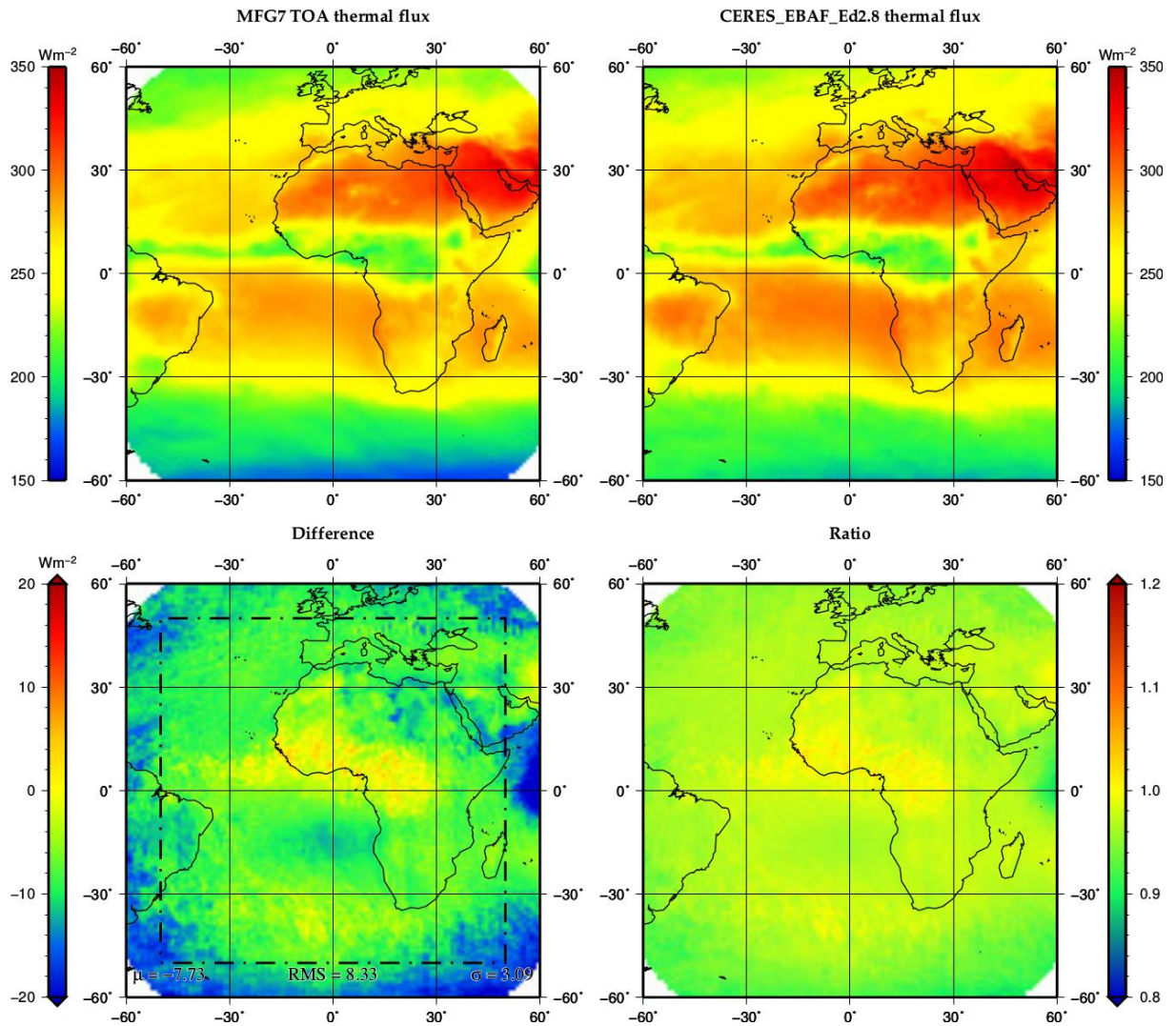
91

Figure 43: Comparison of June 2004 MET-8 monthly mean TET fluxes from CM SAF (top left) and CERES EBAF Ed2.8 (top right). The bottom images show the difference (left) and ratio (right).
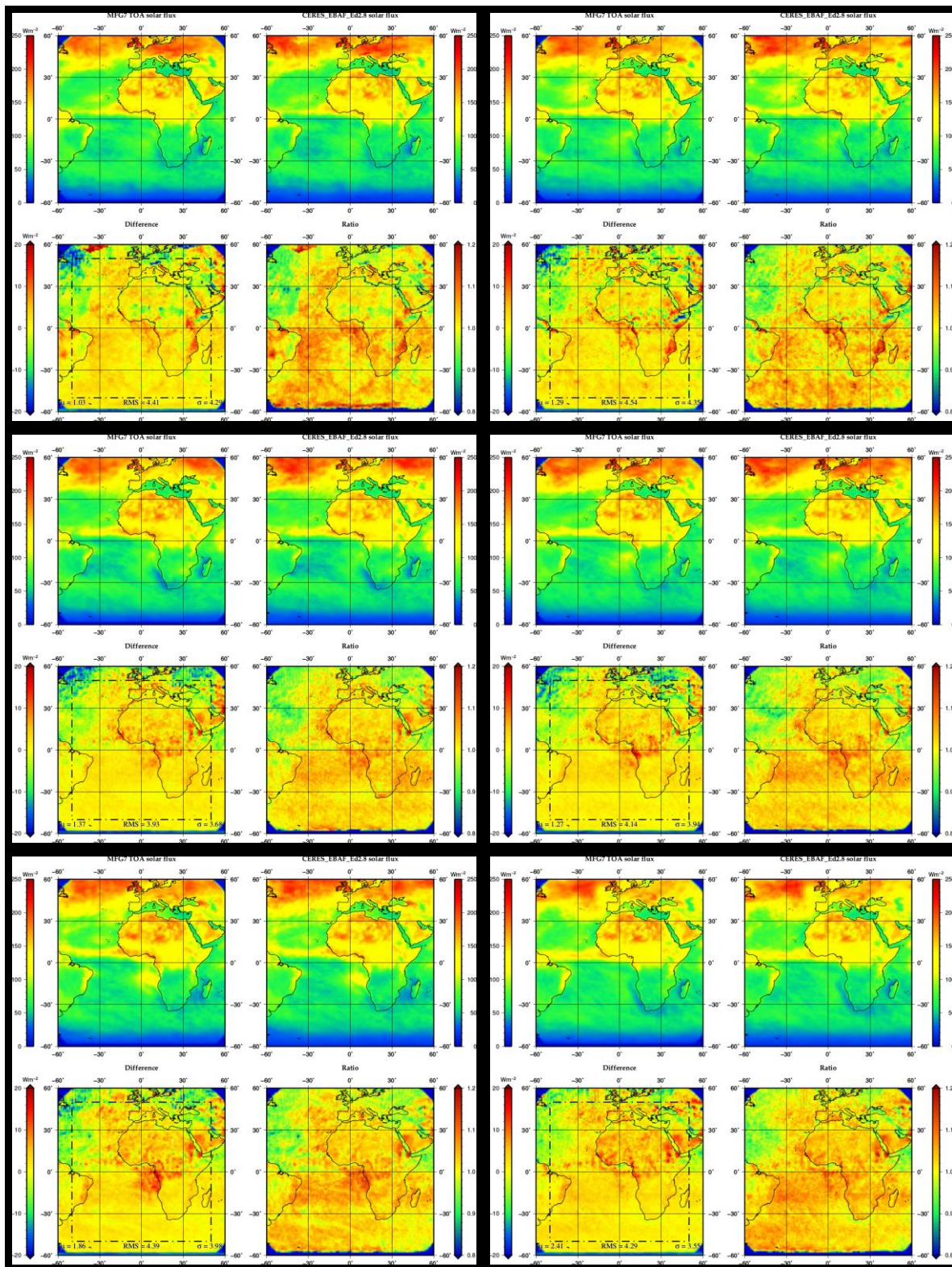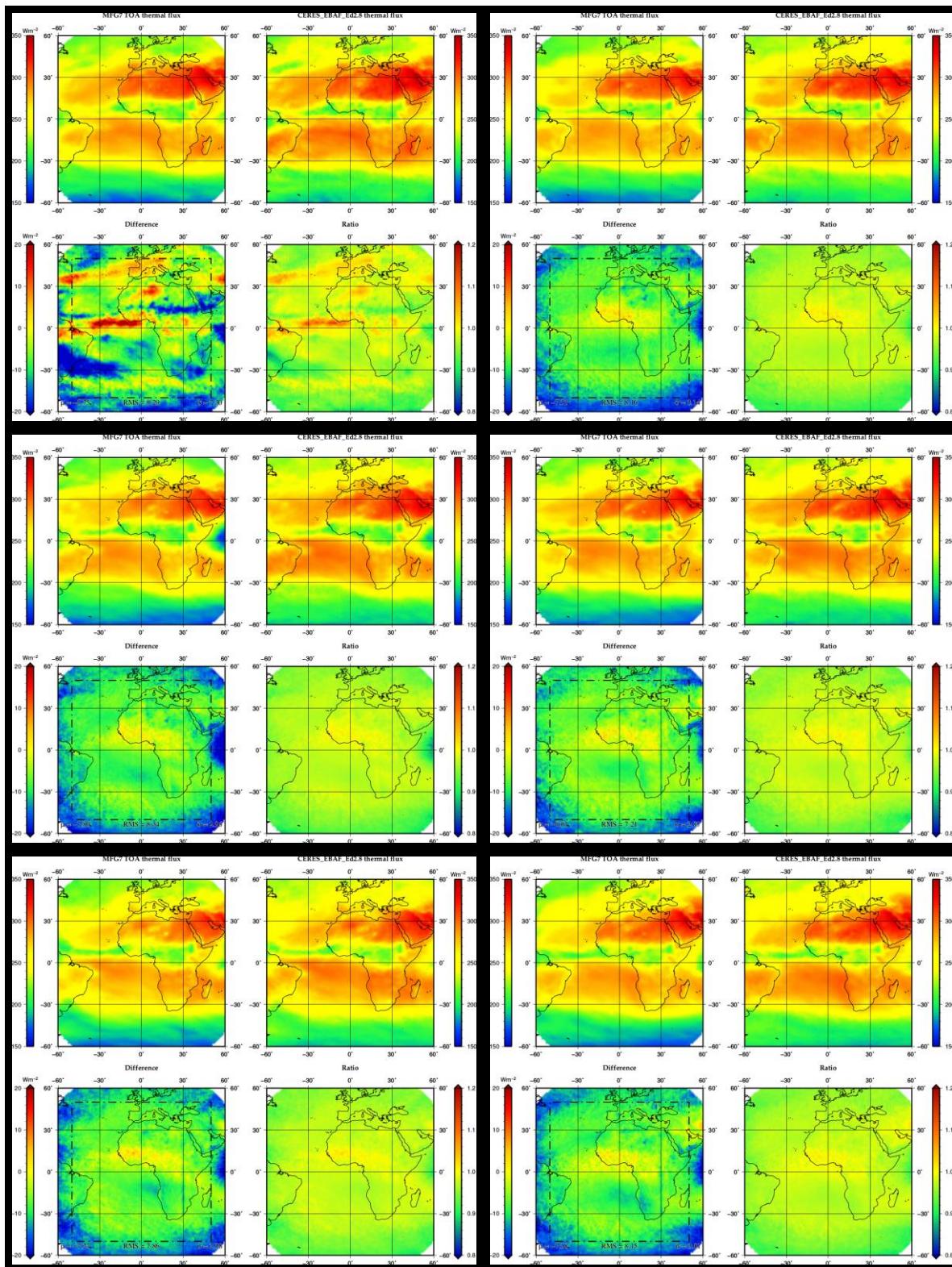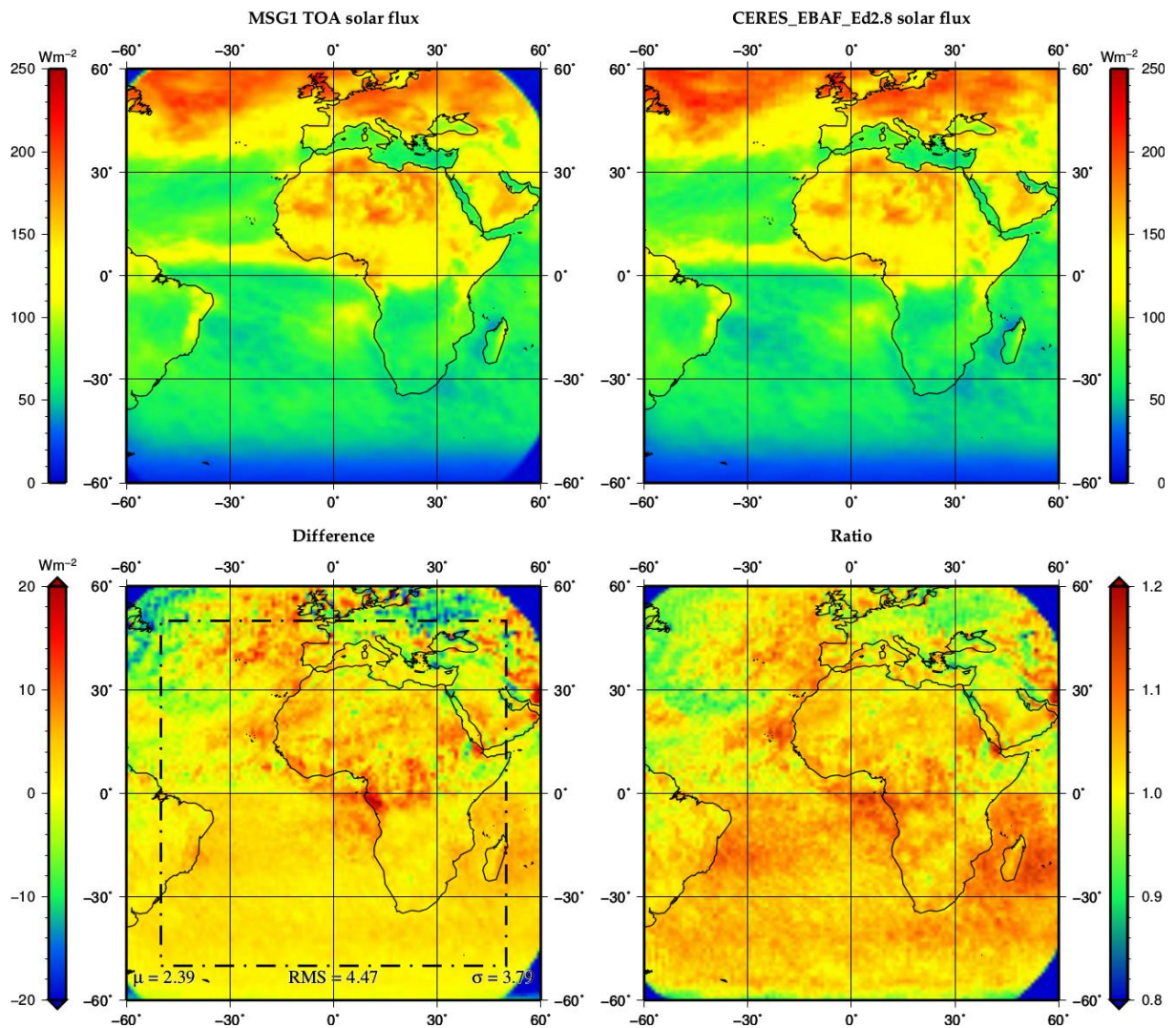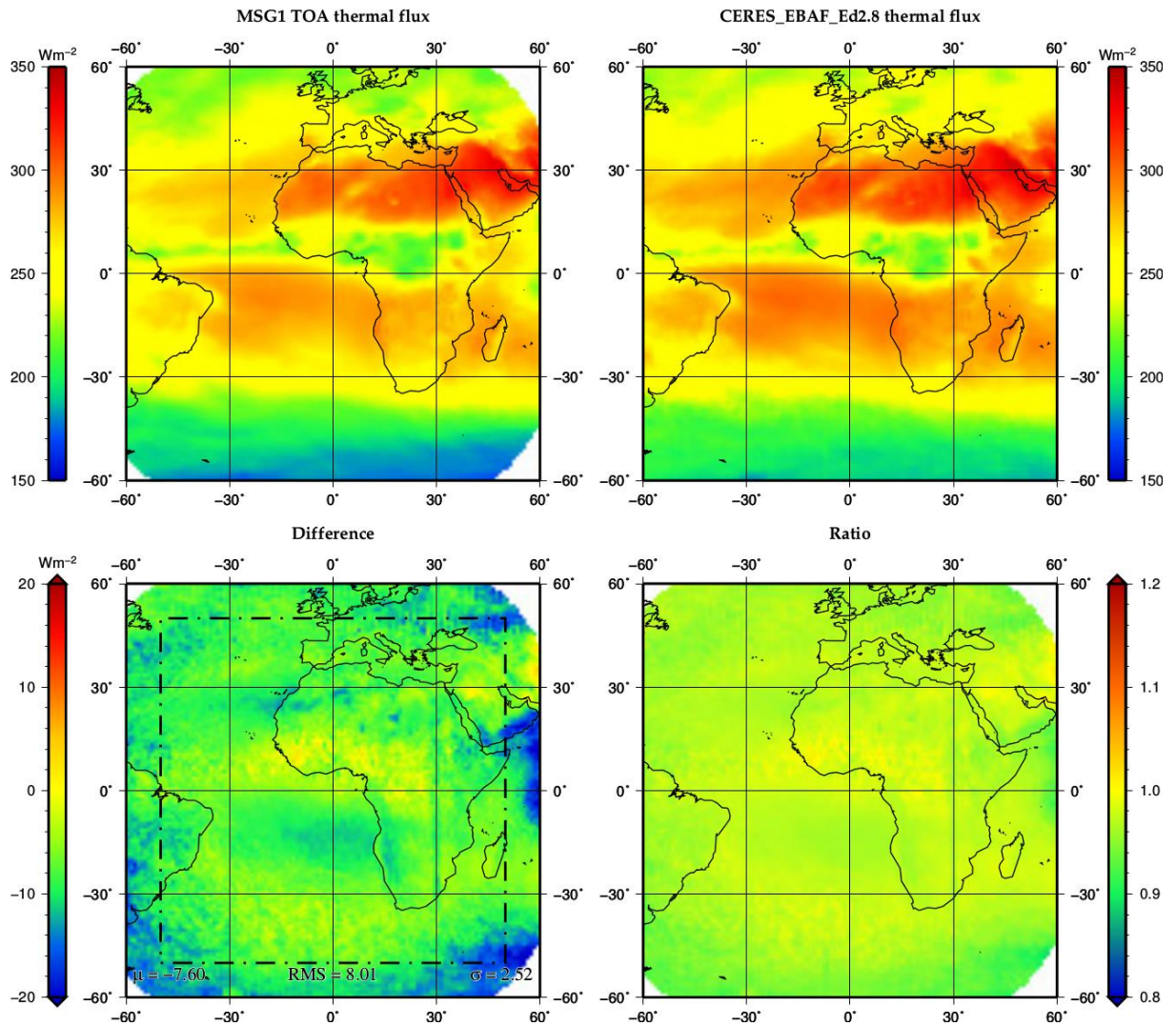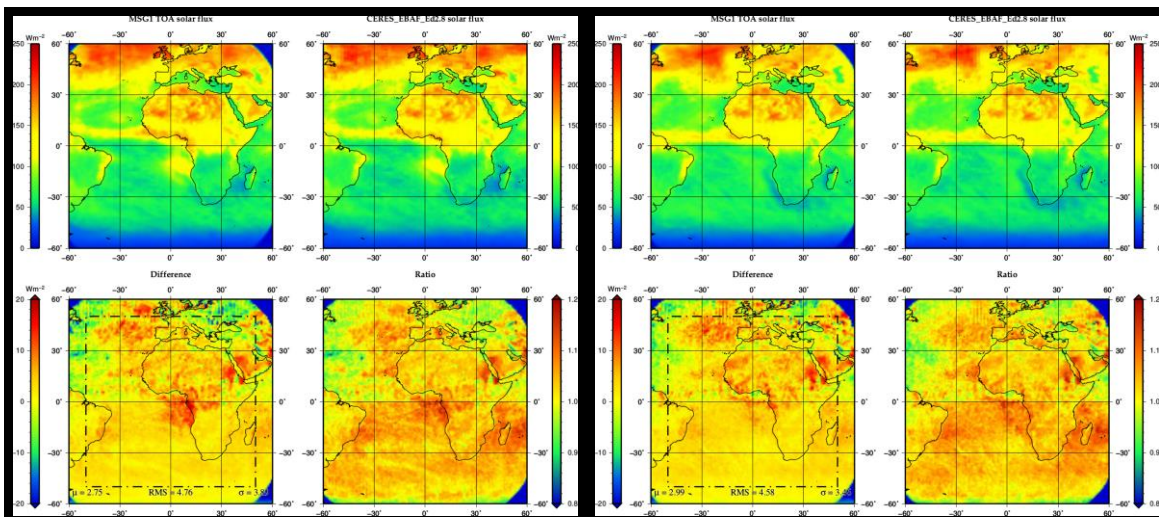
Figure 44: MET-8 monthly mean TRS comparison with CERES EBAF Ed2.8 for June 2005 (left) and 2006 (right).
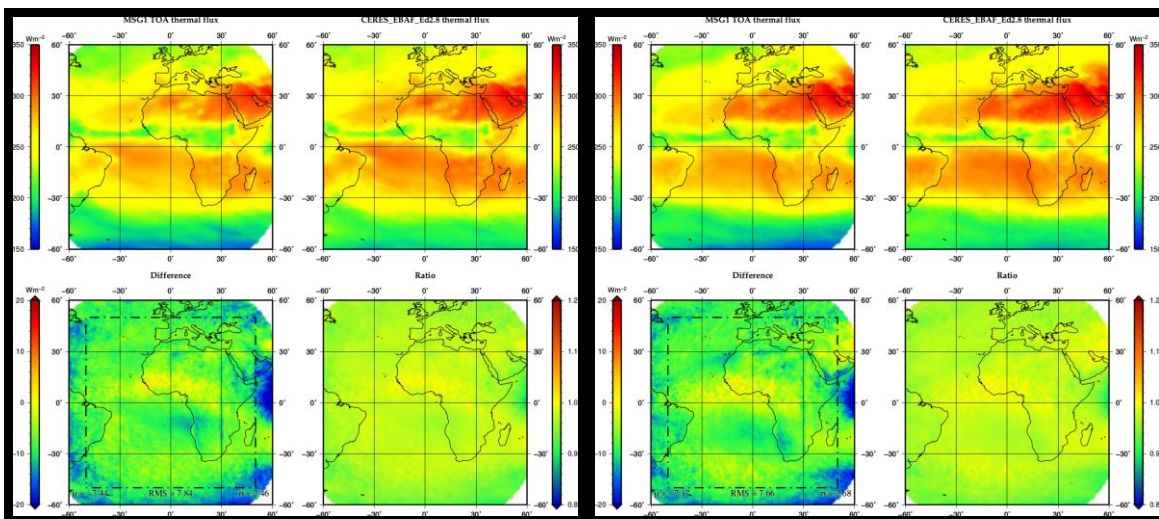
Figure 45: MET-8 monthly mean TET comparison with CERES EBAF Ed2.8 for June 2005 (left) and 2006 (right).

9.2 Temporal stability with respect to CERES EBAF Ed2.8

To assess the stability of the CM-23311 and CM-23341 data records, some successive Meteosat monthly mean products have been compared to CERES EBAF Ed 2.8. Figure 46 shows the overall all-sky bias for the months of June from 2000 to 2006. The overall TRS bias relative to CERES remains between -1.5 W/m^2 and 1.0 W/m^2 and the TET bias between -8.0 W/m^2 and -5.5 W/m^2. Such a result is consistent with the threshold stability of 4 W/m^2/decade. It should be noted that the TRS products include the GERB-2 SW channel calibration update.

The residual RMS difference (bias corrected) is shown in Figure 47. The overall TRS RMS difference with respect to CERES EBAF is about 4 W/m^2 and the TET RMS difference is about 2.5 W/m^2.

93

Absolute bias CMSAF - EBAF
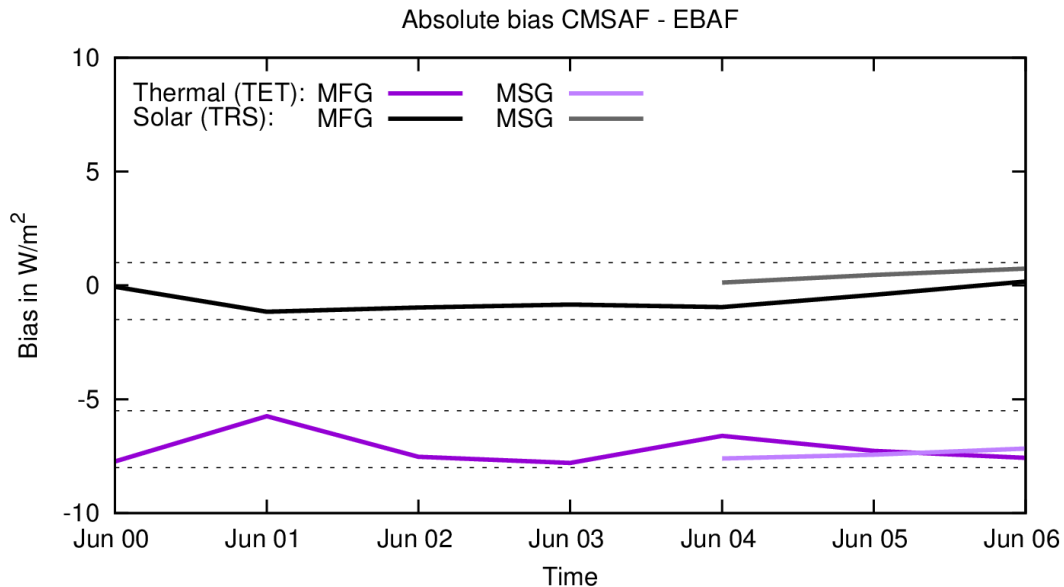
Figure 46: Bias between Meteosat CM SAF and CERES EBAF monthly mean all-sky TRS (in black for Meteosat-7 and grey for Meteosat-8) and TET (in dark purple for Meteosat-7 and light purple for Meteosat-8) fluxes for the month of June from 2000 to 2006. As shown in dotted lines, the variation of the bias is consistent with a stability of 2.5 W/m^2 for both the TET fluxes.

RMS difference CMSAF - EBAF (bias corrected)
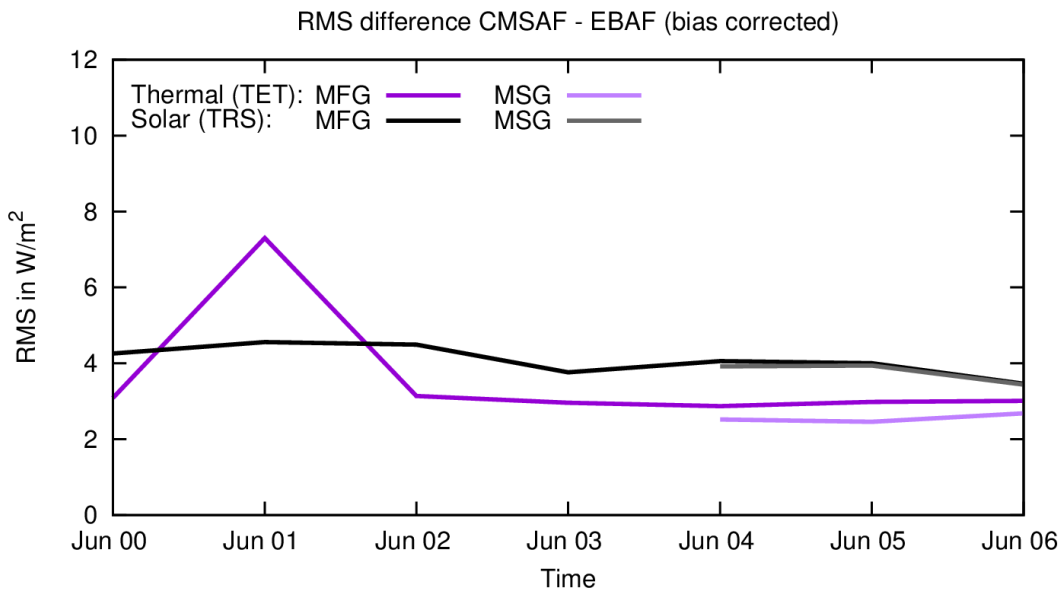
Figure 47: RMS (bias corrected) between Meteosat CM SAF and CERES EBAF monthly mean all-sky TRS (in black for Meteosat-7 and grey for Meteosat-8) and TET (in dark purple for Meteosat-7 and light purple for Meteosat-8) fluxes for the month of June from 2000 to 2006.

9.3 Overall time series stability on main surface types

The TOA fluxes processing algorithm (see section 7) has been applied in a clear-sky mode to process the 12 UTC repeat cycle over the full data record. The CS mode uses as input the visible CS products delivered by the visible CS processing (see section 5) and computes the CS TRS fluxes (the TET fluxes are not delivered). Figure 48 shows the time series of the CS TRS fluxes averaged over 5 scene types while Figure 49 shows the anomalies for those time

series. The use of CS fluxes allows being independent of change in cloudiness but the time series may still suffer of natural changes in aerosol content and surface albedo. The effect of the Mount Pinatubo eruption in 1991 is well visible with increase of the TRS flux over dark surfaces (ocean, dark vegetation) and decrease over bright surfaces (bright desert). The decrease over bright surfaces indicates that the absorption from volcanic aerosols is not negligible.
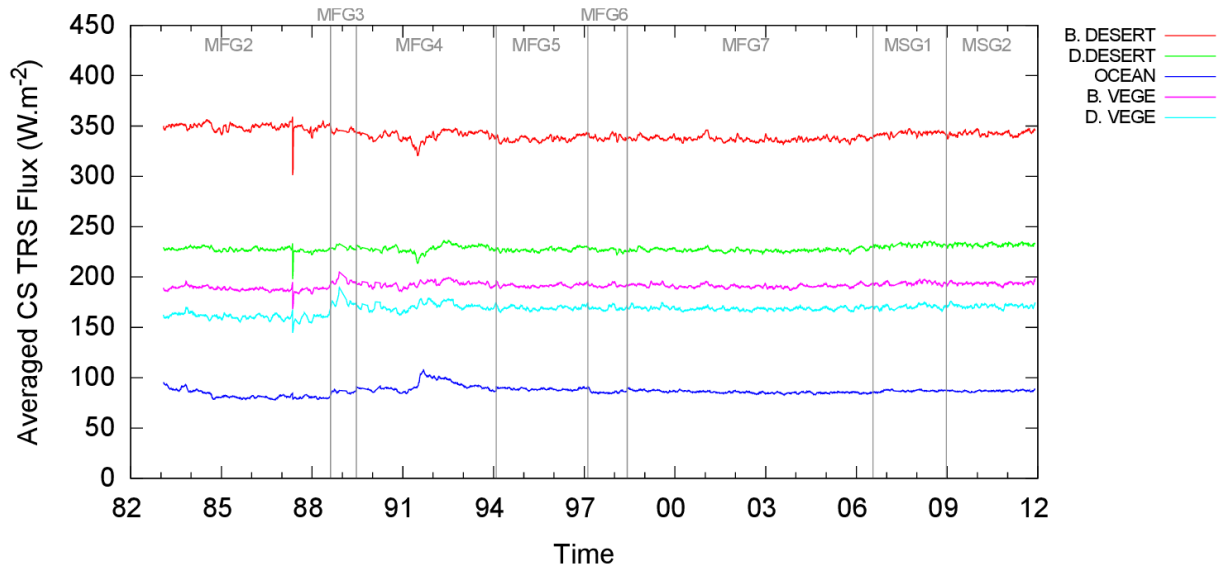
Figure 48: Time series of averaged CS TRS fluxes according to various surface types (colored curves).
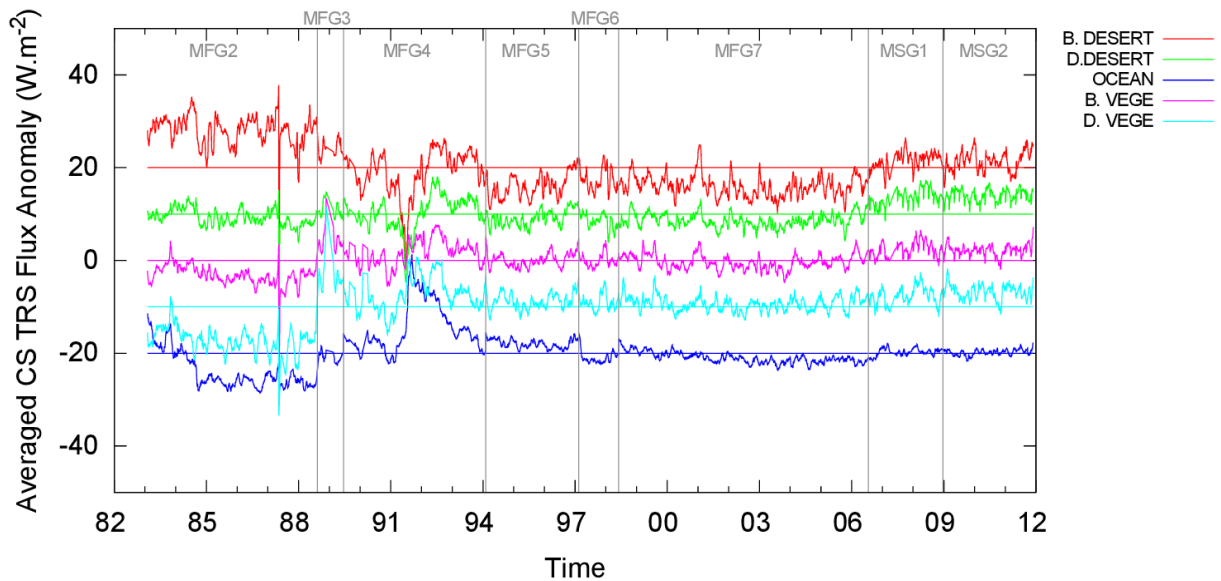
Figure 49: Time series of anomalies for the averaged CS TRS fluxes according to various surface types (coloured curves). The anomalies are obtained by subtracting the average TRS flux (coloured straight lines) from the time series. An additional shift of -20 W/m^2, -10 W/m^2, 0 W/m^2, +10 W/m^2, +20 W/m^2 is done to improve the readability of the graph.

95

Figure 50 shows the time series of the CS TRS fluxes averaged over the whole Meteosat disk without any surface type distinction while Figure 51 shows the anomalies for this time series.
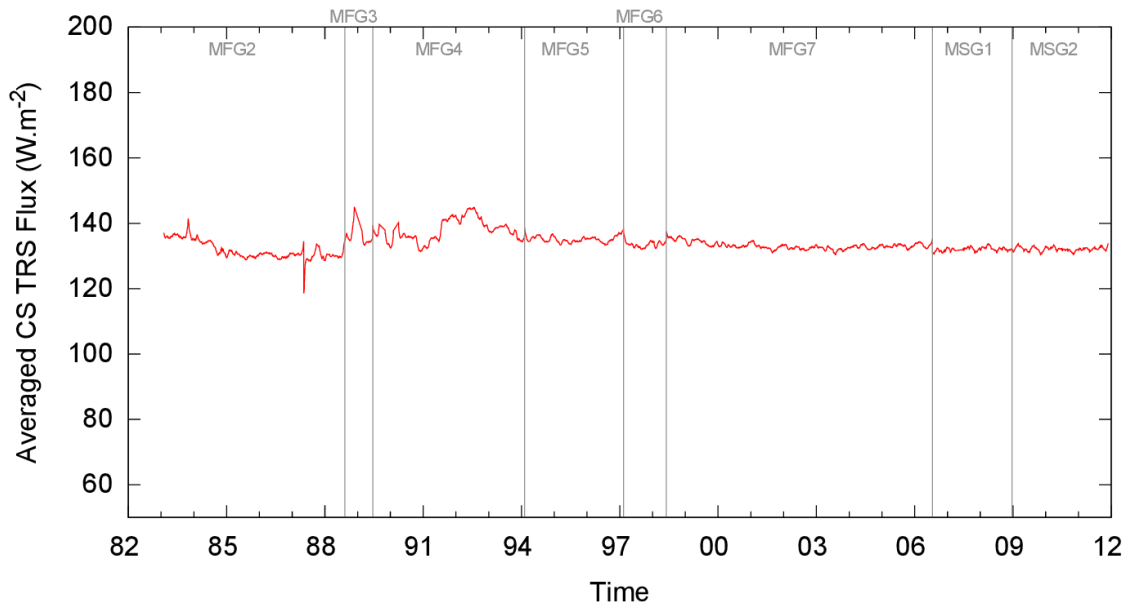
Figure 50: Time series of CS TRS fluxes averaged over the whole Meteosat disk.
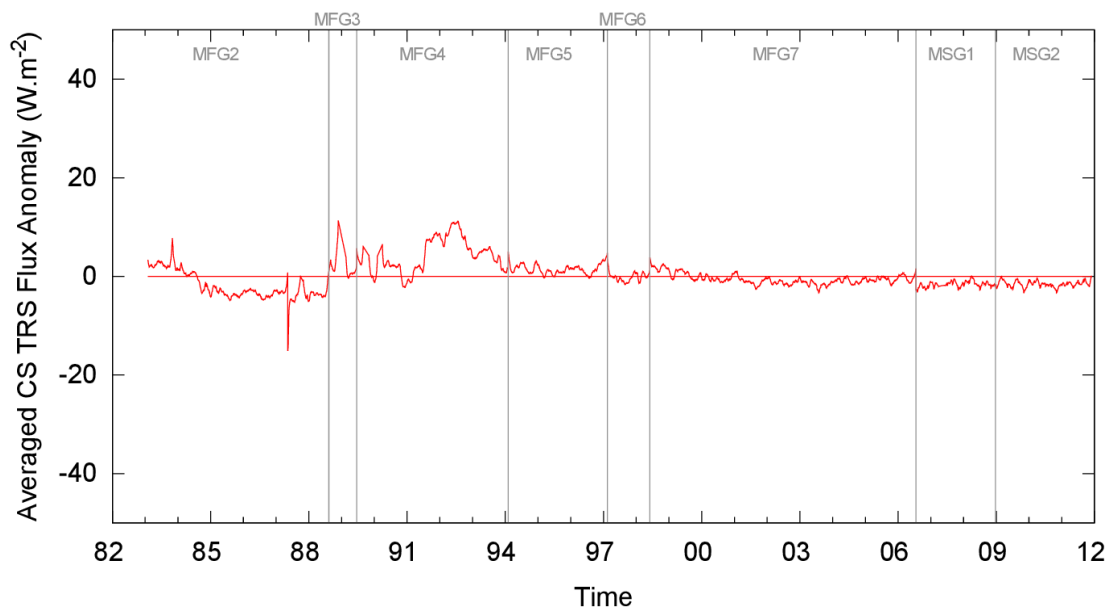
Figure 51: Time series of anomalies for the CS TRS fluxes averaged over the whole Meteosat disk. The anomalies are obtained by subtracting the average TRS flux (straight line) from the time series.

The TOA fluxes processing algorithm (see section 7) has also been applied in all-sky mode to process the 12 UTC repeat cycle over the full data record. Figure 52 shows the time series of all-sky TRS fluxes for deep convective clouds, which have been selected by taking the 0.995 percentile over the whole Meteosat disk. A smoothing procedure has then been applied on the resulting all-sky TRS fluxes, which consists in taking the local mean from

inside a moving window of N days. Figure 52 corresponds to a smoothing period of 60 days while Figure 54 corresponds to 180 days. The natural variations are nearly completely removed from the latter time series. Figures 53 and 55 show the anomalies for these time series.
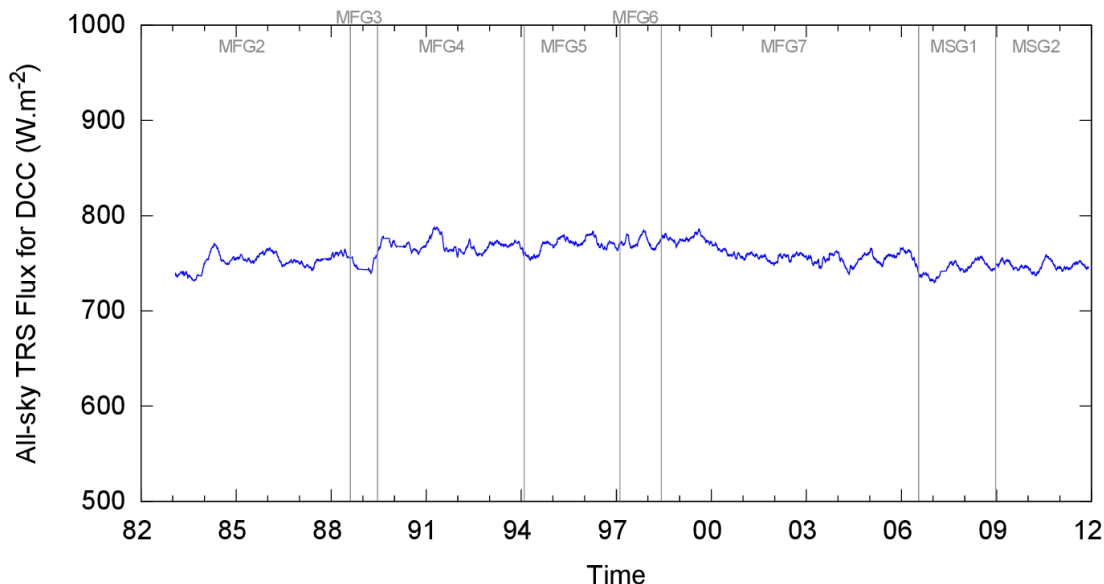
Figure 52: Time series of the all-sky TRS fluxes for deep convective clouds (corresponding to the 0.995 percentile over the whole Meteosat disk). Resulting fluxes have been smoothed over a period of 60 days.
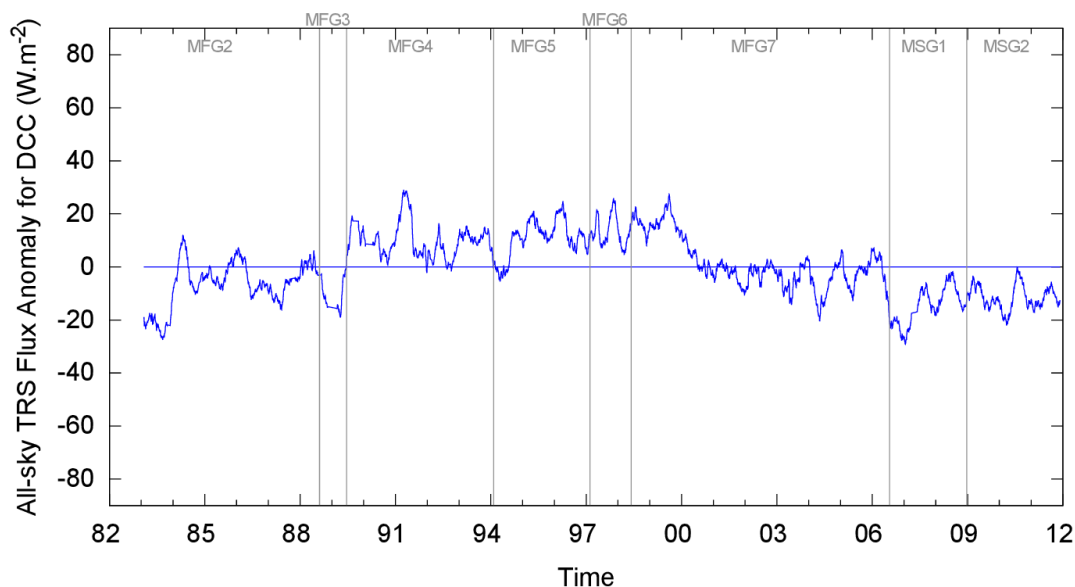
Figure 53: Time series of anomalies for the all-sky TRS fluxes for deep convective clouds (corresponding to the 0.995 percentile over the whole Meteosat disk) using a smoothing period of 60 days. The anomalies are obtained by subtracting the average TRS flux (straight line) from the time series.
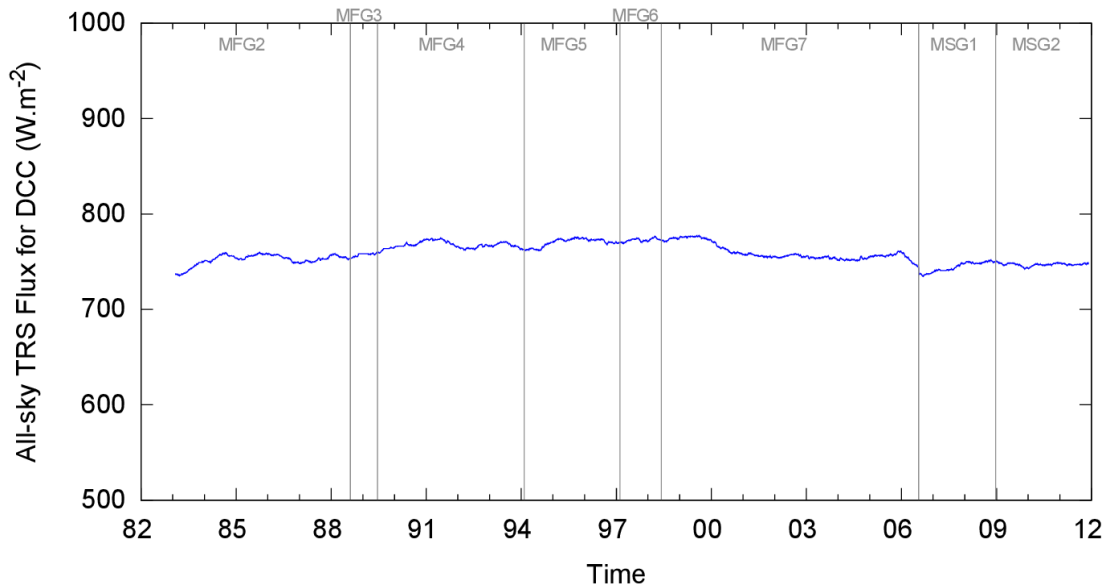
Figure 54: Time series of the all-sky TRS fluxes for deep convective clouds (corresponding to the 0.995 percentile over the whole Meteosat disk). Resulting fluxes have been smoothed over a period of 180 days.
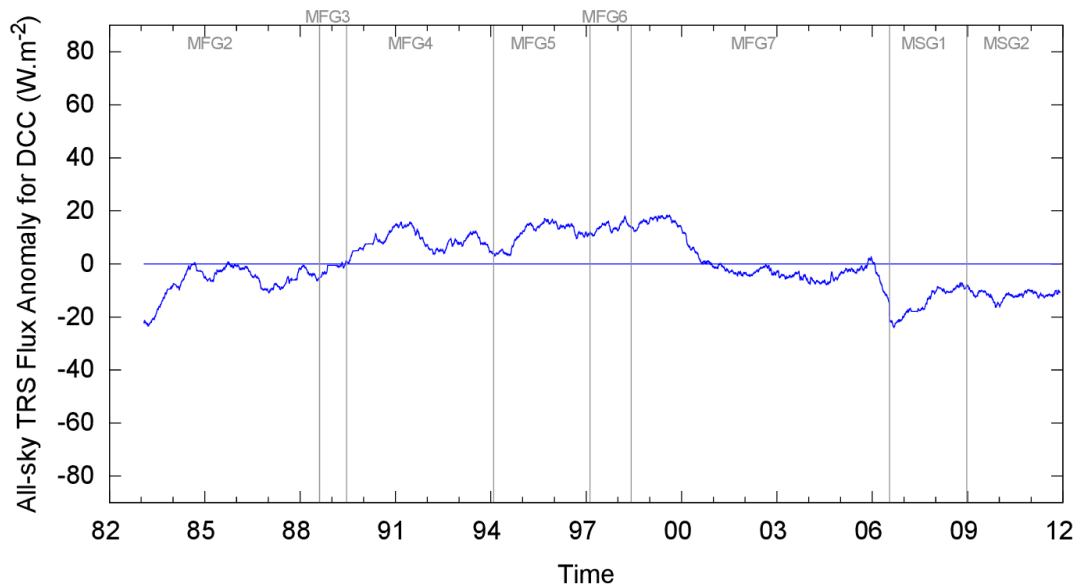
Figure 55: Time series of anomalies for the all-sky TRS fluxes for deep convective clouds (corresponding to the 0.995 percentile over the whole Meteosat disk) using a smoothing period of 180 days. The anomalies are obtained by subtracting the average TRS flux (straight line) from the time series.

The results presented here suggest that the decadal threshold accuracy requirement of 4 W/m^2/decade would be met for most of the scene types. This will be further analyzed once the data record is fully generated.

9.4 Discussion

In view of the comparison with CERES EBAF, it is expected that the MM products will fulfil the threshold accuracy requirements and is likely to also fulfil the target accuracy requirements. Validation activities will consolidate this result and also look at the daily mean and at the monthly mean diurnal cycle products. If the results obtained with the GERB data records (CM-113 and CM-115) [RD 2] can be extrapolated to the MVIRI data record, the daily mean and the monthly mean diurnal cycle should also fulfil their threshold requirement.

In terms of stability, the target requirement of 0.6 W/m^2/decade will most likely not be met, at least for the MFG era. The stability for MSG seems very good, as well for the TRS and the TET. The threshold requirement (4 W/m^2/decade) seems feasible as well for the MFG and MSG eras. The merging of MFG and MSG data seems not to introduce a discontinuity in the TET data record (similar bias of about -7.5 W/m^2 are observed for Met-7 and Met-8) as well as in the TRS data record (similar bias of about -0.5 W/m^2).

Obviously, improvements of the stability are expected by using the recalibration of the MVIRI WV and IR channels.

10 Output format description

The data format will be NetCDF. The file content is fully described in the PUM [RD 8].

11 References

Bentamy, A., Queffeulou, P., Quilfen, Y., & Katsaros, K. (1999). Ocean surface wind fields estimated from satellite active and passive microwave instruments. *Geoscience and Remote Sensing, IEEE Transactions on, 37*(5), 2469-2486.

Bertrand, C., Clerbaux, N., Ipe, A., & Gonzalez, L. (2003). Estimation of the 2002 Mount Etna eruption cloud radiative forcing from Meteosat-7 data. *Remote Sensing of Environment, 87*, 257-272.

Bertrand, C., Clerbaux, N., Ipe, A., Dewitte, S., & Gonzalez, L. (2005). Angular distribution models, anisotropic correction factors, and mixed clear-scene types: a sensitivity study. *Geoscience and Remote Sensing, IEEE Transactions on, 43*(1), 92-102.

Clerbaux, N., Dewitte, S., Gonzalez, L., Bertand, C., Nicula, B. & Ipe, A. (2003a). Outgoing Longwave Flux Estimation: Improvement of Angular Modelling Using Spectral Information. *Remote Sensing of Environment, 85*, 389-395.

Clerbaux, N., Ipe, A., Bertrand, C., Dewitte, S., Nicula, B. & Gonzalez, L. (2003b). Evidence of azimuthal anisotropy for the thermal infrared radiation leaving the Earth's atmosphere. *International Journal of Remote Sensing, 24*(14), 3005-3010.

Clerbaux, N., Dewitte, S., & Bertrand, C. (2006). RMIB GERB processing: Angular dependency models. *Reference Document MSG-RMIB-GE-TN-0008, RMIB.*

Clerbaux, N. (2007). Equivalence between the ARG, BARG and HR GERB formats. *Reference Document MSG-RMIB-GE-TN-0043, RMIB.*

Clerbaux, N., Dewitte, S., Bertrand, C., Caprion, D., De Paepe, B., Gonzalez, L., & Ipe, A. (2007). GERB-like data from Meteosat First Generation. In *Proceedings of the 2007 EUMETSAT Meteorological Satellite Conference (P48).*

Clerbaux, N. (2008). Processing of Geostationary Satellite Observations for Earth Radiation Budget Studies. PhD t*hesis at Vrije Universiteit Brussel Available via http://gerb.oma.be*

Clerbaux, N., Dewitte, S., Bertrand, C., Caprion, D., De Paepe, B., Gonzalez, L., Ipe, A., Russell, J.E., & Brindley, H. (2008a). Unfiltering of the Geostationary Earth Radiation Budget (GERB) Data. Part I: Shortwave Radiation. *Journal of Atmospheric and Oceanic Technology, 25*(7), 1087-1105.

Clerbaux, N., Dewitte, S., Bertrand, C., Caprion, D., De Paepe, B., Gonzalez, L., Ipe, A., & Russell, J.E. (2008b). Unfiltering of the Geostationary Earth Radiation Budget (GERB) Data. Part II: Longwave Radiation. *Journal of Atmospheric and Oceanic Technology, 25*(7), 1106-1117.

Clerbaux, N., Russell, J.E., Dewitte, S., Bertrand, C., Caprion, D., Depaepe, B., Gonzalez, L., Ipe, A., Bantges, R.J., & Brindley, H.E. (2009). Comparison of GERB Instantaneous Radiance and Flux Products with CERES Edition-2 Data. *Remote Sensing of Environment, 113*(1), 102-114.

Decoster, I., Clerbaux, N., Govaerts, Y. M., Baudrez, E., Ipe, A., Dewitte, S., Nevens, S., Velazquez Blazquez, A., & Cornelis, J. (2013a). Evidence of pre-launch characterization problem of Meteosat-7 visible spectral response. *Remote Sensing Letters, 4*(10), 1008-1017.

Decoster, I., Clerbaux, N., Baudrez, E., Dewitte, S., Ipe, A., Nevens, S., Velazquez Blazquez, A., & Cornelis, J. (2013b). A Spectral Aging Model for the Meteosat-7 Visible Band. *Journal of Atmospheric and Oceanic Technology, 30*(3), 496-509.

Decoster, I., Clerbaux, N., Baudrez, E., Dewitte, S., Ipe, A., Nevens, S., Velazquez Blazquez, A., & Cornelis, J. (2014a). Spectral Aging Model Applied to Meteosat First Generation Visible Band. *Remote Sensing, 6*(3), 2534-2571.

Decoster, I. (2014b). Spectral ageing model for the Meteosat First Generation visible band. *PhD thesis at Vrije Universiteit Brussel.*

Dee, D. P., Uppala, S. M., Simmons, A. J., Berrisford, P., Poli, P., Kobayashi, S., Andrae, U., Balmaseda, M. A., Balsamo, G., Bauer, P., Bechtold, P., Beljaars, A. C. M., van de Berg, L., Bidlot, J., Bormann, N., Delsol, C., Dragani, R., Fuentes, M., Geer, A. J., Haimberger, L., Healy, S. B., Hersbach, H., Hólm, E. V., Isaksen, L., Kållberg, P., Köhler, M., Matricardi, M., McNally, A. P., Monge-Sanz, B. M., Morcrette, J.-J., Park, B.-K., Peubey, C., de Rosnay, P., Tavolato, C., Thépaut, J.-N., & Vitart, F. (2011), The ERA-Interim reanalysis: configuration and performance of the data assimilation system. *Quarterly Journal of the Royal Meteorological Society, 137*, 553–597.Dewitte, S., & Clerbaux, N. (1999). First Experience with GERB Ground Segment processing Software: Validation with CERES PFM Data. *Advances in Space Research, 24*, 925-929.

Dewitte, S., Crommelynck, D., & Joukoff, A. (2004) Total solar irradiance observations from DIARAD/VIRGO. *Journal of Geophysical Research, 109 A2.*

Dewitte, S., Janssen, E., Mekaoui, S., Science results from the Sova-Picard Total Solar Irradiance instrument. In *Proceedings of AIP Conference, 1531, 688-691.* Available via http://dex.doi.org/10.163/1.4804863.

Dewitte, S., Gonzalez, L., Clerbaux, N., Ipe, A., & Bertrand, C. (2008). The Geostationary Earth Radiation Budget Edition 1 data processing algorithms. *Advances in Space Research, 41*, 1906-1913.

EUMETSAT (2011). EUMETSAT satellites history. *Eum/ops/doc/08/4698*, EUMETSAT.

EUMETSAT (2012). ATBD for EUMETSAT Pre-Operational GSICS Inter-Calibration of Meteosat-IASI. *EUM/MET/TEN/11/0268*, v1A, EUMETSAT.

Goudie, A., & Middleton, N. (2000). Saharan dust storms: nature and consequences. Earth-*Science Reviews, 56*(1-4), 179–204.

Govaerts, Y. M (1999). Correction of the Meteosat-5 and -6 radiometer solar channel spectral response with the Meteosat-7 sensor spectral characteristics. *International Journal of Remote Sensing, 20,* 3677-3682.

Govaerts, Y. M., Arriaga, A., & Schmetz, J. (2001). Operational vicarious calibration of the MSG/SEVIRI solar channels. *Advances in Space Research, 28*(1), 21–30.

Govaerts, Y. M., Clerici, M., & Clerbaux, N. (2004). Operational calibration of the Meteosat radiometer VIS band. *IEEE Transactions on Geoscience and remote sensing, 42*, 1900-1914.

Harries, J., Russell, J., Hanafin, J., Brindley, H., Futyan, J., Rufus, J., Kellock, S., Matthews, G., Wrigley, R., Last, A., Mueller, J., Mossavati, R., Ashmall, J., Sawyer, E., Parker, D., Caldwell, M., Allan, P., Smith, A., Bates, M., Coan, B., Stewart, B., Lepine, D., Cornwall, L., Corney, D., Ricketts, M., Drummond, D., Smart, D., Cutler, R., Dewitte, S., Clerbaux, N., Gonzalez, L., Ipe, A., Bertrand, C., Joukoff, A., Crommelynck, D., Nelms, N., Llewellyn-Jones, D., Butcher, G., Smith, G., Szewczyk, Z., Mlynczak, P., Slingo, A., Allan, R., & Ringer, M. (2005). The Geostationary Earth Radiation Budget projet. *Bulletin of the American Meteorological Society, 86*(7), 945- 960.

Hewison, T. J., & König, M. (2008). Inter-calibration of Meteosat imagers and IASI. In *Proceedings of EUMETSAT Satellite Conference, Darmstadt, Germany, September 2008.*

Ipe, A., Bertrand, C., Clerbaux, N., Dewitte, S., & Gonzalez, L. (2003). Pixel-scale composite top- of-the-atmosphere clear-sky reflectances for Meteosat-7 visible data. *Journal Geophysical Research, 108*, 4612.

Ipe, A., Bertrand, C., Clerbaux, N., Dewitte, S., & Gonzalez, L. (2004). Validation and homogenization of cloud optical depth and cloud fraction retrievals for GERB/SEVIRI scene identification using Meteosat-7 data. *Atmospheric Research, 72*(1), 17-37.

Ipe, A., Gonzalez, L., Bertrand, C., Baudrez, E., Clerbaux, N., Decoster, I., Dewitte, S., Nevens, S., & Velazquez Blazquez, A. (2010). Cloud detection using IR SEVIRI channels for GERB. *Remote Sens. Environ.*, submitted, 2010.

Ipe, A. (2011). Cloud properties retrieval for climate studies from geostationary orbit. *PhD thesis at Vrije Universiteit Brussel. Available via http://gerb.oma.be*

Janssen, E., Dewitte, S., Conscience, C., Chevalier A., Meftah, M., Irbah, A., & Crommelynck, D. (2013). Efficiency revision for the DIARAD radiometers. *Submitted to Metrologia.*

Kato, Seiji, &Norman G. Loeb (2003). Twilight irradiance reflected by the earth estimated from Clouds and the Earth's Radiant Energy System (CERES) measurements. *Journal of climate 16*(15), 2646-2650.

Key, J.R., & Schweiger, A.J. (1998). Tools for atmospheric radiative transfer : Streamer and FluxNet. *Computers & Geosciences 24*(5), 443-451.

Loeb, N. G., Manalo-Smith, N., Kato, S., Miller, W. F., Gupta, S. K., Minnis, P., & Wielicki, B. A. (2003). Angular distribution models for top-of-atmosphere radiative flux estimation from the Clouds and the Earth's Radiant Energy System instrument on the Tropical Rainfall Measuring Mission satellite. Part I: Methodology. Journal of applied meteorology, 42(2), 240-265.

Loeb, N. G., Manalo-Smith, N., Kato, S., Miller, W. F., Gupta, S. K., Minnis, P., & Wielicki, B. A. (2003b). Angular distribution models for top-of-atmosphere radiative flux estimation from the Clouds and the Earth's Radiant Energy System instrument on the Tropical Rainfall

Measuring Mission satellite. Part II: Validation. Journal of applied meteorology, 42(2), 1748-1769.

Loveland, T. R., Reed, B.C., Brown, J.F., Ohlen, D.O., Zhu, Z., Yang, L.W.M.J., & Merchant, J.W. (2000). Development of a global land cover characteristics database and IGBP DISCover from 1 km AVHRR data. *International Journal of Remote Sensing*, *21*(6-7), 1303-1330.

Meirink, J.F., Roebeling, R.A., & Stammes, P. (2013). Inter-calibration of polar imager solar channels using SEVIRI. *Atmospheric Measurement Techniques, 6*, 2495-2508.

Mekaoui, S., & Dewitte S. (2008). Total Solar Irradiance measurement and modelling during cycle 23. *Solar Physics, 247(1), 203-216.*

Maidment, R. I., Grimes, D., Allan, R. P., Tarnavsky, E., Stringer, M., Hewison, T., ... & Black, E. (2014). "The 30 year TAMSAT African rainfall climatology and time series (TARCAT) data set." Journal of Geophysical Research: Atmospheres 119.18 (2014).

Minnis, P., S. Sun-Mack, D. F. Young, P. W. Heck, D. P. Garber, Y. Chen, D. A. Spangenberg, R. F. Arduini, Q. Z. Trepte, W. L. Smith, Jr., J. K. Ayers, S. C. Gibson, W. F. Miller, V. Chakrapani, Y. Takano, K.-N. Liou, & Y. Xie (2011). CERES Edition-2 cloud property retrievals using TRMM VIRS and Terra and Aqua MODIS data, Part I: Algorithms. *IEEE Transactions on Geoscience and Remote Sensing, submitted.*

Otterman, J., Starr, D., Brakke, T., Davies, R., Jacobowitz, H., Mehta, A., Chéruy, F., & Prabhakara, C. (1997). Modeling zenith-angle dependence of outgoing longwave radiation: Implication for flux measurements. *Remote Sensing of Environment, 62*, 90–100.

Pili, P. (2000). Calibration of SEVIRI. *Proc. 2000 EUMETSAT Meteorological Satellite Data Users' Conf.*, Bologna, Italy, EUMETSAT EUM P29, 33–39.

Press, W.H., Teukolsky, S.A., Vetterling, W.T., & Flannery, B.P (1992). *Numerical recipes in C: the art of scientific computing. Second Edition.* Cambridge University Press, Cambridge. 65,76,93,101.

Ricchiazzi, P., Yang, S., Gautier, C., & Sowle, D. (1998). SBDART: A research and teaching software tool for plane-parallel radiative transfer in the Earth's atmosphere. *Bulletin of the American Meteorological Society, 79*(10), 2101-2114.

Rossow, W.B., & Schiffer, R.A. (1999). Advances in understanding clouds from ISCCP. *Bulletin of the American Meteorological Society, 80,* 2261-2287.

Russell, J. (2006). Quality Summary for GERB Edition 1 L2 ARG Product. *Reference document, Imperial College. Available via http://cedadocs.badc.rl.ac.uk/1226/1/QS_GERB_L2ARG_updated2006.pdf*

Schmetz, J., Pili, P., Tjemkes, S., Just, D., Kerkmann, J., Rota, S., & Ratier, A. (2002). An introduction to Meteosat second generation (MSG). Bulletin of the American Meteorological Society, 83(7), 977-992.

Simmons, A., Uppala, S., Dee, D., & Kobayashi, S. (2007). ERA-Interim: New ECMWF reanalysis products from 1989 onwards. *ECMWF newsletter, 110*(110), 25-35.

Suttles, J.T., Green, R.N., Minnis, P., Smith, G.L., Staylor, W.F., Wielicki, B.A., Walker, J., Young, D.F., Taylor, V.R., & Stowe, L.L. (1988). Angular radiation models for Earth-atmosphere system : Volume 1: Shortwave radiation. *Reference Publication 1184, NASA*, July 1988.

Taylor, K.E. (2001). Summarizing multiple aspects of model performance in a single diagram. *Journal Geophysical Research, 106,* 7183-7192.

Theodore, B., & Heinemann, T. (2008). Monitoring the calibration of METEOSAT first and second generation radiance data using HIRS measurements. In *Proceedings of EUMETSAT Satellite Conference, Darmstadt, Germany, September 2008.*

Townshend, J., Justice, C., Skole, D., Malingreau, J.P., Cihlar, J., Teillet, P., Sadowski, F., & Ruttenberg, S. (1994). The 1-km AVHRR global data set: needs of the International Geosphere Biosphere Program. International Journal for Remote Sensing , 15, 3319-3332.

Uppala, S. M., Kållberg, P. W., Simmons, A. J., Andrae, U., Bechtold, V. D. C., Fiorino, M., Gibson, J. K., Haseler, J., Hernandez, A., Kelly, G. A., Li, X., Onogi, K., Saarinen, S., Sokka, N., Allan, R. P., Andersson, E., Arpe, K., Balmaseda, M. A., Beljaars, A. C. M., Berg, L. V. D., Bidlot, J., Bormann, N., Caires, S., Chevallier, F., Dethof, A., Dragosavac, M., Fisher, M., Fuentes, M., Hagemann, S., Hólm, E., Hoskins, B. J., Isaksen, L., Janssen, P. A. E. M., Jenne, R., Mcnally, A. P., Mahfouf, J.-F., Morcrette, J.-J., Rayner, N. A., Saunders, R. W., Simon, P., Sterl, A., Trenberth, K. E., Untch, A., Vasiljevic, D., Viterbo, P., & Woollen, J. (2005), The ERA-40 re-analysis. *Quarterly Journal of the Royal Meteorological Society, 131*, 2961–3012.

Wielicki, B.A., Barkstrom, B.R., Harrison, E.F., Lee III, R.B., Smith, G.L., & Cooper, J.E. (1996). Clouds and the Earth's Radiant Energy System (CERES): An Earth Observing System Experiment. *Bulletin of the American Meteorological Society , 77*, 853-868.

Wild, M., Folini, D., Schär, C., Loeb, N., Dutton, E. G., & König-Langlo, G. (2013). The global energy balance from a surface perspective. *Climate dynamics, 40*(11-12), 3107-3134.

Zhang, X., Friedl, M., & Schaaf, C. (2006). Global vegetation phenology from moderate resolution imaging spectroradiometer (MODIS): Evaluation of global patterns and comparison with in situ measurements. *Journal of Geophysical Reaseach: Biogeosciences, 111*(G4017), 1–14.

12 Glossary

AD	Applicable Document
ADC	Atlantic Data Coverage
ADM	Angular Dependency Model
ARG	Averaged Rectified and Geolocated
ATBD	Algorithm Theoretical Basis Document
AVHRR	Advanced Very High Resolution Radiometer
BARG	Binned Averaged Rectified and Geolocated
BB	Broadband
BT	Brightness Temperature
CDOP	Continuous Development and Operations Phase
CERES	Clouds and the Earth's Radiant Energy System
CM SAF	Satellite Application Facility on Climate Monitoring
COD	Cloud Optical Depth
CS	Clear-sky
DAAC	Distributed Active Archive Center
DC	Digital Count
DCC	Deep Convective Cloud
DGCDD	Dataset Generation Capability Description Document
DIARAD	Differential Absolute Radiometer
DISORT	Discrete Ordinate Radiative Transfer
DM	Daily Mean
DRI	Delivery Readiness Inspection
DSM	De-Spin Mirror
DWD	Deutscher Wetterdienst (German MetService)
ECMWF	European Centre for Medium Range Forecast
ECV	Essential Climate Variable
EDC	EROS Data Center
ERB	Earth Radiation Budget
ESA	European Space Agency
EUMETSAT	European Organisation for the Exploitation

	of Meteorological Satellites
FCDR	Fundamental Climate Data Record
FI	Filter Integration
FMI	Finnish Meteorological Institute
FOV	Field Of View
FSI	Filtered Solar Irradiance
GCOS	Global Climate Observing System
GERB	Geostatinonary Earth Radiation Budget Instrument
GSICS	Global Space-based Inter-Calibration System
HIRS	High-resolution Infrared Radiation Sounder
HR	High Resolution
HRV	High Resolution Visible
c	Infrared Atmospheric Sounding Interferometer
IGBP	International Geosphere Biosphere Program
IODC	Indian Ocean Data Coverage
IOP	Initial Operations Phase
IR	Infrared
ISCCP	International Cloud Climatology Project
KNMI	Koninklijk Nederlands Meteorologisch Instituut
LUT	Look-Up-Table
LW	Longwave
MARF	Meteosat Archive and Retrieval Facility
MeghaTropique	Indo-French MeghaTropique mission
MeteoSwiss	Meteorological Service of Switzerland
MFG	Meteosat First Generation
MM	Monthly Mean
MMDC	Monthly Mean Diurnal Cycle
MODIS	Moderate Resolution Imaging Spectroradiometer
MOP	Meteosat Operationnal Program
MRC	Missing Repeat Cycles
MSG	Meteosat Second Generation
MTP	Meteosat Transition Program
MVIRI	Meteosat Visible and InfraRed Imager

NANRG	Non-Averaged Non-Rectified Geolocated
NB	Narrowband
NetCDF	Network Common Data Form
NMHS	National Meteorological and Hydrological Services
NRT	Near Real Time
OLR	Outgoing Longwave Radiation
PSF	Point Spread Function
PUM	Product User Manual
RAA	Relative Azimuth angle
RAPS	Rotating Azimuth Plane Scan
RD	Reference Document
RMIB	Royal Meteorological Institute of Belgium
RMS	Root Mean Square
RSS	Rapid Scan Service
RTM	Radiative Transfer Model
SAF	Satellite Application Facility
SARAH	Surface Solar Radiation DataSet - Heliosat
SAS	Sun Avoidance Seasons
SBDART	Santa Barbara DISORT Atmospheric Radiative Transfer model
ScaRaB	Scanner for Radiation Budget Instrument
SEVIRI	Spinning Enhanced Visible and Infrared Imager
SGA	Sun Glint Angle
SMHI	Swedish Meteorological and Hydrological Institute
SOHO	Solar and Heliospheric Observatory
SR	Spectral Response
SSCC	SEVIRI Solar Channels Calibration
ST	Surface Type
SW	Shortwave
SZA	Solar Zenith Angle
TCDR	Thematic Climate Data Records
TET	Top Of the Atmosphere Emitted Thermal
TIS	Top of the Atmosphere Incoming Solar
TISA	Time-Space Averaging

TOA	Top Of the Atmosphere
TRMM	Tropical Rainfall Measurement Mission
TRS	Top of the Atmosphere Reflected Solar
TSI	Total Solar Irradiance
UKMO	UK Met-Office
VIRGO	Variability of solar Irradiance and Gravity Oscillations
VIRS	Visible and InfraRed Scanner
VIS	Visible
VZA	Viewing Zenith Angle
WF	Water Fraction
WV	Water Vapour
XADC	Extended Atlantic Data Coverage